Optical Properties of Silicon-On-Insulator Waveguide Arrays and Cavities

Hobbs, Gareth

Award date:
2014

Awarding institution:
University of Bath

Optical Properties of Silicon-On-Insulator Waveguide Arrays and Cavities

submitted by

Gareth David Hobbs

for the degree of Doctor of Philosophy

of the

University of Bath

Department of Physics

July 2013

for Emily, for everything...
although I know you'll never read this
and for Aneirin,
I may make you read this

Contents

1 Introduction to Silicon-on-Insulator Waveguides and Cavities 8

1.1 Background 9

1.2 Light in a Waveguide 12

1.2.1 Modes 13

1.2.2 Effective Area 19

1.3 Dispersion 20

1.3.1 Material Dispersion 22

1.3.2 Waveguide Dispersion 23

1.4 Optical Loss 25

1.5 Waveguide Fabrication 27

1.6 Optical Cavities 28

1.6.1 The Fabry-Pérot Etalon 28

1.6.2 Quality Factor and Finesse 31

2 Linear Dispersion in Waveguide Arrays 35

2.1 Linear Propagation in Arrays of SOI Photonic Wires 35
2.1.1 Supermodes - The Weakly Guiding, Weakly Coupled Regime . . 36
2.1.2 Strong Guiding and Weak Coupling 42
2.1.3 Slot-modes - The Strong Guiding and Strongly Coupled Regime 42
2.2 Coupling Induced Dispersion 44
2.3 Group Index Measurements 48
2.3.1 Experimental Methods 49
2.3.2 Numerical Modelling 54
2.4 Results 54
2.5 Analysis 57
2.6 Sample Imaging 62
2.7 Conclusions 66

3 Linear Properties of 1D Photonic Crystal Microcavities in Silicon 67

3.1 Review of Optical Microcavities 68
3.2 1D Photonic Crystal Microcavities in Silicon 72
3.2.1 A Fabry-Pérot Description 73
3.2.2 Cavity Mode Volume 77
3.3 Linear Characterisation of 1D PhC Microcavities 78
3.3.1 Experimental Setup 78
3.3.2 Low Q-factor Cavities 81

3.3.3 High Q-factor Cavities 85

3.3.4 Thermal Stabilisation and Tuning 86

3.4 Conclusions 91

4 Nonlinear Properties of 1D PhC Microcavities 93

4.1 Introduction to Optical Bistability 94

4.1.1 Optically Induced Refractive Index Changes 96

4.2 Thermally Induced Bistability 100

4.3 Free Carrier Induced Bistability 118

4.4 Interplay of Thermal and Free Carrier Effects 124

4.5 Conclusions 131

5 Conclusions and Future Work 132

A Device Layout for the Waveguide Array Chip 137

References 139

Acknowledgments

There are a number of people I would to thank for help and guidance throughout my PhD.

All of the members of the CPPM and the Department of Physics in general, for making it an enjoyable and friendly place in which to work.

Everyone I have played football with or against over the last four years. I can only apologise and assure you I really was trying.

Carles, for help with modelling in Comsol.

Pete, for all of the interesting discussions and help with laser maintenance... but mostly for putting up with my ridiculous questions.

My collaborators from the Department of Engineering at the University of Glasgow, Michael Strain, Marc Sorel, Marco Gnan, Antonio Samarelli and Richard De La Rue, for supplying the samples used throughout this thesis. Additional thanks to Michael for allowing me to visit and take over his lab for an entire week, as well as providing me with haggis.

My co-workers here at Bath, Charles de Nobriga, Wei Ding, Owain Staines, Andrei Gorbach, Jonathan Knight and Dmitry Skryabin. Particular thanks must go to Charles, with whom I worked closely during my first year and learned a great deal from.

Finally, and most of all, my supervisor William, for his continued guidance and support without which none of this would have been possible.

Abstract

This thesis details work undertaken over the past three and a half years looking at the optical properties of silicon-on-insulator waveguide arrays and 1D photonic crystal microcavities. Chapter 1 contains relevant background information, while chapters 2, 3 and 4 contain results of experimental work. Chapter 5 summarises the results and conclusions of the preceding chapters and also suggests some directions for possible future research.

Chapter 1 starts by introducing some of the fundamental aspects of guided wave optics and how these relate to silicon-on-insulator waveguides. The modes of single, uncoupled silicon waveguides are described, along with a brief description of how such waveguides can be fabricated. Following this a short introduction to optical cavities and the relevant parameters that can be used to describe them is provided.

In Chapter 2 results are presented that experimentally confirm the presence of coupling-induced dispersion in an array consisting of two strongly-coupled silicon-on-insulator waveguides. This provides an additional mechanism to tailor dispersion and shows that it is possible to achieve anomalous dispersion at wavelengths where the dispersion of a single wire would be normal.

In Chapter 3 the focus switches to the linear properties of 1D photonic crystal microcavities in silicon. The optical transmission of a number of different devices are examined allowing the identification of suitable microcavities for use in nonlinear measurements. Microcavities with Q-factors in excess of $\sim$40,000 were selected for use in the work presented in Chapter 4, whilst the possibility of thermally tuning the microcavity resonances is also investigated. A cavity resonance shift of 0.0770 ± 0.0004 nm K^{-1} is measured experimentally.

Chapter 4 looks at the nonlinear transmission of those microcavities identified as suitable in Chapter 3. More specifically, the response of the microcavities to thermal and free carrier induced bistability is considered. Thermally induced bistability is observed at a threshold power of 240 µW for the particular cavity chosen, with a thermal time of 0.6 µs also measured. Free carrier induced bistability is then observed for pulses with nanosecond durations and milliwatt peak powers. Following that, the interplay of thermal and free carrier effects is observed using input pulses of a suitable duration.

Chapter 1

Introduction to Silicon-on-Insulator Waveguides and Cavities

The idea of confining light in a dielectric material has been well known for some time, with John Tyndall demonstrating in 1870 that light could be confined and guided along a thin stream of water. Soon after it was demonstrated that light may also be confined in silica glass strands or 'light pipes' [1]. Now, over one hundred years after Tyndall, low loss fibre optic cables that transmit information in the form of optical pulses over vast distances are at the heart of the telecommunications industry. Just as optical fibres have become an integral part of modern communications, many now strongly believe that electronic microchips could benefit significantly by incorporating nanoscale optical waveguides and devices, creating photonic integrated circuits. The work described in this thesis is therefore focused on understanding the optical properties of arrays of evanescently coupled silicon-on-insulator (SOI) photonic wires, referred to simply as wires or arrays from here on, and 1D photonic crystal (PhC) microcavities in silicon. In this chapter, after relevant background information, some of the basic concepts of guided wave optics are reviewed in the context of SOI waveguides, starting with optical confinement. Following on from this, an introduction to optical cavities is provided, describing some of the concepts associated with their operation and also key parameters describing their performance.

1.1 Background

In recent years silicon photonics [2], the branch of photonics concerned with the utilisation of silicon (Si) for optical devices, has received significant attention [3]. This is undoubtedly due to the myriad number of potential applications of Si optical devices in the near-to-mid infrared [4, 5, 6]. The transparency of Si in the spectral region beyond 1.2 µm makes it a suitable material for waveguides operating in the 1.3 µm and 1.55 µm telecommunications bands. At the same time, the large refractive index of Si ($n \sim 3.5$) in the near infrared (IR), combined with a low index cladding such as air ($n = 1$) or silica ($n \sim 1.44$), leads to strong optical confinement due to the high index contrast (HIC). This allows the cross-sections of Si waveguides to be dramatically reduced, typically to below 0.1 µm^2, in which case they are referred to as 'nanowires'. Such small waveguides led to the possibility of designing compact and densely integrated optical devices, as well as bent waveguides with radii of curvature of the order of a few micrometres [7].

The silicon-on-insulator (SOI) platform, consisting of waveguides patterned into a thin guiding layer of Si, separated from the bulk Si substrate by an insulating layer of, for example, silica or sapphire, is highly compatible with current fabrication methods [8]. Complementary-metal-oxide-semiconductor (CMOS) techniques for Si are well developed [9], allowing the production of structures on the scale of tens of nanometres at low cost, as well as the possibility for easy integration with existing electronic technologies. These features, combined with the fact that Si is already the dominant material in the microelectronics industry, makes the idea of creating Si-based optical devices particularly attractive. In fact, many believe that the answer to the demand for ever-increasing bandwidths, data speeds and reduced power requirements may be met by incorporating optical devices on-chip in the form of 'photonic integrated circuits' [10]. Here, both electronic and photonic devices would work in tandem, allowing the manipulation of both photons and electrons. Since the first nanoscale Si waveguides were demonstrated by Soref and Lorenzo [11] they have thus emerged as a potential platform for the realization of densely packed, chip-scale photonic devices capable of emitting, guiding, modulating and detecting light.

Low-loss waveguides are an essential component of any photonic integrated circuit, with considerable progress having been made in this area to date. Losses as low as 0.1 dB cm^{-1} have been recorded for so-called 'rib waveguides' [12], for which the Si guiding layer sits on top of a thin slab of Si. Up until recently however, the minimum

bend radius for these types of waveguide to ensure low losses was large, typically of the order of 200 µm - 600 µm due to their relatively weak lateral confinement [13]. An alternate geometry is that of the 'strip waveguide', consisting of a rectangular strip of Si with sub-micron dimensions, on top of an insulating layer of e.g. silica. It is this type of Si waveguide that forms the basis of the devices considered in this thesis. The strong confinement offered by these waveguides allows for greatly reduced bend radii, whilst current losses are as low as $\sim$1 dB cm^{-1} [14]. In addition to low-loss waveguides, numerous passive optical devices including couplers, splitters, bends and filters have all been demonstrated for Si photonics [15].

Devices capable of emitting light are also of vital importance for the successful commercialisation of Si photonics. Si is, however, an indirect semiconductor so that achieving light emission, a key component for on-chip light sources, has proved difficult [16]. During the last decade however a number of breakthroughs have been made, from the realisation of a fully integrated Si laser based on the Raman effect [17] to hybrid Si lasers incorporating various types of microcavity [18].

Key to any active devices will be the use of nonlinear optical effects for, e.g. wavelength conversion [19, 20] and amplification [21, 22] etc. in order to provide various functionalities such as optical switching and amplification on a single chip. Si has a nonlinear optical response that is two to three orders of magnitude larger than silica, which combined with the increased intensities due to small waveguide dimensions, leads to the observation of nonlinear effects at low powers and over short length scales. Other materials with larger optical nonlinearities, such as aluminium gallium arsenide (AlGaAs, which by contrast is a direct gap semiconductor), are also being considered as an alternative to Si. For the reasons outlined above however, Si currently remains the preferred choice for the fabrication of nano-waveguides [23]. Once again, significant progress has already been made in the area of nonlinear Si photonics [24], with self and cross-phase modulation (SPM and XPM), four-wave mixing (FWM), coherent anti-Raman Stokes scattering and supercontiuum generation all having been observed in Si photonic wires to date ([25] and references therein).

The majority of these effects however have been observed only in individual wires; with less work having been carried out that focuses on either the linear or nonlinear properties of arrays of wires like those considered in this thesis. These consist of closely spaced, evanescently coupled Si wires with rectangular cross-sections on top of a silica insulating layer. Arrays fabricated from other materials, such as AlGaAs, can also be found in the literature and have provided researchers the opportunity to investigate

the physics of discrete systems in nature [26]. In the linear propagation regime the effects of discrete diffraction have been observed, whilst researchers have also noted self-focussing of light during nonlinear propagation [27]. Of continued interest is the possibility of using arrays as a system in which to observe pulses of light that are localized temporally, known as solitons [28], and both temporally and spatially, known as spatial-discrete temporal quasi-solitons, or 'light-bullets' [29].

The two wire array, or directional coupler, considered in this thesis has a wall-to-wall separation of just 100 nm, much smaller than many of the arrays previously considered in the literature [26]. Due to the close proximity of adjacent wires there is strong coupling between them, so that the optical properties of arrays of this type can differ significantly from those of a single wire. More specifically, the dispersion experienced by light propagating in strongly-coupled waveguide arrays can be very different to that of a single, uncoupled wire. The magnitude and relative sign of the dispersion experienced by light in a Si waveguide can significantly impact the types of nonlinear effects observed, ranging from modulation instability and four-wave mixing to solitons [30]. The work carried out in the first part of this thesis is therefore focussed on understanding the linear, dispersive properties of the simplest possible SOI waveguide array, the two wire directional coupler.

The ability to modulate light on-chip is another important aspect of a successful integration of photonic and microelectronic devices, particularly for optical interconnects [31]. As with many of the other aspects of Si photonics, improvements in the performance of on-chip optical modulators have been dramatic in recent years, with bandwidths increasing from megahertz to the multi-gigahertz regime [32]. Modulators based on refractive index changes due to temperature changes [33] and the much faster plasma dispersion effect have been demonstrated. Typically in the case of modulators relying on the plasma dispersion effect, free-carriers are injected via the incorporation of a p-i-n junction on chip, either into a Mach-Zehnder interferometer [34] or a resonant structure such as a ring resonator [35].

So-called microresonators (or microcavities) [36], like their conventional counterparts, are capable of confining light for extended periods. However, the greatly reduced size of optical microcavities means that light intensities inside them can be extremely high for even modest input powers. The ability to strongly confine light in extremely small volumes, in some cases approaching the order of a cubic wavelength, has sparked considerable interest in this area of nanophotonics. A wide variety of microcavity geometries exist for Si (and will be reviewed in Chapter 3), with researchers aiming to fabricate

devices capable of confining light for longer and longer times and in ever decreasing volumes. This extreme light confinement makes it possible to study the effects of quantum electrodynamics (QED) [37], making optical microcavities of great interest from a fundamental point of view. At the same time, microcavities are becoming increasingly important components for on-chip devices including light sources [38], modulators [35] and switches [39, 40], due to the potential for fast modulations and low power requirements as a result of enhanced field strengths on resonance. Both switching and modulation usually require some method of modulating the refractive index of the micrcocavity, leading to a bistable output [41]. Knowledge of the nonlinear response of a given cavity is therefore necessary when determining its suitability as a modulator or switch. At this point, optical bistability and switching have been demonstrated for a number of different microcavity geometries and using a number of different effects (see e.g. the work of Lipson et al. on ring microcavities [42, 43]). The work in the second part of this thesis focuses on a specific type of microcavity known as a 1-dimensional (1D) photonic crystal microcavity [44] and aims to make a full characterisation of their nonlinear response, as well as assessing their potential for use as an optical modulator.

1.2 Light in a Waveguide

The physical mechanism used to confine light in photonic wires is the same as that in conventional step-index fibres, namely total internal reflection (TIR) [45]. In the ray picture of geometric optics the process can be understood by considering the angles of the incident and refracted waves at the interface between regions of differing refractive index. Here refractive index, n, is defined as the ratio of the speed of light in vacuum, c, to the phase velocity of light in the medium, v. When propagating from a region of high to low refractive index, for light incident at an angle exceeding a certain critical angle, θ_c, the refracted wave becomes imaginary and all of the power is carried by the reflected wave. At this point the wave is said to be totally internally reflected. Thus, in the simplest possible case, by having a core of refractive index n_{co} surrounded by a cladding of lower refractive index, n_{cl}, known as a step-index profile, it is possible to confine and guide light in the high index region, as shown in Fig. 1.1. Here only those waves incident at an angle greater than θ_c will experience TIR and be guided. One can then define the numerical aperture (NA) of a waveguide as [46],

$$NA = \sqrt{n_{co}^2 - n_{cl}^2} = n_{out} \sin(\theta_{max}) \tag{1.1}$$

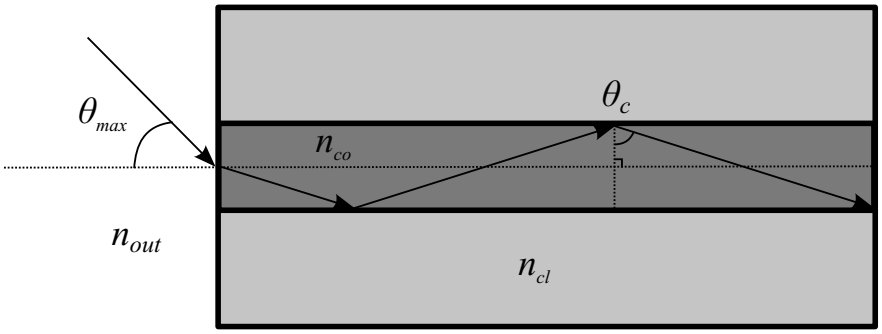

Figure 1.1: The ray picture of index-guiding with light confined to the high index core region, n_{co}, through TIR at the boundary with the low index cladding, n_{cl}. The maximum angle at which light can be coupled into the structure, θ_{max}, is also shown. As the dimensions of the high and low index regions approach that of the wavelength being confined this simple picture becomes inaccurate, at which point it is necessary to solve Maxwell's equations to correctly describe the confinement.

where θ_{max} is a measure of the maximum external angle at which light can be launched into the core of the waveguide and still be guided. Another parameter often used to characterize a step-index fibre is Δn [46], which is related simply to the difference in refractive indexes of the core and the cladding via

$$\Delta n = \frac{n_{co} - n_{cl}}{n_{co}}. \tag{1.2}$$

The value of Δn for a standard optical fibre is typically around 0.02, while for SOI photonic wires it is around 0.6 due to the large index contrast between the Si core and silica and air claddings.

1.2.1 Modes

The above approach gives a simple, intuitive understanding of how light can be confined within an optical waveguide. However, it becomes increasingly inaccurate as the dimensions of the guiding structure are reduced from those of a bulk material, so that it becomes necessary to consider the wave nature of light [45]. Thus, in order to gain further insight into the way in which light propagates in such a structure, in particular the distribution of the electric and magnetic fields ($\vec{E}$ and $\vec{H}$), it is necessary to solve Maxwell's equations. For a linear, isotropic, source free medium, Maxwell's equations can be written as

$$\nabla \cdot \vec{D} = 0 \tag{1.3}$$

$$\nabla \cdot \vec{H} = 0 \tag{1.4}$$

$$\nabla \times \vec{E} = -\frac{1}{\epsilon_0 c^2}\frac{\partial \vec{H}}{\partial t} \tag{1.5}$$

$$\nabla \times \vec{H} = \frac{\partial \vec{D}}{\partial t} \tag{1.6}$$

where ϵ_0 is the permittivity of free space, t is time and $\vec{D}$ is the electric displacement, related to $\vec{E}$ via the constituent relation

$$\vec{D} = \epsilon_0 \vec{E} + \vec{P} = \epsilon_0 \vec{E} + \epsilon_0 \chi^{(1)} \vec{E} = \epsilon_0 (1 + \chi^{(1)}) \vec{E}. \tag{1.7}$$

Here $\vec{E}$ induces a material polarization $\vec{P}$ (where $\vec{P} = \epsilon_0 \chi^{(1)} \vec{E}$ and $\chi^{(1)}$ is the first-order electronic susceptibility) that causes a separation of positive and negative charges within the material, leading to a dipole moment. An oscillating $\vec{E}$ will then lead to oscillating dipoles, $\vec{P}$, that re-radiate the field. The total field $\vec{D}$ is therefore the sum of the incident field $\vec{E}$ and the induced polarization $\vec{P}$. In the case of linear optics this polarization is assumed to be proportional to the first power of the electric field, whilst for sufficiently high intensities in the regime of nonlinear optics, $\vec{P}$ is expanded as a power series, leading to a variety of new, nonlinear effects [47].

Assuming a uniform waveguide that has continuous translational symmetry in the z direction, a trial solution to the above equations of the form

$$\vec{E}(x, y, z, t) = \vec{E}(x, y) e^{i(\beta z - \omega t)}, \tag{1.8}$$

can be used, where ω is angular frequency. Here the wave is assumed to be propagating in the z direction, so that $\vec{E}(x, y)$ is the transverse field distribution. Under these assumptions, the above Maxwell's equations can then be manipulated to give the vector wave equation [48],

$$\nabla_T^2 \vec{E} + (k^2 n^2 - \beta^2)\vec{E} = -(\nabla_T + i\beta \hat{\underline{z}})(\vec{E} \cdot \nabla_T \ln n^2) \ . \tag{1.9}$$

Here ∇_T is the transverse Laplacian, $\vec{E}(x,y)$ is the transverse field distribution, k is the wave vector ($\frac{2\pi}{\lambda}$ where λ is wavelength), $\hat{\underline{z}}$ is a unit vector in the propagation direction and β is the component of k parallel to the optical (z) axis, known as the propagation constant. Note that an analogous equation could be derived for $\vec{H}$ instead of $\vec{E}$. This equation can then be solved to find the appropriate values of β and $\vec{E}(x,y)$ for a given waveguide geometry, with the resulting solutions known as modes. These are electromagnetic waves that propagate without change to their transverse field distributions, except for a phase factor determined by β. One can also define an effective mode index,

$$n_{eff} = \frac{\beta}{k} \tag{1.10}$$

while it can be shown that for confinement it is required that $n_{cl} < \frac{\beta}{k} < n_{co}$. Modes that fulfil this condition are known as guided modes, which are propagating in the core region and decay exponentially in the cladding. Alternatively, modes with $\frac{\beta}{k} < n_{cl}$ form a continuum of states known as radiation modes that are not confined by the waveguide.

As the right-hand side of Eq. (1.9) contains terms that couple the x and y components of $\vec{E}$ (and similarly for $\vec{H}$) the resulting modes do not have simple polarisation states. Solutions are thus typically analytically intractable and require numerical methods for all but the simplest geometries. Perhaps the simplest waveguide geometry for which there is an analytic solution to Eq. (1.9) is the 2D symmetric planar, or slab, dielectric waveguide. This consists of a core layer of uniform refractive index, n_{co}, and thickness $2a$, between two layers of cladding material with refractive index n_{cl}, as shown in Fig. 1.2. In order for light to be confined in the core layer it is necessary that $n_{co} > n_{cl}$, whilst each layer is assumed to be unbounded.

As the $\nabla_T \ln n^2$ terms in the vector wave equation are only non-zero where n varies, for a step-like refractive index profile like that shown in Fig. 1.2, the terms are only non-zero at the boundaries between the core and cladding layers. In this case an analytic solution is therefore possible by solving the vector wave equation for the longitudinal (z) components of $\vec{E}$ (or $\vec{H}$) in the core and cladding separately, where the right-hand side of the vector wave equation can be set to zero, and then applying suitable boundary conditions to include the effects of the non-zero $\nabla_T \ln n^2$ terms at the boundary. The relevant boundary conditions in this case are that $\vec{H}$ and the longitudinal components of $\vec{E}$ be continuous across the boundary and that all of the fields remain finite everywhere.

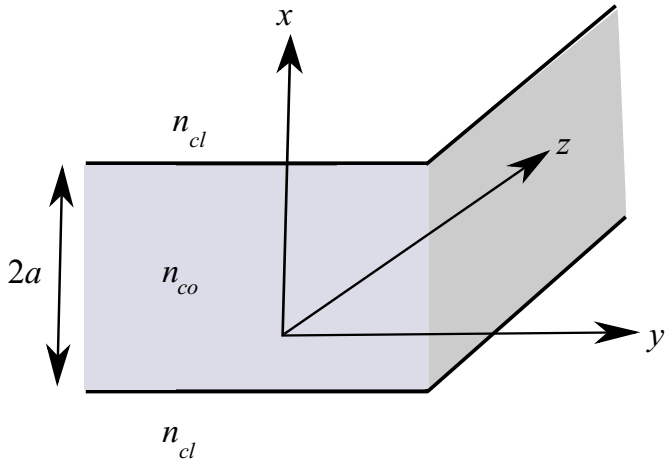

Figure 1.2: Geometry of a symmetric, planar slab waveguide, which is assumed to be unbounded in the y and z directions. The core region has a width of $2a$ and a refractive index of n_{co} whilst the cladding layers have refractive index n_{cl}.

As there are numerous suitably sized textbooks describing the above analysis the main results are simply summarised here, with the the interested reader directed to e.g. [48] for further details. The resulting solutions for the slab waveguide of Fig. 1.2 are found to oscillate sinusoidally within the core region and decay exponentially in the cladding and can be divided into two families, the transverse electric (TE) modes for which $E_z = E_x = 0$ everywhere, and the transverse magnetic (TM) modes for which $H_z = E_y = 0$ everywhere. The modes are also found to possess odd or even symmetry with respect to the centre of the core layer in the x direction. The most strongly confined modes from each family are known as the fundamental TE and TM modes respectively and they possess the highest β, whilst for the planar geometry considered here they will always be guided. Additional solutions, known as higher-order modes, that possess lower β's, undergo a greater number of oscillations in the core region and are more weakly confined can also be found, with the number depending both on the thickness of the guiding layer and the core-cladding index difference.

At this point a useful analogy can be made between the modes of a waveguide and the quantum states of an electron in a 2D finite potential well. In each case the confinement leads to a quantization of the available states of the system, in terms of β for a waveguide or energy for an electron. A higher n_{co} for light in a waveguide is therefore equivalent to a deeper potential well for an electron and therefore stronger confinement. Solutions for the confined states in both systems are oscillatory, but decay exponentially in the region outside the waveguide core or potential well. Just as in quantum mechanics, where an overlap of exponentially decaying electron wave

functions between two closely spaced potential wells is possible, the same can occur for closely spaced waveguides. This point becomes highly relevant below in Chapter 2, where arrays of waveguides are discussed.

Unfortunately, given the more complex geometry of the Si wires considered in this thesis, it is not possible to solve the vector wave equation analytically. It is therefore necessary to use numerical methods in order to accurately describe the modes of an SOI wire, which can be done straightforwardly using commercially available eigenvalue solvers. *COMSOL Multiphysics* ®, which utilises the finite element method, is used throughout this thesis. A schematic of the modelled geometry is shown in Fig. 1.3, whilst an example mode profile for an individual wire is shown in Fig. 1.4. Information on the fabrication of the arrays is given at the end of the chapter and more details on the modelling process can be found in Chapter 2.

Looking at the mode profiles in Fig. 1.4 there is a large component of $\vec{E}$, in this case E_z (Fig. 1.4 (c)), pointing in the direction of propagation as a result of the reduced waveguide dimensions. In addition, the mode shown in Fig. 1.4 is, in theory, the TE mode, with $\vec{E}$ ideally aligned entirely in the x-direction, parallel to the silica substrate. The fact that this is not the case, and that there is a non-zero component of $\vec{E}$ in the y-direction (Fig. 1.4 (c)), shows that the modes no longer possess a uniform polarisation, in contrast to the modes of the slab waveguide describe previously. However, the magnitude of E_y is much smaller than E_x, so that the mode can be considered a quasi-TE mode, with the principal electric field component aligned parallel to the substrate. A quasi-TM mode also exists for which the principal electric field component is perpendicular to the silica substrate. Throughout the remainder of this thesis the 'quasi-' will be omitted from the description of the modes, however it should be remembered that the TE and TM modes are not truly linearly polarised.

When looking at Fig. 1.4 one can also see that not all of $\vec{E}$ is confined to the high index Si core and that some extends into the surrounding silica and air claddings. In the case of E_x there is also a step-discontinuity at the the Si-air interface of the sidewalls of the waveguide, with the field much larger immediately inside the low-index air region. These points are particularly relevant when discussing arrays of coupled waveguides and so will be discussed in more detail in Chapter 2.

As mentioned above it is possible for a waveguide to support multiple confined modes, with waveguides that do so known as multimode waveguides. Simple expressions that provide an estimate of the number of modes supported by a conventional step-index fibre are well known [46], whilst expressions have also been developed in an attempt

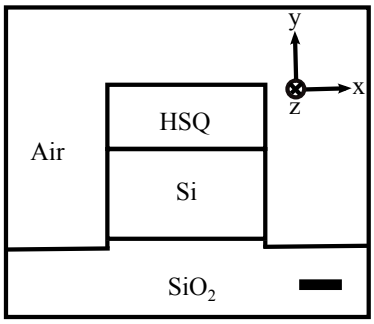

Figure 1.3: Schematic diagram of the cross-section of a Si wire. The Si wire sits on the silica (SiO_2) substrate, with a residual layer of etch mask material (HSQ) on top that is assumed to have the same refractive index as silica. The waveguide is otherwise surrounded by air. The scale bar is 100 nm in this case.

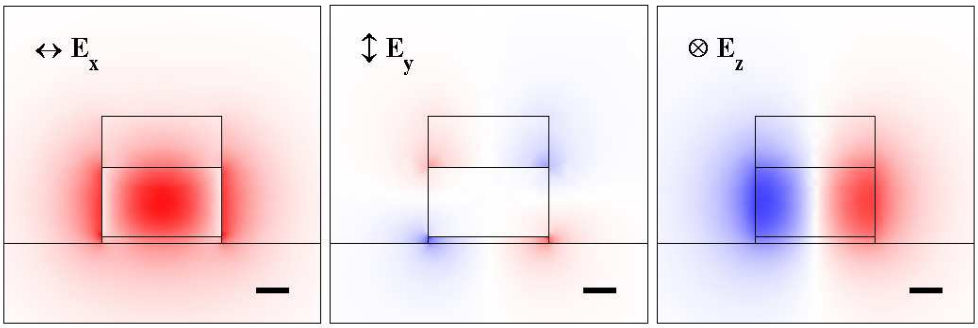

Figure 1.4: Electric field components of the fundamental mode of a wire with a 220 nm × 380 nm cross-section, shown over a 1 × 1 µm area. a) The x component of the electric field, parallel to the silica substrate, showing discontinuities at the side-walls. b) The non-zero y component of the electric field, perpendicular to the silica substrate, indicating the modes are no longer truly linearly polarised. c) The z component of the electric field, coming out of the page and pointing in the direction of propagation, demonstrating the modes are no longer transverse. Colour saturation gives absolute magnitude with red and blue indicating positive and negative phase respectively. The scale bar is 100 nm in each case.

to provide some insight into guidance in SOI wires. In particular, Aalto [49] identifies an approximate expression for the single-mode condition of an SOI strip waveguide operating at around 1550 nm as,

$$W \times H < 0.13\,\mu\text{m}^2, \tag{1.11}$$

where W and H are the waveguide width and height respectively and core and cladding indexes of 3.476 and 1.444 have been assumed in the calculations. Due to the extremely small cross-sectional areas of the waveguides considered in this work (220 nm $\times$ 380 nm for the individual wires that comprise the arrays in Chapter 2 and 220 nm $\times$ 500 nm for the microcavities in Chapter 3), they can only support the fundamental mode, and are therefore single-mode waveguides.

1.2.2 Effective Area

When characterising modes it is almost always necessary to have some estimate of the transverse mode area, especially when attempting to determine the intensity of light in a particular waveguide. For a given input power a smaller mode area will result in a higher intensity, which, depending on the application, may be an advantage or disadvantage. A high intensity is often desirable for applications involving nonlinear optics, whilst large mode area fibres have been developed to allow the delivery of high power laser pulses without any detrimental nonlinear effects [50]. If the intensity of light were uniform across the waveguide core and zero outside it, then this area would simply equal the cross-sectional area of the core. Of course this is not the case, as the mode amplitude varies across the core and also extends into the cladding. For this reason it is necessary to introduce an effective mode area [51], defined as

$$A_{eff} = \frac{|\int\int |\vec{E}(x,y)|^2 dxdy|^2}{\int\int |\vec{E}(x,y)|^4 dxdy}. \tag{1.12}$$

This definition of effective area depends on the geometric cross-section of the waveguide, but will also be influenced by the core-cladding index difference. It has proven extremely useful when considering conventional step-index fibres and even more complex geometries [52], such as those found in photonic crystal fibres, where the cladding

consists of a periodic arrangement of high and low index regions surrounding a uniform core [53]. Once again however, due to the subwavelength nature of SOI wires and their large Δn, the above expression becomes increasingly inaccurate. As a result a new, generalised expression has been developed [54] that takes into account the non-zero component of $\vec{E}$ in the direction of propagation and more accurately describes the effective area of subwavelength waveguides:

$$A_{eff} = \left(\frac{\mu_0}{\epsilon_0 n_{co}}\right)^2 \frac{[\int\int Re\{\vec{E} \times \vec{H}^*\} dxdy)]^2}{[\int\int \frac{2}{3}|\vec{E}|^4 + \frac{1}{2}|\vec{E}^2|^2 dxdy]}. \tag{1.13}$$

Using Equation (1.13), the A_{eff} of the fundamental mode of the 220 nm $\times$ 380 nm wire shown in Fig. 1.4 is just 0.11 µm^2. With such a small A_{eff}, extremely high optical intensities can be achieved in photonic wires, even for modest input powers.

1.3 Dispersion

Dispersion arises due to the frequency dependence of β and hence mode effective index, n_{eff}. The phase velocity of a wave is given by, $v_p = \frac{\omega}{k}$, while for a waveguide k is replaced with β so that $v_p = \frac{\omega}{\beta} = \frac{\omega}{k n_{eff}}$, so that waves of a different frequency will travel at different speeds due to the frequency dependence of n_{eff}. An optical pulse however will not travel at v_p, but will instead propagate at the group velocity, $v_g = \frac{d\omega}{d\beta}$, so that for a waveguide with group velocity dispersion (GVD), in which v_g varies with frequency, pulses will broaden in time as the slower frequencies lag behind the faster ones. Mathematically, the effects of dispersion are taken into account by taking a Taylor expansion in β around the central frequency of the pulse, ω_0, so that,

$$\beta = \frac{n_{eff}(\omega)}{c} = \beta_0 + \beta_1(\omega - \omega_0) + \frac{1}{2}\beta_2(\omega - \omega_0)^2 + \frac{1}{6}\beta_3(\omega - \omega_0)^3 + ... \tag{1.14}$$

where the coefficients β_i are given by

$$\beta_i = \left.\frac{d^i \beta}{d\omega^i}\right|_{\omega=\omega_0}, \qquad i = 0, 1, 2, 3, \ldots . \tag{1.15}$$

From Equation (1.14) and the definition of v_g given above it is then possible to identify that,

$$\beta_1 = \frac{1}{v_g} = \frac{n_g}{c} = \frac{1}{c}\left(n + \omega\frac{dn}{d\omega}\right) \tag{1.16}$$

$$\beta_2 = \frac{1}{c}\left(2\frac{dn}{d\omega} + \omega\frac{d^2n}{d\omega^2}\right) \tag{1.17}$$

where we have defined the group index as $n_g = \frac{c}{v_g}$. The coefficient β_2 describes how v_g varies with frequency and therefore the magnitude of the GVD and the amount by which a pulse spreads in time during propagation. This allows one to define a dispersion length, L_D, as

$$L_D = \frac{T_0^2}{\beta_2}, \tag{1.18}$$

which gives an estimate of the propagation distance over which the length of an optical pulse will have changed by a factor of $\sqrt{2}$ due to dispersion. Here T_0 is the duration of the input pulse, such that dispersive effects are more significant for shorter pulses as they must contain a larger range of frequencies and are also more sensitive to small group delays.

Although β_2 characterizes GVD, it is also common to use the dispersion parameter, D, particularly in the field of engineering when dealing with long lengths of optical fibre. D has units of ps nm^{-1} km^{-1} and gives the broadening of a pulse in picoseconds per nanometre of bandwidth per kilometer of propagation distance. D and β_2 are related through

$$D = -\frac{2\pi c}{\lambda^2}\beta_2 \ . \tag{1.19}$$

As the group index measurements presented in Chapter 2 are given as a function of wavelength it is convenient to express both n_g and D as functions of wavelength, as opposed to frequency. Re-writing equations (1.16) and (1.19) in terms of wavelength it is found that,

$$n_g = n(\lambda) - \lambda \frac{dn(\lambda)}{d\lambda} \tag{1.20}$$

and

$$D = -\frac{\lambda}{c}\frac{d^2 n}{d\lambda^2} = \frac{1}{c}\frac{dn_g}{d\lambda}. \tag{1.21}$$

When using D to describe GVD, a negative value corresponds to normal dispersion, in which longer wavelengths travel faster, while a positive value corresponds to anomalous dispersion, in which shorter wavelengths travel faster. The point at which D is zero is known as the zero GVD wavelength, at which point the higher order terms in Equation (1.14) become significant. The two main contributions to the frequency dependence of n_{eff}, material and waveguide dispersion, are discussed below.

1.3.1 Material Dispersion

Material dispersion occurs due to the frequency dependence of the refractive index of the bulk medium out of which the waveguide is fabricated. As shown previously in Equation (1.7), the field $\vec{D}$ propagating in any medium is the sum of the incident field, $\vec{E}$, and polarization, $\vec{P}$, due to the response of the material. In a classical approach, the bound electrons in the material can be modelled as damped harmonic oscillators and as such will have a characteristic resonant frequency. The response of the material will thus depend on the frequency of the applied $\vec{E}$, relative to the resonant frequency of the bound electrons. Assuming a low optical power, $\vec{P}$ has the same frequency as $\vec{E}$, but will be emitted with a different phase. The speed at which $\vec{D}$ propagates will then depend on the amplitudes and relatives phases of the two waves, leading to a frequency dependent refractive index. In reality a medium will have a number of resonances, corresponding to light at frequencies that exactly match the difference in energy between two different energy levels of the material.

Empirically, the frequency dependence of the refractive index can be taken into account through Sellmeier type equations [46], which are designed to fit measured refractive index curves and take the form

	Silicon	Silica
$\boldsymbol{\epsilon_\infty}$	11.6858	1
$\boldsymbol{\Delta\epsilon_1}$	0.00810461	0.6961663
$\boldsymbol{\Delta\epsilon_2}$	0.939816	0.4079426
$\boldsymbol{\Delta\epsilon_3}$	-	0.8974794
$\boldsymbol{\lambda_1}$ **(µm)**	1.1071	0.0684043
$\boldsymbol{\lambda_2}$ **(µm)**	1	0.1162414
$\boldsymbol{\lambda_3}$ **(µm)**	-	9.896161

Table 1.1: Sellmeier coefficients for silica and Si, taken from [55] and [56] respectively.

$$n(\lambda) = \sqrt{\epsilon_\infty + \sum_n \frac{\Delta\epsilon_n \lambda^2}{\lambda^2 - \lambda_n^2}}, \tag{1.22}$$

where ϵ_∞ is the electric permittivity at infinite frequency and the $\Delta\epsilon_i$ terms take into account resonances at wavelengths given by the corresponding λ_i. In silica, the $\Delta\epsilon_1$ and $\Delta\epsilon_2$ terms correspond to absorptions in the ultraviolet, whilst $\Delta\epsilon_3$ corresponds to an infra-red absorption. For Si, a modified Sellmeier Equation is often used [55], which provides a better fit to experimentally obtained refractive index data;

$$n_{Si}(\lambda) = \sqrt{\epsilon_\infty + \frac{\Delta\epsilon_1 \lambda_1^2}{\lambda_1^2 - \lambda^2} + \frac{\Delta\epsilon_2 \lambda_2^2}{\lambda^2}} \ . \tag{1.23}$$

In this case $\Delta\epsilon_1$ is the main cause of dispersion due to Si's 1.1 eV bandgap, whilst $\Delta\epsilon_2$ is a small correction highly detuned from any resonance. The various coefficients used in equations (1.22) and (1.23) are taken from [55] and [56] and are shown in Table 1.1. The values of n, n_g and D calculated from equations (1.23), (1.20) and (1.21) are shown in Fig. 1.5. From this it can be seen that the dispersion of bulk Si is strongly normal in the region around 1550 nm, the wavelength range of interest here.

1.3.2 Waveguide Dispersion

The other main contribution to the dispersion is that of waveguide dispersion, caused by the confinement of the light within a waveguide [48]. For multimode waveguides, different modes propagate with different group indexes, leading to dispersion. This

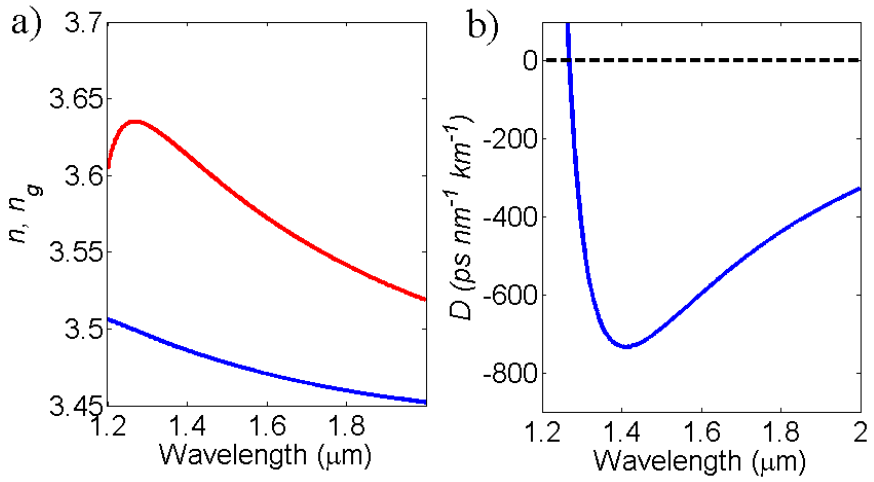

Figure 1.5: a) Variation of n (blue curve) and n_g (red curve) with wavelength for bulk Si, calculated from Equation (1.23). b) Variation of D with wavelength for bulk Si. The black dashed line indicates zero GVD, with negative values indicating normal dispersion and positive values corresponding to anomalous dispersion.

inter-modal dispersion is absent in the wires considered here as they are single-mode, however waveguide dispersion is still present as the confinement of the fundamental mode varies with wavelength. For conventional waveguides, with a small Δn and large core diameter, waveguide dispersion is usually a small correction to the material dispersion [48]. However, for photonic wires waveguide dispersion is actually the dominant form of dispersion, so that, despite the strongly normal dispersion of bulk Si in the near IR, it is possible to achieve a net anomalous GVD [57]. The waveguide dispersion is also highly sensitive to the dimensions of a waveguide, so that by simply tailoring the height and width of a wire it is possible to significantly alter its dispersive properties, as shown in Fig. 1.6. The zero GVD point at the short wavelength side can be shifted over a range of less than 0.1 µm around 1.2 µm, while by reducing the wire width a second zero GVD can be brought into the wavelength range of interest, whose position can be varied considerably. In Chapter 2, when looking at arrays of coupled wires, we introduce the idea of coupling-induced dispersion as another method of tailoring dispersion.

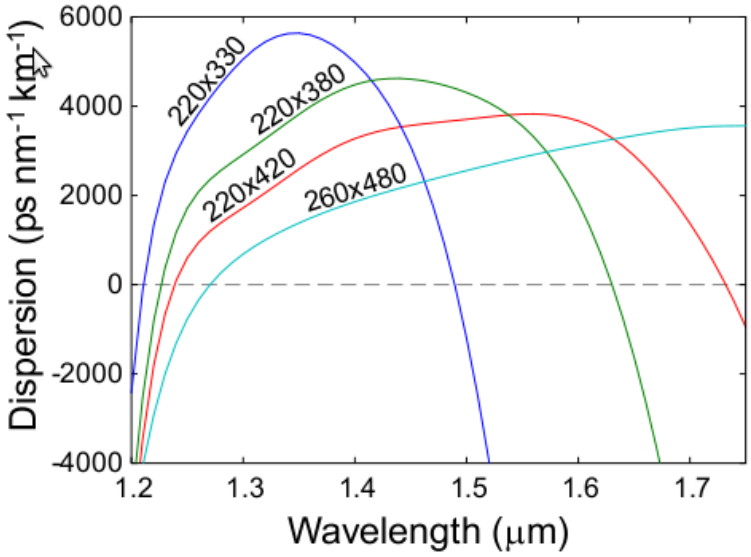

Figure 1.6: Effect of waveguide geometry on D for an SOI photonic wire [reproduced from [58]]. Array dimensions (width × height) are given in nm.

1.4 Optical Loss

Another important parameter when considering guided modes is the propagation loss, which is always present to a greater or lesser extent, and results in attenuation of the incident light as it propagates through the waveguide. The change in intensity with propagation can be straightforwardly described by,

$$-\frac{dI}{dz} = \alpha I_0 \tag{1.24}$$

where I_0 is the incident intensity and α is the linear loss term, often expressed in dBkm^{-1} for optical fibres and dBcm^{-1} for photonic wires.

The main sources of loss in the wires considered here are coupling of light to the silica substrate and also scattering out of the waveguides due to side-wall roughness [59]. This type of loss is particularly significant for wires, due to their small dimensions resulting in increased field intensities at the interfaces between the core and cladding (see (Fig. 1.4 (a)) due the large core-cladding index difference. The modes are therefore far more sensitive to any deviations in uniformity at the core-cladding boundaries. For this reason it is particularly important that wires are fabricated with low surface roughness to minimise loss. For state of the art silica fibres the loss can be as low as just 0.2 dBKm^{-1}, whilst for SOI wires loss values as low as ∼1 dBcm^{-1} have been

reported [14]. There may also be a small amount of linear material absorption in the spectral region around 1500 nm, despite the bandgap energy of Si corresponding to a wavelength of ∼1.1 µm, possibly at defect sites at the Si surface [60].

As well as these linear loss mechanisms, it is also possible for two photons to be absorbed simultaneously when their energies are sufficient to overcome the ∼ 1.1 eV band gap of Si, in a process known as two photon absorption (TPA) [61]. For silica optical fibres operating at 1550 nm this effect is negligible due to the large, ∼9 eV, bandgap of silica. This nonlinear absorption is intensity dependent and therefore becomes more significant at higher pulse powers and can lead to a saturation of the transmitted intensity. Mathematically the effects of TPA can be included in Equation (1.24) by adding an intensity dependent term,

$$-\frac{dI}{dz} = \alpha I_0 + \alpha_{TPA} I_0^2, \tag{1.25}$$

where α_{TPA} is the two photon absorption coefficient for Si, which is of the order of 1×10^{-11} mW^{-1} [62]. The absorption of the two photons leads to the generation of a pair of free charge carriers (FCC), as an electron is promoted from the valence band to the conduction band. The subsequent relaxation and recombination of the FCC over a certain time scale, known as the free-carrier lifetime, τ_c, leads to an increase in temperature of the Si. The exact value for τ_c will depend on the waveguide geometry [63] and is typically between 10 ns and 200 ns [64]. Prior to recombining, the FCC can also absorb photons (free carrier absorption, FCA), further increasing losses [65], as well as modifying the refractive index of Si [43].

The effects of TPA and the associated FCA are often highly detrimental and efforts are usually undertaken experimentally to minimise the effects of FCA, either through waveguide design or the careful choice of pulse duration and repetition rate. A reduction in τ_c from 3 ns to just 12.2 ps has also been achieved by incorporating a p-i-n junction into a waveguide [66], in order to sweep away any photogenerated carriers. It is also possible to eliminate TPA entirely by designing waveguides that operate at wavelengths beyond 2.2 µm, at which point TPA falls to zero [67]. However, as will be seen in Chapter 4, TPA and the modulation of the refractive index caused by FCC are not always undesired effects, and can be used to successfully modify the resonant properties of a Si microcavity.

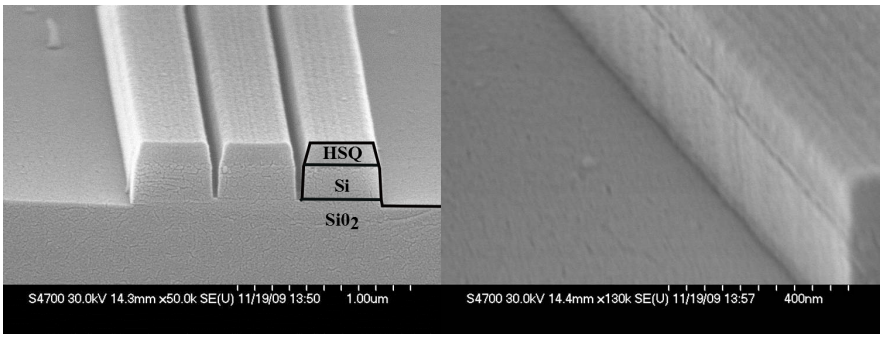

(a) (b)

Figure 1.7: a) SEM of a three wire array showing the good side-wall verticality of the wires. The overlay indicates the various parts of the waveguide and can be compared to the idealised geometry show in the schematic in Fig. 1.3. b) Close up of one of the sides of a wire showing the low surface roughness. Images were obtained by collaborators at the University of Glasgow.

1.5 Waveguide Fabrication

All of the devices (waveguide arrays and microcavities) used in the experiments described in the following chapters were fabricated by collaborators at the Department of Engineering at the University of Glasgow, according to the method described in [14]. The process starts with a macroscopic Si wafer, which contains a 1 µm thick layer of silica that isolates a 220 nm thick guiding layer from the rest of the Si wafer. A 160 nm thick layer of Hydrogen silsesquioxane (HSQ), a negative tone resist, is then deposited onto the wafer via spin coating and patterned using electron-beam lithography. After irradiation HSQ becomes an amorphous material similar to silica and, after discussion with collaborators, was assumed to have the same refractive index as silica. The waveguide pattern is then transferred to the Si guiding layer through inductively-coupled plasma reactive ion etching (ICP-RIE) [68] using a gas combination of SF_6/C_4F_8, which removes the exposed HSQ and underlying Si. The use of HSQ is advantageous as it provides high resolution in the lithography stage and shows good resistance to etching, removing the need for a second mask transfer stage to a harder etch mask material. The resultant waveguides, examples of which are shown in Fig. 1.7, have good side-wall verticality ($\sim 88^\circ$) and low side-wall roughness. This is highly significant as side-wall roughness has been identified as a key source of loss in nanoscale waveguides, due to the increased interaction of the guided mode with the side-walls, meaning these waveguides have low propagation losses of ~ 1 dBcm^{-1} [14]. Vertical side-walls are also important, as this limits the crosstalk between the TE and

TM modes of the waveguide. The Si channels that confine the light have rectangular cross-sections with heights of 220 nm and widths of either 380 nm or 500 nm, for the arrays (Chapter 2) and microcavities (chapters 3 and 4) respectively. They sit on top of a $\sim$ 20 nm thick silica pedestal due to the slight over-etch, necessary to ensure the Si guiding layer is fully etched through, are surrounded by air on two sides and have an approximately 160 nm thick layer of residual HSQ on top.

1.6 Optical Cavities

Finally, having given an introduction to SOI photonic wires and their fabrication in the preceding sections, the remainder of this chapter will be used to provide a brief overview of optical cavities and their characterisation. The physical concepts and parameters introduced here will be important for understanding the work presented below in chapters 3 and 4, where the linear and nonlinear properties of Si microcavities are studied.

1.6.1 The Fabry-Pérot Etalon

Conventional optical cavities, or resonators, allow the localisation of light in space, typically through the use of a suitable configuration of mirrors such that light in the cavity undergoes multiple reflections between them and is trapped. Perhaps the simplest possible example of such a cavity is the Fabry-Pérot etalon [69], which consists of two planar, partially reflecting mirrors separated by a certain distance. Whilst simple in configuration, a basic knowledge of the behaviour of a Fabry-Pérot etalon is sufficient to elucidate the key features of any optical cavity. Indeed, it will be seen in Chapter 3 that with some modifications, the theory outlined below can be applied equally well to the Si microcavities studied in this work.

In the case of a Fabry-Pérot etalon light incident on the cavity is transmitted through the first mirror and on entering is reflected back and forth, with a certain amount of light being transmitted through the second mirror after each round trip, as shown in Fig. 1.8. Assuming a monochromatic input the forward and backward propagating light can interfere either constructively or destructively, depending on the wavelength of the incident light, leading to the formation of a standing-wave. This interference leads to a strongly wavelength dependent transmission spectrum of the etalon, a characteristic of all optical cavities.

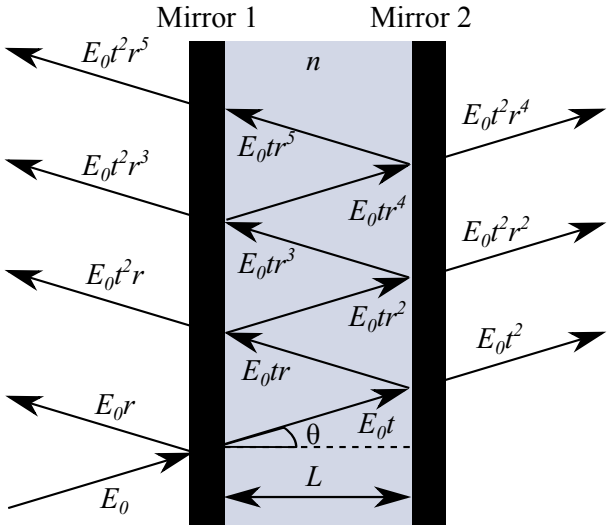

Figure 1.8: Schematic of a Fabry-Pérot etalon consisting of two planar mirrors, separated by a distance L and surrounding a medium of refractive index n. Light with electric field amplitude E_0 is incident on mirror 1 at an angle θ and undergoes multiple reflections, with the amplitudes of each reflected and transmitted wave related via the amplitude reflection, r, and transmission, t, coefficients of the mirrors, which are assumed to be the same for each.

With reference to Fig. 1.8 it is clear that the total transmitted intensity, I_T, is related to the sum of the contributions from each of the transmitted fields i.e.

$$I_T \propto |E_T|^2 = |E_0t^2 + E_0t^2r^2e^{i\phi} + E_0t^2r^4e^{2i\phi} + ...|^2, \tag{1.26}$$

where we have assumed that $r = |r|e^{i\phi_r}$, where ϕ_r is a phase shift due to a single reflection, $\phi = 2knL\cos\theta$ is the phase shift due to propagation (see Fig. 1.8 for symbols) and $r^2 + t^2 = R + T = 1$ i.e. there is no loss. Recognising that the above takes the form of a geometric progression (and $r < 1$), the ratio of incident to transmitted light for a Fabry-Pérot etalon can be written as [70],

$$\frac{I_T}{I_0} \propto \frac{1}{1 + \frac{R}{(1-R)^2}sin^2(\Phi/2)}, \tag{1.27}$$

where Φ is the cavity round trip phase shift due to propagation and reflection, given by

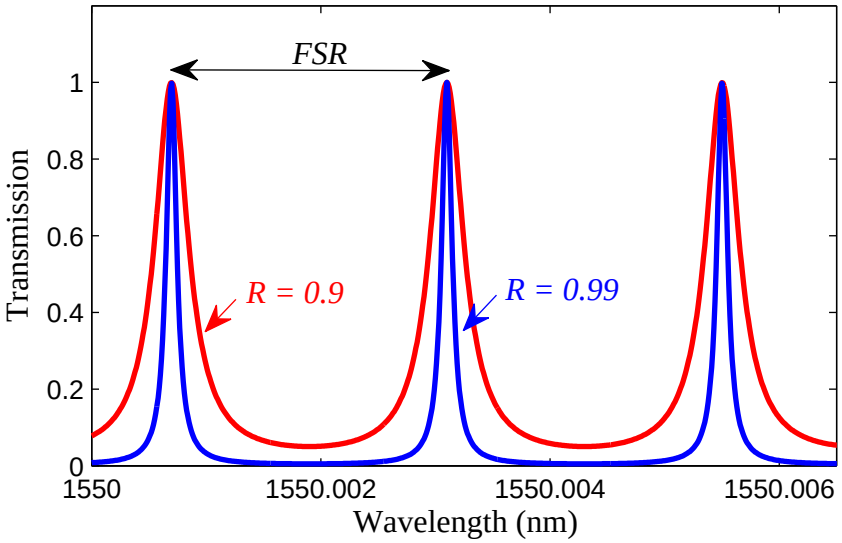

Figure 1.9: Transmission of a Fabry-Pérot etalon with $L = 1$ m and $n = 1$, calculated according to Equation (1.27) (ϕ_r is assumed to be negligible). The spacing between resonances, known as the free spectral range, FSR, is labelled and two values of mirror reflectivity, R, have been used.

$$\Phi = \phi + 2\phi_r. \tag{1.28}$$

In the case of bulk cavities ϕ_r is usually negligible, since $L >> \lambda$, whilst for the microcavities considered below this is not the case due to their small size. In addition, when considering microcavities embedded in photonic wires, the refractive index of the bulk material, n, is replaced by n_{eff}. Remembering that $k = \frac{2\pi}{\lambda}$, Equation (1.27) has been plotted as a function of wavelength in Fig. 1.9 for a cavity with $L = 1$ m and $n = 1$, assuming ϕ_r is constant with λ and $\theta = 0$.

Sharp, resonant peaks in transmission can be observed in Fig. 1.9 for wavelengths at which constructive interference occurs. Here the transmission can be unity if there are no sources of optical loss. For wavelengths away from these resonant peaks, destructive interference occurs and the transmission of the cavity is very low. The condition for maximum transmission occurs on resonance, when an integer number of half-wavelengths fit inside the cavity [70] i.e.

$$\lambda_{res} = \frac{2nL}{m}, \tag{1.29}$$

where m is an integer that specifies the order of the resonance. For a sufficiently long cavity there may be a large number of wavelengths that satisfy the resonance condition, e.g. for a laser with a central wavelength of 800 nm and a cavity length of 1 m there may be 10^5 or 10^6 resonances supported by the cavity within the laser bandwidth. Of course, in practical terms, for a cavity to support such a large number of resonances the mirrors used would need to be highly reflecting over the entire wavelength range.

Although in Fig. 1.9 transmission is plotted as a function of wavelength, the spacing between resonances, known as the free spectral range (FSR) of the cavity, is more naturally defined in terms of frequency. Using $c = \lambda\nu$, where ν is frequency and c is the vacuum speed of light, Equation (1.29) can be rewritten and the frequencies for resonance $m + 1$ and m can be subtracted so show that the FSR is given by

$$FSR = \frac{c}{2nL}. \tag{1.30}$$

The FSR is thus independent of mode order, m, and the spacing between resonances is constant when written in terms of frequency. This does of course assume that n remains constant over the entire spectral range, which would not be the case for a cavity fabricated from Si where n is a function of ω.

Also shown in Fig. 1.9 is the effect of varying R, with a higher R leading to a narrower resonance and lower transmission between resonances. As mentioned, in the ideal lossless case (with $R = 1$) the on resonance transmission would be unity, while the resonances themselves would be infinitely narrow. In a real situation however there is always some source of loss, leading to energy dissipation and a broadening of the resonances.

1.6.2 Quality Factor and Finesse

The level of broadening is described by the quality factor (or Q-factor) [71], Q, which is one of the most important figures of merit used to compare the performance of any optical cavities. In general the Q-factor is defined as 2π multiplied by the time-averaged energy stored in the cavity, divided by the energy-loss per optical cycle, or

$$Q = 2\pi \frac{Stored\ Energy}{Power\ Loss\ Per\ Cycle} = \omega_0 \frac{U}{P}, \tag{1.31}$$

where ω_0 is the resonant angular frequency, U is the electromagnetic energy stored in the cavity and P is the power radiated out. From this definition it is seen that the energy in the cavity decays exponentially, with a time constant $\tau = Q/\omega_0$. Alternatively, in the spectral domain the Q-factor is often defined as,

$$Q = \frac{\lambda_{res}}{\Delta\lambda} = \frac{\nu_{res}}{\Delta\nu}, \tag{1.32}$$

where ν_{res} is the resonant frequency, and $\Delta\lambda$ and $\Delta\nu$ are the full-width-half-maximum of the resonance in wavelength and frequency respectively. For large values of the quality factor the two definitions (equations 1.31 and 1.32) are equivalent, so that in the time domain the Q-factor gives an idea of how long photons of light will remain confined within the cavity, while in the spectral domain it indicates the width of the resonance. Thus, the higher the Q-factor, the longer photons remain within the cavity and the narrower the resonance. An example resonance showing λ_0 and $\Delta\lambda$ is shown in Fig. 1.10.

A high Q-factor is often desirable, as the increased temporal confinement leads to circulating powers inside the cavity that can far exceed the optical input power on resonance. A related property is the cavity finesse [72], $\mathcal{F}$, defined as the cavity FSR divided by $\Delta\nu$, so that

$$\mathcal{F} = \frac{FSR}{\nu_0} Q. \tag{1.33}$$

Using the definition of Q-factor in Equation (1.31), $\mathcal{F}$ can be shown to be equivalent to 2π multiplied by the time averaged energy stored in the cavity, divided by the energy-loss per cavity round trip (as opposed to per optical cycle for Q-factor). Both Q-factor and $\mathcal{F}$ are therefore figures of merit characterising the energy storage in a cavity. One important difference between the two parameters however, is that for a cavity in which losses due to the partial reflections at the mirrors dominate other sources of loss, such as absorption or scattering in the cavity medium, $\mathcal{F}$ is independent of L and represents the quality of the mirrors, whilst an increase in L would lead to an increase in Q-factor.

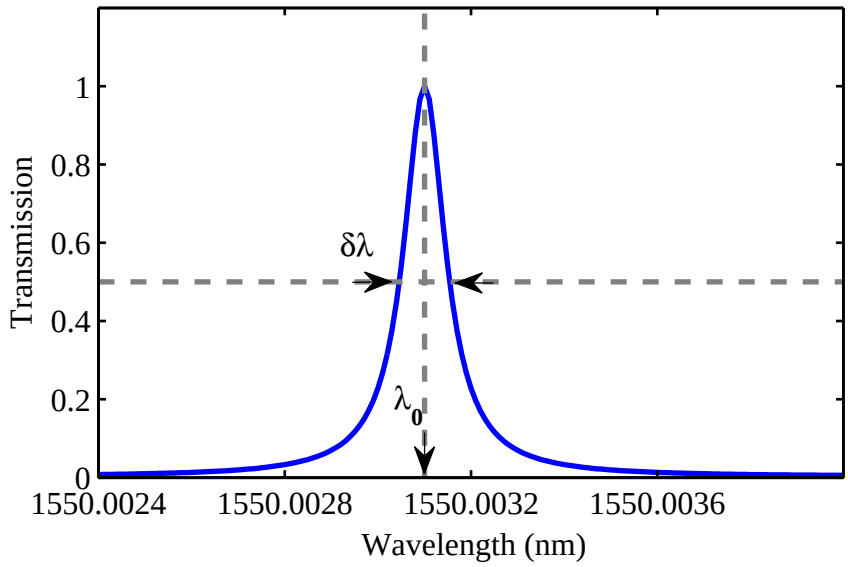

Figure 1.10: Example resonance showing the resonance wavelength, λ_0, and the full-width-half-maximum, $\Delta\lambda$, corresponding to a Q-factor of 7.8×10^6.

Following on from this, $\mathcal{F}$ for a Fabry-Pérot Etalon can be written as

$$\mathcal{F} = \frac{\pi\sqrt{R}}{1-R}, \tag{1.34}$$

again under the assumption that losses due to absorption, scattering etc. are negligible. Calculating the total intensity circulating inside a Fabry-Pérot Etalon, I_{cav}, by summing the forward and backward propagating waves in Fig. 1.8,

$$I_{cav} \propto |E_{cav}|^2 = |E_0 t + E_0 t r e^{i\phi/2} + E_0 t r^2 e^{i\phi} + E_0 t r^3 e^{3i\phi/2} + E_0 t r^4 e^{2i\phi} + ...|^2, \tag{1.35}$$

and using the definition of $\mathcal{F}$ from Equation (1.34) one finds that on resonance [73],

$$\frac{I_{cav}}{I_0} \simeq \frac{1}{1-R} = \frac{\mathcal{F}}{\pi\sqrt{R}}. \tag{1.36}$$

This means the circulating intensity inside a cavity on resonance can be significantly larger than the input, with the enhancement directly proportional to the cavity $\mathcal{F}$. It is for this reason high $\mathcal{F}$ cavities are desirable, as they provide the maximum possible enhancement to the input light allowing high intensities to be achieved for even moderate input powers.

It is clear then that the Q-factor characterises the spectral width of the resonances and the temporal decay rate of the stored energy, or photon lifetime, whilst $\mathcal{F}$ characterises the on resonance field enhancement provided by the cavity. Both Q-factor and $\mathcal{F}$ can be increased by reducing loss in the cavity, either by increasing the mirror reflectivity, as can be seen from Fig. 1.8 and Equation (1.34), or more generally by reducing cavity losses.

For conventional cavities, like those found in lasers, amplifiers and spectrometers, the mirror separations may be of the order of meters and the cavities themselves can be very large. Of course, for a smaller cavity volume, V, the region of space in which light is confined is reduced and the intensity of light in the cavity for a given input power necessarily increases. One can see this by considering that $I_{cav} \propto \mathcal{F} I_0$ from Equation 1.36, whilst noting that I_0 is simply the input power, P_{in}, divided by the area of the cavity cross-section. In addition, since $\mathcal{F} \propto Q$ whilst the Q-factor is in turn dependent on the cavity length one finds,

$$\frac{I_{cav}}{P_{in}} \propto \frac{Q}{V}. \tag{1.37}$$

Clearly then, to maximise the circulating intensity inside the cavity, I_{cav}, for a given P_{in}, it is necessary to design cavities with as large a Q/V ratio as possible. This is particularly useful for nonlinear applications, where high intensities are required in order to observe the desired nonlinear effects, and also for on chip devices with low power requirements. When evaluating the relative performance of different cavities it is therefore usual to compare the Q/V ratio for each. The improvements in nanofabrication that have permitted the fabrication of photonic wires like those discussed earlier have also led to the development of so-called optical microcavities [74]. These are devices with dimensions significantly smaller than their conventional counterparts, in some cases approaching a diffraction limited volume of $\left(\frac{\lambda}{2n}\right)^3$, ensuring extremely large values of Q/V. Various designs have been fabricated, with the ultimate aim of achieving large values of Q/V. In chapters 3 and 4 the linear and nonlinear properties of one specific type of microcavity, the 1D photonic crystal microcavity are investigated.

Chapter 2

Linear Dispersion in Waveguide Arrays

The effects of dispersion, as detailed in Chapter 1, often play a significant role in guided wave optics. In the case of optical telecommunications, high levels of uncompensated dispersion can lead to pulse broadening, causing temporal overlap of successive pulses and a loss of information. In nonlinear optics the relative sign and magnitude of dispersion can strongly impact the types of effects observed [51]. These can range from four-wave mixing and modulation instability to soliton formation, in which the effects of dispersion and nonlinearity balance to create pulses of light that propagate without change. The ability to control the dispersion of an optical system is therefore often highly desirable. In this chapter the possibility of tailoring the dispersion of the supermodes of an array of waveguides through coupling is investigated.

2.1 Linear Propagation in Arrays of SOI Photonic Wires

As noted in Chapter 1, the fields of a propagating mode are not confined solely to the core region, but decay exponentially into the cladding in the form of evanescent waves. If one waveguide is brought into close proximity with another, it is possible that there may be some overlap between the evanescent field of one waveguide with the core of another, leading to a coupling of light between the two. This transfer of light from one waveguide to another is analogous to the tunnelling of electrons between two finite

potential wells due to an overlap of their wavefunctions [75]. In the case of identical waveguides possessing the same β in isolation, the only case considered here, there will be complete power transfer from one guide to another and back again [76].

2.1.1 Supermodes - The Weakly Guiding, Weakly Coupled Regime

A set of such coupled waveguides may be viewed as a single, composite waveguide with modes of its own. It is possible to describe these modes by making the photonic tight-binding approximation [77]. This assumes that the presence of a nearby waveguide acts as a small perturbation to the first (weak coupling), so that modes of the composite system, known as supermodes, can be built up from a linear superposition of the modes of the individual waveguides (which are no longer modes of the coupled system). The approach takes its name from an analogous approximation in solid state physics, in which the wavefunction of a lattice is assumed to be a linear superposition of the electronic wavefunctions of the individual atoms [78].

For insight the modes of weakly coupled waveguides are described below, following the method used in [79]. For the case of two coupled waveguides, also known as a directional coupler, let $n_1(x, y)$ and $n_2(x, y)$ be the transverse index profiles of the individual waveguides (1 and 2) in isolation and $n(x, y)$ be the refractive index profile of the composite waveguide. The modes of the individual waveguides will then possess transverse mode profiles $\Psi_1(x, y)$ and $\Psi_2(x, y)$, with propagation constants β_1 and β_2, see Fig. 2.1 (a) and (b). Under the weak guidance approximation these will satisfy the scalar wave equations for the isolated wires, such that,

$$\nabla_T^2 \Psi_1(x, y) + [k_0 n_1(x, y)^2 - \beta_1^2] = 0 \tag{2.1}$$

and

$$\nabla_T^2 \Psi_2(x, y) + [k_0 n_2(x, y)^2 - \beta_2^2] = 0. \tag{2.2}$$

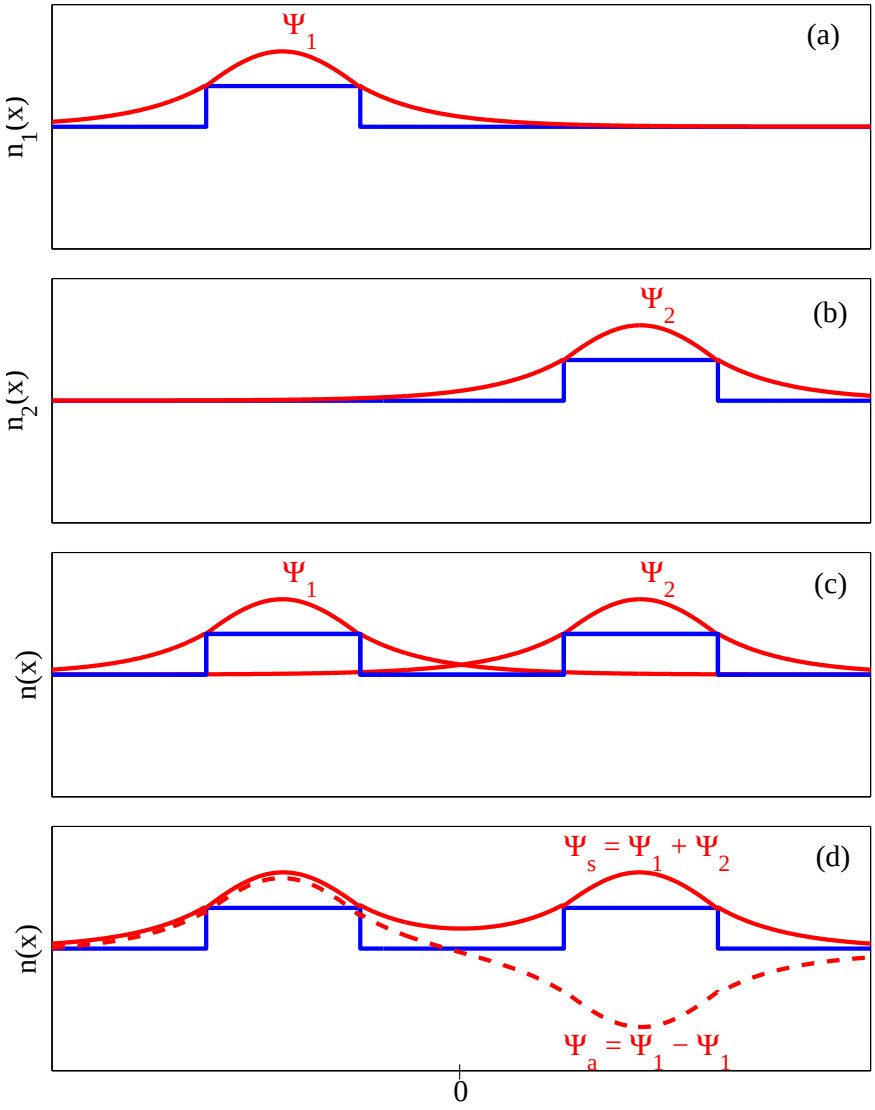

Figure 2.1: Schematic representation of the refractive index profiles, $n(x)$, (blue) and transverse mode profiles, $\Psi(x)$, (red) of the individual and composite waveguides. a) $n_1(x)$ and $\Psi_1(x)$ for waveguide 1 in isolation. b) $n_2(x)$ and $\Psi_2(x)$ for waveguide 2, identical to waveguide 1 but translated in x by a certain distance. c) $n(x)$ for the composite waveguide, along with $\Psi_1(x)$ and $\Psi_2(x)$ showing the overlap of each mode with the adjacent core. d) The resulting supermodes Ψ_s (solid curve) and Ψ_a (dashed curve) of the composite waveguide. As the sum or difference of Ψ_1 and Ψ_2 they possess definite symmetry and are often referred to as the symmetric and antisymmetric supermodes.

In a similar manner, the modes of the composite waveguide should be solutions of,

$$\nabla_T^2\Psi(x,y) + \frac{\partial^2\Psi(x,y)}{\partial z^2} + k_0 n(x,y)^2\Psi(x,y) = 0, \tag{2.3}$$

which is the scalar wave equation of the composite waveguide. It is then possible to make the tight-binding approximation, which is equivalent to looking for approximate solutions to Equation (2.3) of the from,

$$\Psi(x,y,z) = A_1(z)\Psi_1(x,y)e^{i\beta_1 z} + A_2(z)\Psi_2(x,y)e^{i\beta_2 z}, \tag{2.4}$$

where $A_1(z)$ and $A_2(z)$ are slowly varying envelopes that give the field amplitudes in each waveguide. Their dependence on z is due to the coupling between waveguides, caused by the overlap of the fields in each waveguide with the core of the other, see Fig. 2.1 (c). Substituting this trial solution into Equation (2.3) leads to,

$$\begin{aligned} A_1 e^{-i\beta_1 z}(\nabla_T^2\Psi_1 - \beta_1^2\Psi_1 + k_0^2 n^2\Psi_1) + A_2 e^{-i\beta_2 z}(\nabla_T^2\Psi_2 - \beta_2^2\Psi_2 + k_0^2 n^2\Psi_2) \\ -2i\beta_1\frac{\mathrm{d}A_1}{\mathrm{d}z}\Psi_1 e^{-i\beta_1 z} - 2i\beta_2\frac{\mathrm{d}A_2}{\mathrm{d}z}\Psi_2 e^{-i\beta_2 z} = 0, \end{aligned} \tag{2.5}$$

where, because $A(z)$ and $B(z)$ are slowly varying envelopes, terms containing their second order derivatives with respect to z have been ignored. Now, using equations (2.1) and (2.2) to substitute for $\nabla_T^2\Psi_1$ and $\nabla_T^2\Psi_2$ gives,

$$k_0^2\Delta n_1^2\Psi_1 + k_0^2\Delta n_2^2\Psi_2 e^{i\Delta\beta z} - 2i\beta_1\frac{\mathrm{d}A_1}{\mathrm{d}z}\Psi_1 - 2i\beta_2\frac{\mathrm{d}A_2}{\mathrm{d}z}\Psi_2 e^{i\Delta\beta} = 0, \tag{2.6}$$

where $\Delta n_1^2 = n^2 - n_1^2$, $\Delta n_2^2 = n^2 - n_2^2$ and $\Delta\beta = \beta_1 - \beta_2$. From here, multiplying Equation (2.6) by either Ψ_1^* or Ψ_2^* and integrating over the entire x-y plane leads to a pair of coupled differential equations,

$$\frac{\mathrm{d}A_1}{\mathrm{d}z} = -iC_{1,1} - iC_{1,2}Be^{i\Delta\beta z}, \tag{2.7}$$

and

$$\frac{\mathrm{d}A_2}{\mathrm{d}z} = -iC_{2,2} - iC_{2,1}Ae^{-i\Delta\beta z}, \tag{2.8}$$

where

$$C_{i,j} = \frac{k_0^2}{2\beta_i} \iint_{-\infty}^{+\infty} \Psi_i^* \Delta n_j^2 \Psi_j \, \mathrm{d}x\mathrm{d}y \tag{2.9}$$

are the coupling terms. The self-coupling terms, $C_{1,1}$ and $C_{2,2}$, can be considered negligible, which is reasonable since the integral in Equation 2.9 is only non-zero in the region where Δn_j is non-zero, which lies in the evanescent region where Ψ_j is small. Finally, having assumed identical waveguides means that $C_{1,2} = C_{2,1} = C$ and $\beta_1 = \beta_2 = \beta$, so that $\Delta\beta = 0$. Ignoring any frequency dependence and nonlinearity (the case of a low power, monochromatic input) A_1 and A_2 can be then be described using:

$$\frac{\mathrm{d}A_1}{\mathrm{d}z} = iCA_2, \tag{2.10}$$

and

$$\frac{\mathrm{d}A_2}{\mathrm{d}z} = iCA_1. \tag{2.11}$$

Solutions to the above can be found by assuming light is coupled into one waveguide only at $z = 0$, corresponding to the initial conditions $A_1(z = 0) = 1$ and $A_2(z = 0) = 0$, which leads to

$$A_1(z) = \cos(Cz) \tag{2.12}$$

and

$$A_2(z) = i\sin(Cz). \tag{2.13}$$

Equations (2.10) and (2.11) can be written in a different form by introducing complex amplitudes $a_1(z)$ and $a_2(z)$, where

$$a_1(z) = A_1(z)e^{-i\beta z} \tag{2.14}$$

and

$$a_2(z) = A_2(z)e^{-i\beta z}, \tag{2.15}$$

leading to

$$\frac{\mathrm{d}a_1(z)}{\mathrm{d}z} = -i\beta a_1(z) - iCa_2(z) \tag{2.16}$$

and

$$\frac{\mathrm{d}a_2(z)}{\mathrm{d}z} = -i\beta a_2(z) - iCa_1(z). \tag{2.17}$$

Is is then easy to show that the coupled equations admit modal solutions by noting that a mode will propagate without change except for phase, so that $a_1(z) = a_1e^{-i\beta z}$ and $a_2(z) = a_2e^{-i\beta z}$. Here the z dependence of a_1 and a_2 is now contained entirely within the complex phase term, as it should be for a mode, and β is now the propagation constant of a mode of the coupled system yet to be found. Substituting these expressions for a_1 and a_2 into equations (2.16) and (2.17) leads to a quadratic in β. Solving this yields the propagation constants of the symmetric, β_s, and the antisymmetric, β_a, supermodes,

$$\beta_s = \beta + C \tag{2.18}$$

and

$$\beta_a = \beta - C \tag{2.19}$$

where $\beta = \beta_1 = \beta_2$ is the propagation constant of an uncoupled waveguide, again assuming they are identical and ignoring any frequency dependence. Following this, it is possible to write the amplitudes of the symmetric supermode, A_s, and the antisymmetric supermode, A_a, as

$$A_s = \frac{1}{2}(A_1 + A_2) \tag{2.20}$$

and

$$A_a = \frac{1}{2}(A_1 - A_2). \tag{2.21}$$

As can be seen from equations (2.18) and (2.19), the propagation constants of each of the supermodes are different by an amount related to the strength of the coupling. The difference in propagation constants can be used to give an intuitive explanation for the transfer of light back and forth between waveguides. Light launched into a single waveguide at the input will excite a superposition of both supermodes, each of which will propagate with their own β. As the light propagates a phase difference accumulates between the light in each supermode, so that each waveguide alternately sees constructive and destructive interference. This supermode beating causes the amplitudes A_1 and A_2 to vary periodically with distance, leading to the back and forth transfer of light mentioned above. In most cases, but not all [80], C takes a positive value and so the symmetric supermode will possess a larger propagation constant than the antisymmetric. It is also worth noting that if only a single supermode is excited at the input, no supermode beating is possible and the amplitudes A_1 and A_2 will remain unchanged with propagation. Experimentally this could be achieved by tilting the input beam when coupling into an array, thus introducing a phase difference between the light in each of the wires [81].

Looking again at the expressions for A_1 and A_2 (Equations 2.12 and 2.13) it is clear that after a distance $z = \pi/2C$ all of the light has been transferred to waveguide 2, whilst after a distance $z = \pi/C$ all of the light has been coupled back into waveguide 1. This allows the distance over which the light couples from one waveguide to the next to be defined as,

$$L_c = \frac{\pi}{2|C|} = \frac{\pi}{|\beta_s - \beta_a|}. \tag{2.22}$$

This distance, known as the coupling length, provides a useful indicator as to the strength of the coupling between waveguides, as the stronger the coupling the shorter L_c.

2.1.2 Strong Guiding and Weak Coupling

The above approach, making use of the photonic tight-binding approximation, provides a simple, intuitive understanding of the coupling between waveguides, however it is assumed that the waveguides are both weakly guiding and weakly coupled. As was seen in Chapter 1 in the case of individual, uncoupled wires, the weak-guidance approximation breaks down due to the HIC and reduced waveguide dimensions. For the coupled-wire arrays considered in this chapter this is again the case, so that an accurate description of the supermodes of the array again requires numerical modelling using *COMSOL Multiphysics* ®. More details of the modelling process can be found below in this chapter.

Figure 2.2 shows the supermodes of a of pair 220 nm×380 nm wires with a wall-to-wall separation of 300 nm. For this separation it is clear that the modes of the coupled waveguides can still be well approximated as the symmetric and antisymmetric supermodes formed from linear superpositions of the individual wires, as described in the previous section (see Chapter 1 for modes of the individual wires). The effects of the strong guidance are evident however, as the supermodes possess mixed symmetry and polarisations and are no longer transverse.

2.1.3 Slot-modes - The Strong Guiding and Strongly Coupled Regime

As well as assuming weak guidance, the photonic tight-binding approach also assumes weak coupling, placing an upper limit on the coupling strength between waveguides[1]. For the wire arrays considered here this last point is particularly relevant, as when

[1]Note that weak coupling does not imply weak power transfer, as for two or more identical waveguides complete power transfer will occur for any coupling strength. Weaker coupling will simply lead to the power transfer occurring over a longer propagation distance i.e. longer L_c. Only for the case of non-identical, coupled waveguides will the power transfer be incomplete.

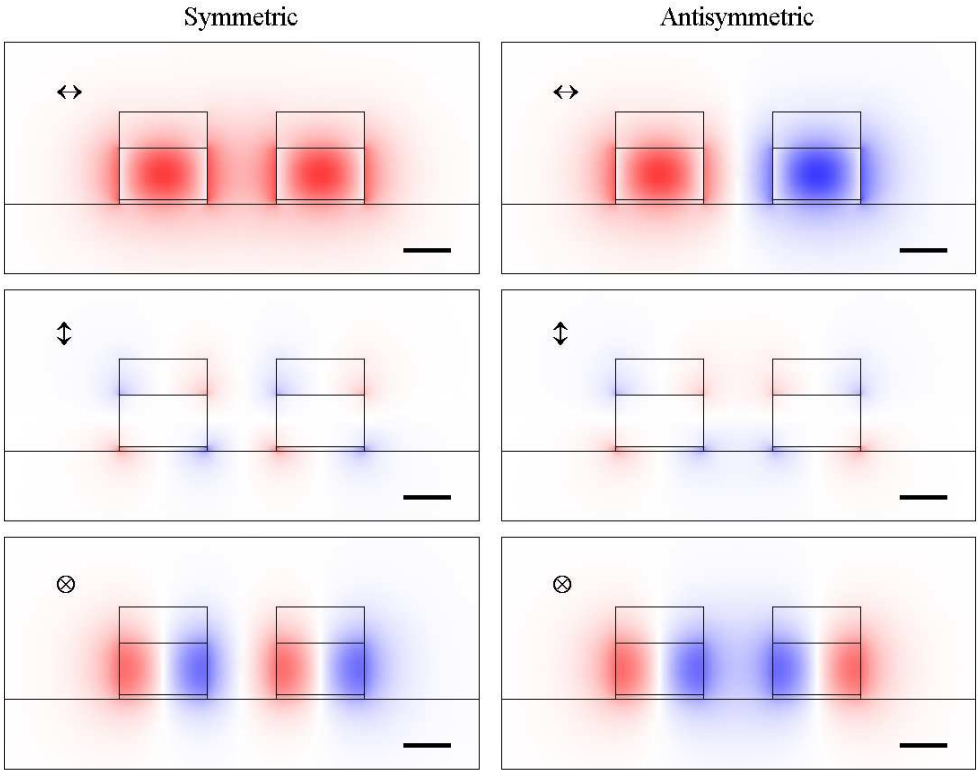

Figure 2.2: The symmetric (left) and antisymmetric (right) TE supermodes of a pair of coupled Si waveguides with heights of 220 nm, widths of 380 nm and a wall-to-wall separation of 300 nm at $\lambda = 1500$ nm. The $\vec{E}$ is split into Cartesian components, with the dominant component, E_x, parallel to the silica substrate shown top, E_y normal to the silica substrate shown middle and E_z pointing out of the page shown bottom. Colour saturation indicates magnitude with red (blue) representing positive (negative) values. The values of E_y have been scaled by a factor of 2 to make them visible on the same scale and the scale bar is 300 nm.

the wall-to-wall separation is reduced, or the wavelength is increased sufficiently, the coupling strength can increase dramatically and the above approximations break down. It is then possible for light to be confined in the low-index region between the wires in what is known as a slot-mode. First proposed by Lipson [82], slot modes arise because of the discontinuity of the electric field component normal to the Si-air interface (E_x). It can be shown that, due to the continuity of D_x normal to the Si-air interface, that E_x is larger by a factor of

$$\frac{n_{co}^2}{n_{cl}^2} \tag{2.23}$$

immediately inside the low index region, but still decays exponentially. The effect is highly pronounced in the case of the wires here due to their HIC, so that if two or more are brought sufficiently close together their evanescent fields overlap so much that E_x will remain high across the slots. It is for this reason that the TE supermodes are often of more interest, as they possess dominant field components normal to the Si-air interfaces at the vertical side-walls and are therefore capable of forming slot-modes.

Fig. 2.3 shows the effect of varying the coupling strength by changing the wall-to-wall separation of a two wire array. For a separation of 600 nm (Figs 2.3 ((a) and (b)) the modes of the array are well approximated as the symmetric and antisymmetric supermodes, formed from linear superpositions of the modes of the individual wires shown in Chapter 1 and predicted from the tight-binding approximation. The discontinuity of E_x at the interfaces is clearly evident for both supermodes. For a separation of 50 nm the supermode approach is no longer valid as E_x is now predominantly confined to the slots (Fig. 2.3 (c)). An identical situation would occur if the wall-to-wall separations were kept constant and instead λ was increased.

2.2 Coupling Induced Dispersion

The dispersion of a single SOI photonic wire can be tailored simply by altering its cross-sectional area, as shown by Fig. 1.6 in Chapter 1. In the case of arrays of coupled SOI photonic wires it has also been predicted that the coupling will become dispersive, adding an additional contribution to the net dispersion (waveguide and material) experienced by the supermodes of an array of wires. This provides an additional mechanism

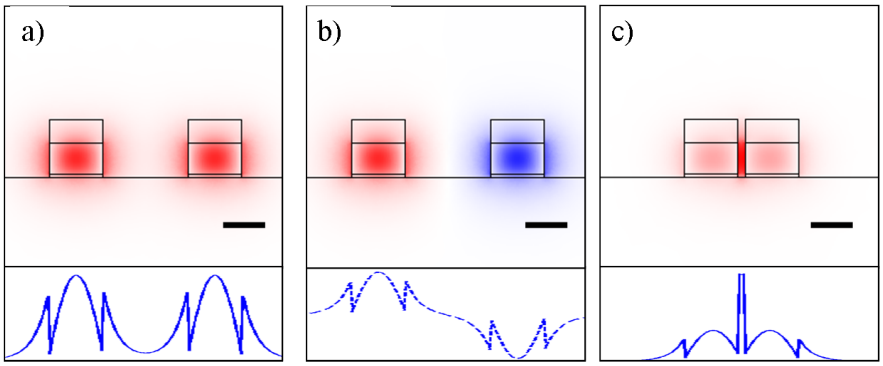

Figure 2.3: Component of the electric field parallel to the silica substrate (E_x) at $\lambda = 1550$ nm for (a) the symmetric supermode of a two channel array with a wall-to-wall separation of 600 nm and (b) the antisymmetric supermode of the same array. c) The same component of the electric field for a two-channel array with a 50 nm wall-to-wall separation. For this separation E_x remains high across the slot and the assumption of weak coupling is no longer valid, such that it is no longer possible to describe the modes of the system as linear superpositions of the individual waveguide modes. The wires have heights of 220 nm and widths of 380 nm and are shown over a $2 \times 2\,\mu$m area. Colour saturation indicates magnitude with red (blue)corresponding to positive (negative) values. The scale bar is 300 nm in each case. The line plots underneath each figure are a plot of E_x through the centre of the waveguides.

through which to tailor the dispersion of an array, as the strength of the coupling can be easily controlled by adjusting the spacing of the wires.

As discussed in Section 2.1.1, a directional coupler consisting of two coupled waveguides supports 2 supermodes of definite symmetry. The propagation constants of the supermodes are then given by the propagation constant of the mode of a single, uncoupled wire, plus or minus some contribution from the perturbation due to the coupling (equations (2.19) and (2.18)). The frequency dependence of the propagation constant of a single waveguide can be included by taking a Taylor expansion of β about the central frequency of the light in the wire, ω_0, as outlined in Chapter 1. It is then possible to use the same approach to include the frequency dependence of the coupling constant, C.

Assuming the evanescent waves decay exponentially outside the waveguide core and scale approximately with wavelength, the frequency dependence of the coupling coefficient C can be approximated by [58]

$$C(\omega) \approx C_0 e^{-x(\omega-\omega_0)} \tag{2.24}$$

where C_0 is the coupling strength at ω_0 and x is a positive constant related to the waveguide spacing. Taking a Taylor expansion in ω leads to

$$C(\omega) \approx C_0 + (-C_0 x)(\omega-\omega_0) + \frac{1}{2}(C_0 x^2)(\omega-\omega_0)^2 + \dots , \tag{2.25}$$

which can be rewritten as

$$C(\omega) \approx C_0 + C_1(\omega-\omega_0) + C_2(\omega-\omega_0)^2 + \dots , \tag{2.26}$$

where $C_m = (-1)^m C_0 x^m$. Typically, when taking into account the frequency dependence of directional couplers, only terms up to C_1 from the above expansion are included. However, for the Si wires considered here this is insufficient, as due to their close proximity the coupling strength is sensitive even to small changes in wavelength. The second derivative of the coupling is therefore substantial and it is necessary to include the quadratic term containing C_2. Thus the coupling now has a GVD of its own

that will contribute to the effective dispersion experienced by the supermodes. Rewriting the expressions for the propagations constants of the symmetric and antisymmetric supermodes (eqs. 2.18 and 2.19) to take into account the frequency dependence of β and C leads to the expressions,

$$\beta_s = \beta + C$$
$$\beta_s = (\beta_0 + C_0)(\omega - \omega_0) + (\beta_1 + C_1)(\omega - \omega_0)^2 + (\beta_2 + C_2)(\omega - \omega_0)^2 + ... \quad (2.27)$$

and

$$\beta_a = \beta - C$$
$$\beta_a = (\beta_0 - C_0)(\omega - \omega_0) + (\beta_1 - C_1)(\omega - \omega_0)^2 + (\beta_2 - C_2)(\omega - \omega_0)^2 + ... \, . \quad (2.28)$$

The expressions for $\beta(\omega)$ and $C(\omega)$ can be converted to the time domain through a Fourier Transform and included in equations (2.10) and (2.11), yielding

$$\frac{\partial A_1}{\partial z} + \beta_1 \frac{\partial A_1}{\partial t} + \frac{i\beta_2}{2}\frac{\partial^2 A_1}{\partial t^2} + C_1 \frac{\partial A_2}{\partial t} + \frac{iC_2}{2}\frac{\partial^2 A_2}{\partial t^2} = iC_0 A_2 \quad (2.29)$$

$$\frac{\partial A_2}{\partial z} + \beta_1 \frac{\partial A_2}{\partial t} + \frac{i\beta_2}{2}\frac{\partial^2 A_2}{\partial t^2} + C_1 \frac{\partial A_1}{\partial t} + \frac{iC_2}{2}\frac{\partial^2 A_1}{\partial t^2} = iC_0 A_1. \quad (2.30)$$

By adding or subtracting equations (2.29) and (2.30) and making use of equations (2.20) and (2.21) from Section 2.1.1, the coupled equations can be written in terms of supermodal amplitudes as:

$$\frac{\partial A_s}{\partial z} + [\beta_1 + C_1]\frac{\partial A_s}{\partial t} + \frac{i}{2}[\beta_2 + C_2]\frac{\partial^2 A_s}{\partial t^2} = \frac{i}{2}C_0 A_s \quad (2.31)$$

$$\frac{\partial A_a}{\partial z} + [\beta_1 - C_1]\frac{\partial A_a}{\partial t} + \frac{i}{2}[\beta_2 - C_2]\frac{\partial^2 A_a}{\partial t^2} = -\frac{i}{2}C_0 A_a \quad (2.32)$$

From these expressions the effects of including the frequency dependence of $C(\omega)$ are clear. Retaining only C_0 from the Taylor expansion of $C(\omega)$ (i.e. no frequency dependence) leads to supermodes that propagate with different phase velocities, related to $\beta_0 \pm C_0$, but the same group velocity. Including C_1 means the supermodes will now propagate with different phase and group velocities, related to $\beta_1 \pm C_1$. Consequently, a single pulse incident on a two wire array and exciting both supermodes would split into two sub-pulses after a few coupling lengths, with the separation continuing to increase with propagation. The envelopes of the sub-pulses would, however, remain unchanged from that of the input pulse. Finally, including the quadratic term containing C_2 equates to modifying the effective dispersion experienced by each supermode; β_2 becomes $\beta_2 \pm C_2$. Light in each supermode will therefore propagate with different phase and group velocities and experience different effective dispersions.

Due to the positive sign of C_2 it is therefore predicted [83] that the region of anomalous GVD will be restricted for the symmetric supermode and extended for the antisymmetric supermode, relative to that of a single wire. Physically this can be understood by considering the relative phases of the light in the two wires for each of the supermodes. In the case of the antisymmetric supermode there is a π-phase difference between the fields in each wire, so that the fields of the antisymmetric supermode are therefore 'pinned' at zero in the center of the slot region between the wires. As the wavelength of the light being confined increases, the expansion of the antisymmetric mode is therefore restricted by the pinning point. Consequently the effects of confinement within the wire are felt more strongly by the antisymmetric supermode, so that its dispersion is shifted further into the anomalous regime (since it is the confinement by the waveguide that causes the anomalous dispersion at these wavelengths). By contrast, the symmetric supermode has no such pinning point and so the mode can expand more easily, thereby reducing the effects of confinement and shifting its dispersion further into the normal relative to a single wire. For an odd number of wires in an array there is also a supermode that corresponds to having no light in alternate wires. In this case the effective coupling is very small and the supermodes possess the same dispersion relation as that of a single, uncoupled wire.

2.3 Group Index Measurements

In order to verify the above prediction, group index measurements were taken for a two wire array and compared to numerically modelled data. A two wire array would be

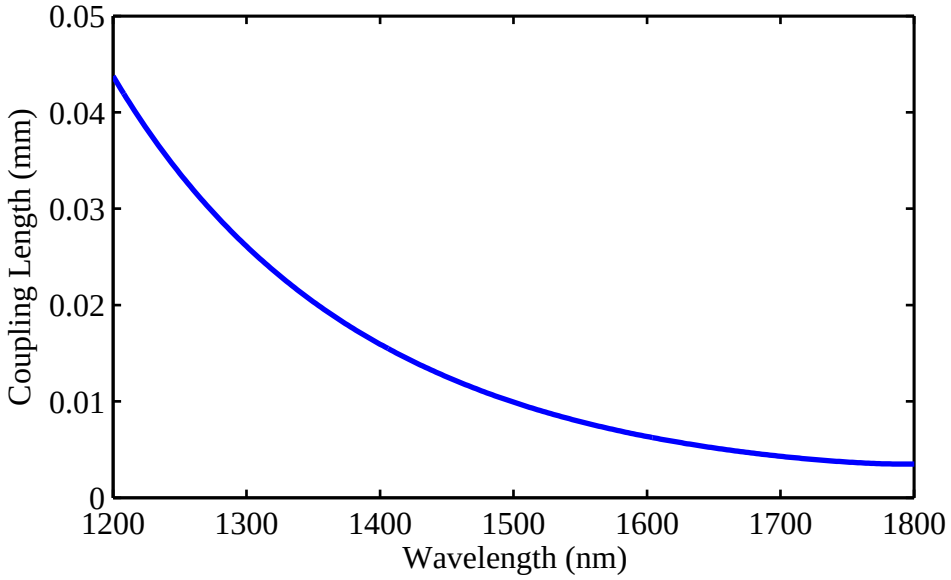

Figure 2.4: Calculated coupling, L_c, as a function of wavelength for a 2 channel array with a 100 nm wall-to-wall separation, as used in the experiments.

expected to support 2 supermodes (one symmetric and one antisymmetric) for each of the TE and TM polarizations. In this case we are more interested in the TE supermodes that have their principal $\vec{E}$ components normal to the Si-air interface, since these are the modes that could form slot-modes. The array used for the measurements was fabricated in the manner detailed in Chapter 1 and consisted of two wires, each with heights of 220 nm, widths of 380 nm and a wall-to-wall separation of 100 nm. This separation, an order of magnitude smaller than the wavelengths of the light being confined, was chosen in the hope that, over the spectral range investigated, it would be possible to observe not only strong coupling-induced dispersion, but also the transition to slot-modes. An indication of the strength of the coupling can be obtained by looking at the values of L_c for the chosen geometry, calculated using Equation (2.22) and shown in Fig. 2.4. Here L_c is of the order of just a few tens of microns, demonstrating the wires are strongly coupled.

2.3.1 Experimental Methods

The potential for white-light to be used to measure the dispersive properties of materials has been known for some time [84, 85, 86]. Often, the method involves multiple

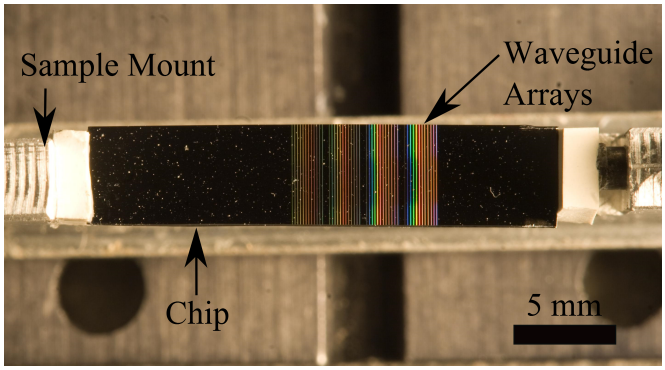

Figure 2.5: Top down view of the sample mounted in the experimental set-up. The arrays are visible as the individual coloured lines as they behave like a grating when illuminated by white light.

measurements of the centre of an interference pattern from a spectrally filtered white-light source [84, 85], which is the method used here. An image of the sample mounted in the experimental set-up is shown in Fig. 2.5. For an overview of the layout of the devices fabricated on the chip please see Appendix A. Low coherence white-light interferometry was performed using a Mach-Zehnder interferometer, as shown in Fig. 2.6. This configuration was preferred to a Michelson interferometer, which would have been more difficult to align and resulted in higher coupling losses, due to the need for light to pass through the sample twice.

The light source was a 1064 nm Q-switched microchip laser (average power < 100 mW, $\tau \sim 600$ ps, PRF ~ 7.25 kHz) used in conjunction with a length of highly nonlinear PCF [87]. This provided a broadband output from approximately 400 to 2200 nm. Wavelengths below 1200 nm were removed using a long pass filter to prevent damage to the arrays as the absorption of Si increases dramatically below 1200 nm, with the desired wavelengths selected using band pass filters with 10 nm full-width half-maxima.

After the initial filtering light was passed through a 50:50 beam splitter so that half of the light was directed to the sample and half was sent along the reference arm. A matched pair of 60× aspheric singlet lenses (NA = 0.65, *New Focus*; Model 5721-H) were used to couple into and out of the array with total losses of 20 dB, determined by measuring the power before the input lens and after the output lens. Reproducible coupling was ensured through the use of an IR charge-coupled device (CCD) camera (*Xenics*; Xeva), mounted initially above the array on a microscope in order to image top scattered light. Once the correct array had been located and coupled into, the

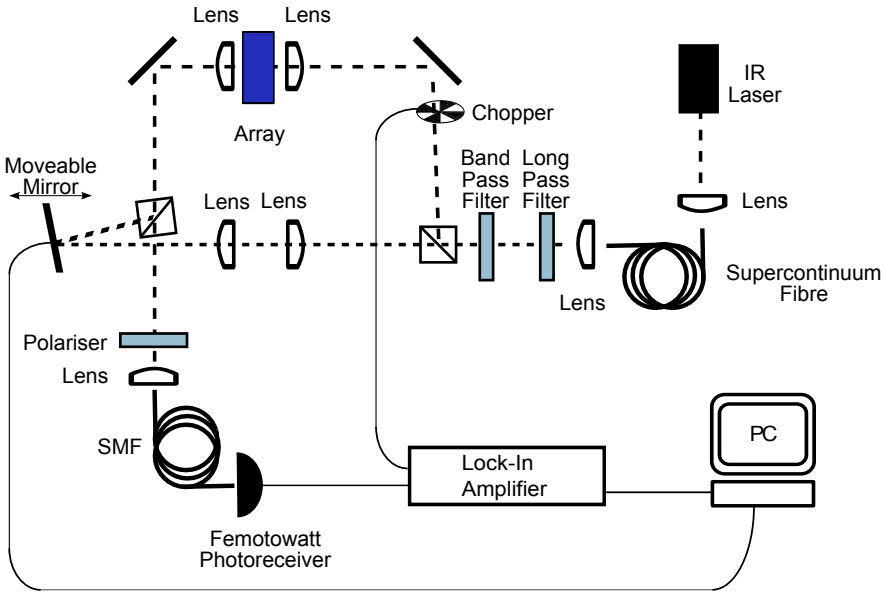

Figure 2.6: Experimental set-up for group index measurements. Light from the broadband source is filtered at the desired central wavelength using 10 nm band-pass filters and the beam is then split at a 50:50 beam splitter cube, so that some light propagates through the reference arm and some propagates through the array. The delay of the reference arm is controlled by a mirror mounted on a translation stage, before the beams are re-combined at a second 50:50 beam splitter and collected using a length of single mode fibre (SMF).

output could then be directed onto the same CCD camera in order to image the output from the waveguides. Coupling was optimized simply by adjusting the position of the input and output lenses until the maximum transmitted power was reached. Identical lenses were positioned in the reference arm of the interferometer, in order to balance any effects of dispersion caused by the lenses in the sample arm.

In a balanced interferometer, i.e. one in which the optical path-length in each arm is equal, the pulses would recombine and interfere constructively. Changing the optical path-length in either arm introduces a phase-difference between the light in each. In the sample arm this change is caused by the dispersion of the sample, which is compensated for in the reference arm by introducing a delay by changing its physical length through the use of a plane mirror mounted on a computer-controlled translation stage. As a single mirror was used, as opposed to a pair of mirrors, there was a possibility that the interferometer may become misaligned as the mirror was moved. However, as the distances over which the mirror was moved were of the order of millimetres there was no significant effect on the performance of the interferometer. The beams were recombined

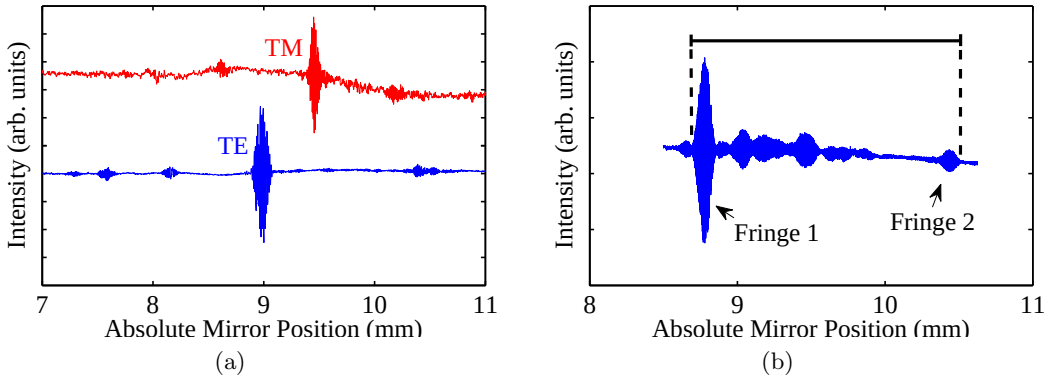

Figure 2.7: a) Successful isolation of the TE (blue) and TM (red) fringe packets at λ = 1240 nm using a polarizing beam splitter cube. Note the TM fringe packet is offset from the TE on the vertical scale for clarity. b) TE fringe at λ = 1600 nm. The capped horizontal bar indicates the full width at background intensity of the fringe.

at a second beam splitter cube and interfered to generate interference fringe packets. The change in length of the reference arm for each fringe compared to when no sample is present could then be related to group index.

A polarizing beam splitter after the array was used to isolate either the TE or TM fringe packets, as shown in Fig. 2.7 (a), before the light was collected using a length of standard single mode fibre. Detection was performed using an InGaAs PIN photodiode (*New Focus* Femtowatt Photoreceiver; Model 2153) and lock-in amplifier (*Stanford Research Systems*; SR830 DSP), referenced to an optical chopper positioned in the sample arm to aid sensitivity. For wavelengths above 1800 nm is was necessary to switch to an unbiased, transimpedance, InGaAs photodiode (*Thorlabs*; DET10D/M), which had an increased spectral range for sufficient responsivity at longer wavelengths. In total, fringes corresponding to the TE and TM supermodes at 17 filter wavelengths between 1200 and 2000 nm were recorded.

As mentioned above, measurements are usually taken of the mirror positions corresponding to the centre of the interference fringe at each wavelength [84, 85]. In this case however, the spectrally filtered input pulse is being coupled into an array supporting two supermodes that should experience different dispersions due to the strong coupling between waveguides. One may therefore expect to see two separate interference fringes for which the centre positions can be measured, corresponding to light

that has propagated in either the symmetric or anti-symmetric supermodes of the array. This of course relies on the fringes being sufficiently separated as to be distinct from each other, which in turn relies on the strength of the coupling-induced dispersion, with larger values giving rise to a bigger fringe separation. Unfortunately it was not possible to completely resolve the individual fringes. At shorter wavelengths where the coupling, and hence coupling-induced dispersion, was small, the difference in n_g between the supermodes was also small, so that the fringes corresponding to each supermode occurred at almost identical mirror positions and remained largely overlapped (see Fig.2.9 (a)). Further, at wavelengths corresponding to the largest differences in n_g between the supermodes it was still not possible to completely resolve the individual fringes due to the appearance of a strongly modulated background, possibly caused by the scattering of light at defects or due to side-wall roughness. This can be seen clearly in Fig. 2.7 (b), which shows the TE fringe packet at $\lambda = 1600$ nm (corresponding to a large difference in n_g), where two fringes can be identified that are separated by a long, modulated background. For these reasons the measured interference patterns were characterized not by measuring the centre of the fringes, but by recording the mirror positions of their full-width at background intensity instead. In this case it is assumed that the part of the interference pattern located at the shortest (longest) reference arm position is associated with the supermode with the lowest (highest) group index. Thus the width of the measured interference pattern can also be used to determine the group index, with a broadening of the interference pattern indicating supermodes propagating with increasingly different group velocities, caused by the presence of coupling-induced group velocity dispersion. Note in this case the 'background intensity' is taken as the signal measured at a point immediately outside the fringe packet where no interference is occurring. The horizontal bar in Fig. 2.7 (b) indicates the region defined as the full-width at background intensity for this particular fringe packet.

It should be noted however, that this measurement set-up actually measures the group-delay, the temporal delay in travelling through a material at a given mode's group velocity. However, once known, the delay corresponding to the mirror positions of the fringe's full-width at background intensity could straightforwardly be related to group index via the equation,

$$n_g = \frac{2(x - x_0)}{L} + 1 \tag{2.33}$$

where x_0 was the position of the centre of the fringe observed without a sample present and the length, L, of each of the wires was 3.1 mm. Although perhaps not an ideal

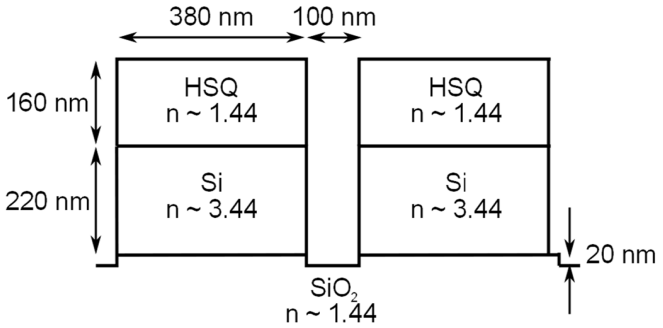

Figure 2.8: Geometry used for modelling the two channel array in the experiment. The wires were assumed to be 220 nm×380 nm with a wall-to-wall separation of 100 nm and a 160 nm thick layer of residual HSQ. Note also the 20 nm over-etch to ensure the wires were sufficiently etched through.

way of characterising the fringes, the calculated values of n_g were insensitive to small variations (of the order of microns) in the measured mirror positions, suggesting the method was suitably robust.

2.3.2 Numerical Modelling

The modelling of the two wire array was performed using a commercial eigenvalue solver, *COMSOL Multiphysics* ®. Maxwell's equations were solved for an idealized geometry, shown in Fig. 2.8, with the appropriate boundary conditions to yield the supermode propagation constants and effective indices. Is was assumed that: the dimensions of the wires were those asked for; the side-walls of the wires were perfectly vertical and the channel was completely etched through. The region around the array was air with $n = 1$ and the material dispersions of Si and silica were incorporated into the model by using equations (1.23) and (1.22) from Chapter 1. HSQ was assumed to have the same n as silica. The modelled effective indices could then be numerically differentiated to obtain values of n_g for each of the supermodes.

2.4 Results

The measured fringe packets for the TE supermodes clearly indicate the presence of coupling-induced dispersion; Fig. 2.9. At shorter wavelengths (Fig. 2.9 (a)) the modes of the wires are more confined and there is less overlap of the evanescent fields, reducing

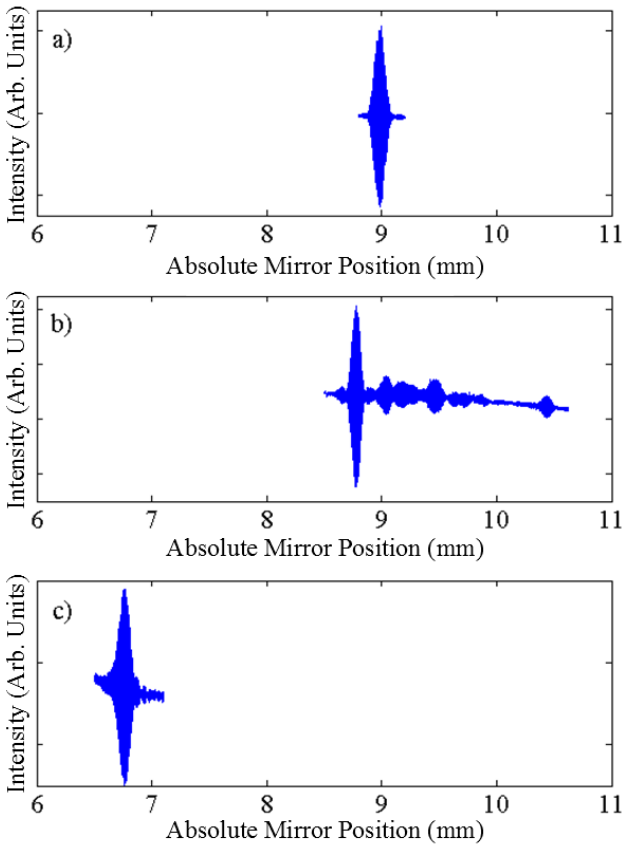

Figure 2.9: Measured fringe packets for the TE supermodes at a) $\lambda = 1240$ nm, b) $\lambda = 1600$ nm and c) $\lambda = 2000$ nm. The broadening of the fringe due to coupling-induced dispersion is clearly visible at 1600 nm, while at 2000 nm the fringe packet appears to be a single mode interferogram, suggesting the cut-off of one of the TE supermodes.

the coupling between them and therefore the coupling-induced dispersion. In this regime the supermodes propagate with almost identical group velocities, so that the fringes due to the symmetric and antisymmetric TE supermodes overlap temporally and occur at the same mirror positions. As wavelength increases however, so too does the strength of the coupling and consequently the coupling-induced dispersion. The supermodes will therefore propagate with increasingly different group indices as they experience different dispersions, leading to a broadening of the fringe packet clearly observed in Fig. 2.9 (b) for $\lambda = 1600$ nm. Two distinct peaks are visible, separated by a long modulated background intensity, which could be due to intermodal scattering caused by side-wall roughness [88], dust on the samples, stitching errors during the fabrication process or other defects along the arrays.

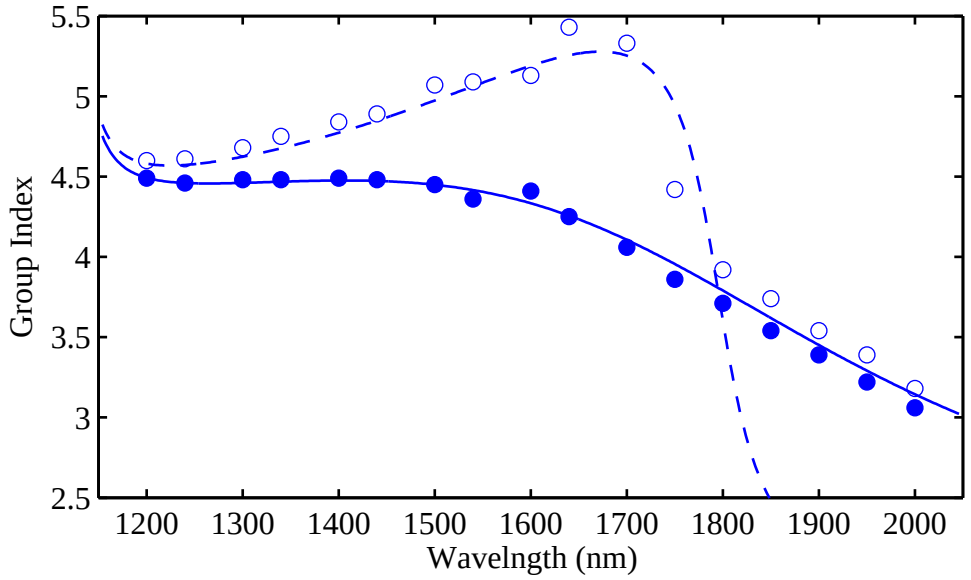

Figure 2.10: Group index measurements for the TE supermodes of the two wire array. The filled and unfilled circles correspond to the experimentally measured group indices of the symmetric and antisymmetric respectively, determined from the fringe packets full-width at background intensity. The solid and dashed curves are the numerically modelled group indices for the symmetric and antisymmetric supermode respectively. Above approximately 1800 nm the antisymmetric supermode has been cut-off, explaining the discrepancy between the modelled and measured group index data.

The measured fringes were used to calculate n_g for the symmetric and antisymmetric TE supermodes (using Equation (2.33)) and are compared to the numerically modelled data in Fig. 2.10. The experimental and modelled results show good agreement and highlight an increasing difference in n_g between the TE supermodes up to $\approx 1700\,\text{nm}$. At this point, according to the modelled data, the n_g of the antisymmetric mode decreases rapidly and falls below the curve for the n_g of the symmetric mode. Experimentally, above 1900 nm the measured fringe packet resembles a single interferogram, as can be seen in Fig. 2.9 (c) for $\lambda = 2000$ nm. Both the modelled and experimental data thus suggest that one of the supermodes has become cut-off by ≈ 1850 nm.

2.5 Analysis

Both the experimental and theoretical results confirm the presence of coupling-induced dispersion through the broadening of the fringe packets (Fig. 2.9) and subsequent splitting of the symmetric and antisymmetric supermodes on the n_g plot (Fig. 2.10). Close agreement between the experimental and modelled data in Fig. 2.10, in terms of both absolute n_g and splitting of the supermodes, suggests that light in the fringe packets at the furthest mirror positions (largest n_g) can be viewed as light that has propagated along the entire array in the antisymmetric TE supermode. While light in the fringe packet at the shortest mirror positions (lowest n_g) has propagated through the arrays in the symmetric TE supermode only. The largest difference in group indices between the symmetric and antisymmetric supermodes occurs at $\approx 1700\,\text{nm}$, which is also the point at which the antisymmetric mode begins to experience normal dispersion (n_g decreases with wavelength). By contrast, the point at which the symmetric supermode begins to experience normal dispersion occurs at $\approx 1400\,\text{nm}$. In other words, the region of anomalous dispersion has been extended for the antisymmetric supermode and suppressed for the symmetric supermode relative to a single, uncoupled wire of the same dimensions, as previously predicted in [83].

The effect of the coupling-induced dispersion can be seen more clearly by plotting the dispersion curves for each of the supermodes. This can be done by differentiating the group index data according to Equation 1.21. Unfortunately, due to the slight scatter on the experimentally obtained group index measurements, it was not possible to differentiate them numerically, whilst the relatively limited number of data points made a numerical fit difficult. Thus only the modelled group index data was differentiated to obtain dispersion. Figure 2.11 shows the calculated dispersion curves for the symmetric and antisymmetric TE supermodes, along with the dispersion of the TE mode of a single wire with the same transverse dimensions (220 nm $\times$ 380 nm). It is interesting to note from this plot that the splitting of the two supermodes is not symmetric with respect to the the dispersion of a single wire, as would be predicted by the tight-binding model, with the asymmetry more pronounced at longer wavelengths. The dispersion of the symmetric supermode (blue curve) seems to differ more significantly from that of a single-uncoupled wire (black curve) than the that of the antisymmetric supermode (dashed blue curve). The coupling induced dispersion thus seems to be having a much stronger impact on the symmetric supermode. The failure of the tight-binding model to predict such asymmetric splitting is perhaps understandable however, as it assumes weak-coupling. By contrast, the 100 nm wall-to-wall separation was specifically chosen to ensure strong coupling in an attempt to observe slot modes. It is therefore not

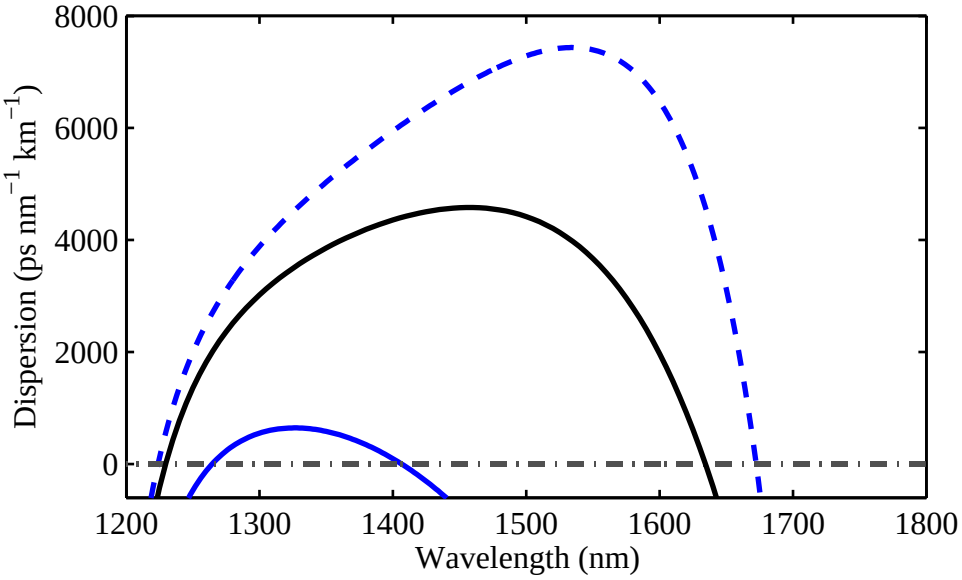

Figure 2.11: Modelled results for the dispersion of the symmetric (blue) and antisymmetric (dashed blue) TE supermodes. For comparison, the dispersion of the TE mode of a single, uncoupled wire with the same transverse dimensions is also shown (black).

surprising that for such a small wall-to-wall separation the tight-binding model fails to accurately predict the dispersive properties of the array supermodes.

The cut-off of the antisymmetric supermode, evidenced by the appearance of the experimental fringe packet above 1900 nm (Fig. 2.9) and by the rapid fall in n_g of the antisymmetric supermode as λ approaches 1900 nm, can be understood with reference to the modelled effective index data, shown in Fig. 2.12. The data show that by $\lambda =$ 1900 nm the n_{eff} of the antisymmetric mode has fallen to that of the bottom silica cladding, while for a guided mode n_{eff} must be greater than or equal to the cladding index. By 1900 nm the antisymmetric mode is thus only weakly confined to the wires, is highly lossy and no longer a truly bound mode of the waveguides; it has become cut-off. Physically this arises because the wavelength of the light is now too large to be confined within the wires. The field can no longer undergo the oscillation in phase between wires required to remain within the antisymmetric supermode, the fields of which are pinned at zero in the slot. The symmetric TE supermode can however continue to expand and remains sufficiently confined to continue to propagate as a guided mode.

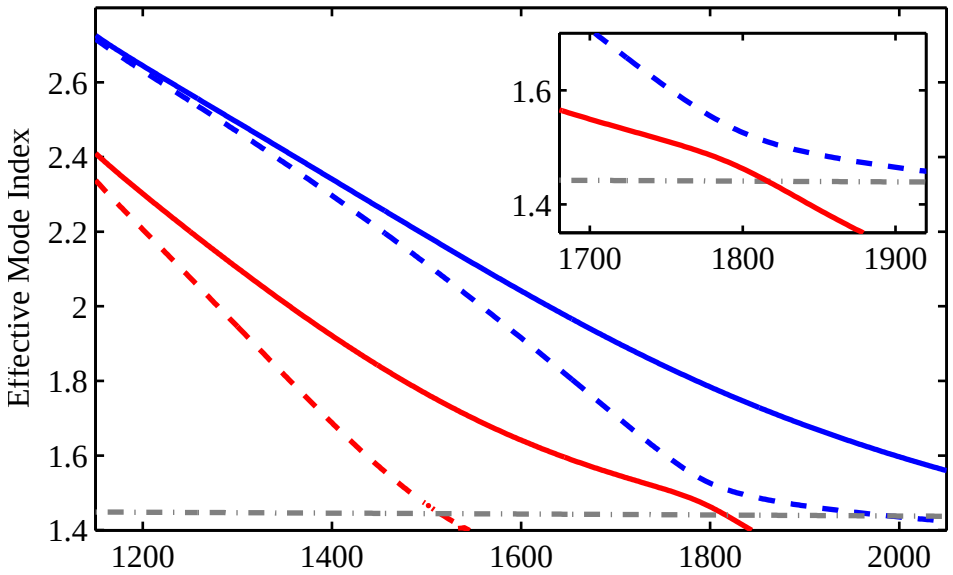

Figure 2.12: Modelled results for the n_{eff} of the TE (blue) and TM (red) supermodes where the solid and dashed lines correspond to the symmetric and antisymmetric supermodes respectively. The grey dashed line indicates the n of bulk silica. The inset shows a close up of the anti-crossing between antisymmetric TE and symmetric TM supermodes.

One can also ask what the field distribution of the only remaining supermode looks like for $\lambda > 1900$ nm, when all but the symmetric TE supermode has been cut-off. The modelled field distributions for the transverse component of $\vec{E}$ and Poynting vector, S, are shown in Fig. 2.13. The discontinuity of the transverse component of $\vec{E}$ at the Si-air interfaces is evident for both supermodes at 1400 nm. The antisymmetric supermode is however, as stated previously, pinned at zero in the slot region, due to the π-phase shift between the fields in each wire (Fig. 2.13 (a)). Thus this supermode cannot form a slot mode, as both $\vec{E}$ and $\vec{H}$ remain negligible in the low-index slot region, meaning the power flow (given by the Poynting vector, $\vec{S} = \vec{E} \times \vec{H}$) is confined within the wires until the supermode becomes cut-off. The situation is different for the symmetric supermode as there is no phase shift between the fields in each wire, so they both point in the same direction and $\vec{E}$ remains high across the slot. The transverse component of $\vec{E}$ therefore has the characteristic appearance of a slot mode (Fig. 2.13 (b) and (c)). It is interesting to note however that although $\vec{E}$ remains high across the slot for the symmetric supermode at $\lambda = 1400$ nm, the Poynting vector is only non-zero in the wires, there is no power flow in the slot. This is easily explained by the fact that at this wavelength, although $\vec{E}$ in the slot is large, $\vec{H}$ is still confined entirely within the

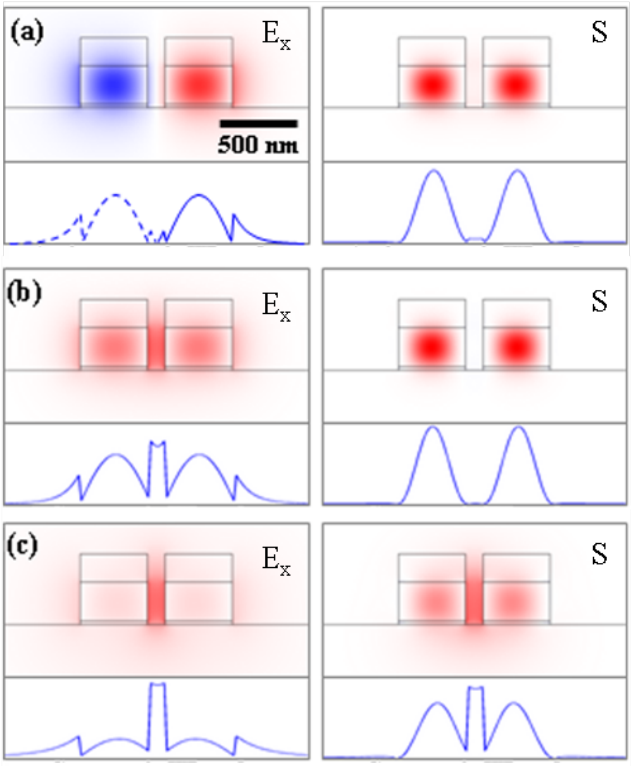

Figure 2.13: Modelled field distributions of the transverse electric field component (left column) and the Poynting vector (right column) for a) the antisymmetric TE supermode at $\lambda = 1400$ nm b) the symmetric TE supermode at $\lambda = 1400$ nm and c) the symmetric TE supermode at $\lambda = 1950$ nm. The line plots are plots of the magnitude of each of the quantities through the centre of the arrays, with the dashed line indicating opposite phase.

wires, so that $\vec{S} = \vec{E} \times \vec{H}$ is zero in the slot. At longer wavelengths $\vec{H}$ becomes less confined and leaks into the slot, so that $\vec{E} \times \vec{H}$ becomes non-zero, until at $\lambda = 1950$ nm there is equal peak intensity in the slot and wires. It can therefore be assumed that by 1950 nm the only remaining supermode, the symmetric TE, is propagating as a slot mode with power as well as $\vec{E}$ within the slots.

Another interesting feature of the modelled data is the predicted anti-crossing between the antisymmetric TE and symmetric TM supermodes of the array as they approach cut-off. Anti-crossings, or avoided-crossings, occur in optics when the effective index of a particular mode approaches that of another with the same symmetry. Should the modes ever have the same effective index at any point they would be degenerate; this is forbidden. This degeneracy (both modes possessing the same effective index) is therefore avoided as the modes undergo a conversion from one to the other at an

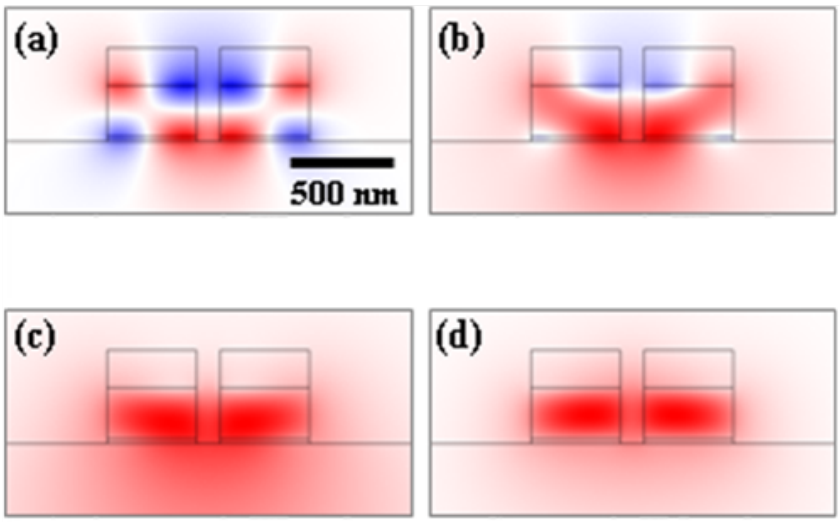

Figure 2.14: Modelled mode profiles showing the transverse component of the magnetic field (H_x, parallel to the silica substrate) of the antisymmetric TE supermode at a) $\lambda = 1650$ nm, b) $\lambda = 1790$ nm and c) $\lambda = 1950$ nm. For comparison the same component of the symmetric TM supermode is shown at d) $\lambda = 1650$ nm.

anti-crossing. Evidence for the existence of an anti-crossing in this system can be seen by looking at Fig. 2.12. The effective index of the highly dispersive antisymmetric TE supermode begins to fall rapidly above 1600 nm and approaches that of the symmetric TM supermode at 1800 nm. The inset of Fig. 2.12 shows this region in more detail, where at 1800 nm there is a clear avoided crossing between the two supermodes as they cannot possess the same effective index. Initially this may seem surprising however, as in general for an anti-crossing to occur there must be some coupling between the modes. This would seem unlikely in this instance, as the supermodes have different polarizations and are of opposite symmetry. Both supermodes do however possess symmetric magnetic field components parallel to the silica substrate (H_x), which can couple due to the asymmetric mode confinement. The presence of the silica substrate below the Si wire, and the HSQ layer above, leads to weaker confinement in the vertical direction due to the lower index contrast between Si and HSQ and Si and silica. Consequently, as the wavelength of the light being confined increases, the supermodes expand more rapidly in the vertical direction. This allows the antisymmetric TE supermode to undergo a transition to the symmetric TM supermode, and vice-versa, via an anti-crossing. The evolution of H_x for the antisymmetric TE supermode through the anti-crossing, along with H_x for the symmetric TM supermode, is shown in Fig. 2.14.

2.6 Sample Imaging

As was highlighted in the previous sections, the presence of multiple fringes that created a modulated background (see Fig. 2.7 (b)) prevented the complete isolation of the individual fringes corresponding to the symmetric and antisymmetric TE supermodes. It was assumed that these additional fringes were caused by intermodal scattering, leading to light that had propagated along the arrays in both the symmetric and antisymmetric TE supermodes. Thus the light at the outer edges of the fringe packet would have propagated along the array entirely within either the symmetric or antisymmetric supermode, whilst the additional fringes in between would correspond to light that had propagated along the array in both supermodes to a greater or lesser extent.

In an attempt to gain further understanding a brief investigation was undertaken, with the outputs of a larger array imaged using the same IR CCD camera used previously for input and output coupling. The chosen array consisted of fifteen 420 nm$\times$220 nm wires with wall-to-wall separations of 600 nm. The increased separation compared to the array used previously for the dispersion measurements ensured weaker coupling and a larger L_c, estimated at 1.2 mm for the 1510 nm input wavelength used here. Given the length of the wires in the array is $\sim$3 mm, this should mean that there is insufficient distance for light coupled into an edge wire at the input to couple across to the opposite side of the array at the output.

The output images shown in Fig. 2.16 were recorded by placing a mirror after the output coupling lens and directing the light onto the IR CCD camera, whilst the input lens was translated across the input face of the array, as shown in Fig. 2.15. It is important to note however that, given the array dimensions and the wavelength of light used for the imaging, it was not possible to resolve the outputs from individual wires in the array. The movement of the input coupling lens across the array was achieved by mounting it on a piezo controlled stage, allowing the focussed laser spot to be moved across the array input from left to right in $\sim$600 nm steps. Given no method of feedback was used however, it was impossible to know in absolute terms the position of the input lens relative to the array. At the same time, the minimum diameter of the focussed laser was estimated at approximately 1500 nm, assuming a collimated beam that filled the clear aperture of the input lens. Consequently there was the potential

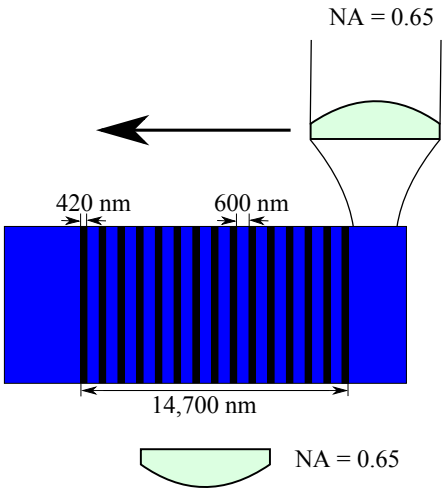

Figure 2.15: Cartoon showing the set-up used to image the outputs of the 15 wire array. The individual wires in the array were 420 nm wide with wall-to-wall separations of 600 nm, giving a total device width of 14.7 µm. The input coupling lens was translated across the face of the array in ∼600 nm steps, with images taken at the output using the IR CCD camera used previously. Note that the set-up did not allow for the resolution of the outputs from individual wires, whilst it was also not possible to identify quantitatively where the input beam was in relation to the wires in the array. Diagram not to scale.

for more than one wire to be excited at the input (given the 600 nm wire spacing). The lens used at the output of the array had a focal length of 2.8 mm, giving a ratio of object distance to focal length of 611. Each 30 µm camera pixel therefore represented approximately 50 nm of image distance, so that an individual wire in the array would be just 4 pixels high and 8 wide. The camera array itself was 320 pixels wide and 100 pixels high.

Despite the limitations of the imaging set-up outlined above, one would still expect, in the absence of scattering, to see symmetric output field patterns as the input lens is moved across the array. More specifically, the output images obtained as the lens is moved from the left hand edge of the array to the centre should be the mirror image of what is observed as the lens is moved from the centre to the right hand edge, given the symmetry of the array structure. This is clearly not observed in any of the images shown in Fig. 2.16, suggesting the possibility of considerable scattering occurring along the length of the array. In addition, Figs. 2.16 (d) and (e) show light exiting the array from both edges whilst the input lens is coupled into the edge of the array at this point. This should be impossible given the ratio of L_c to wire length as discussed

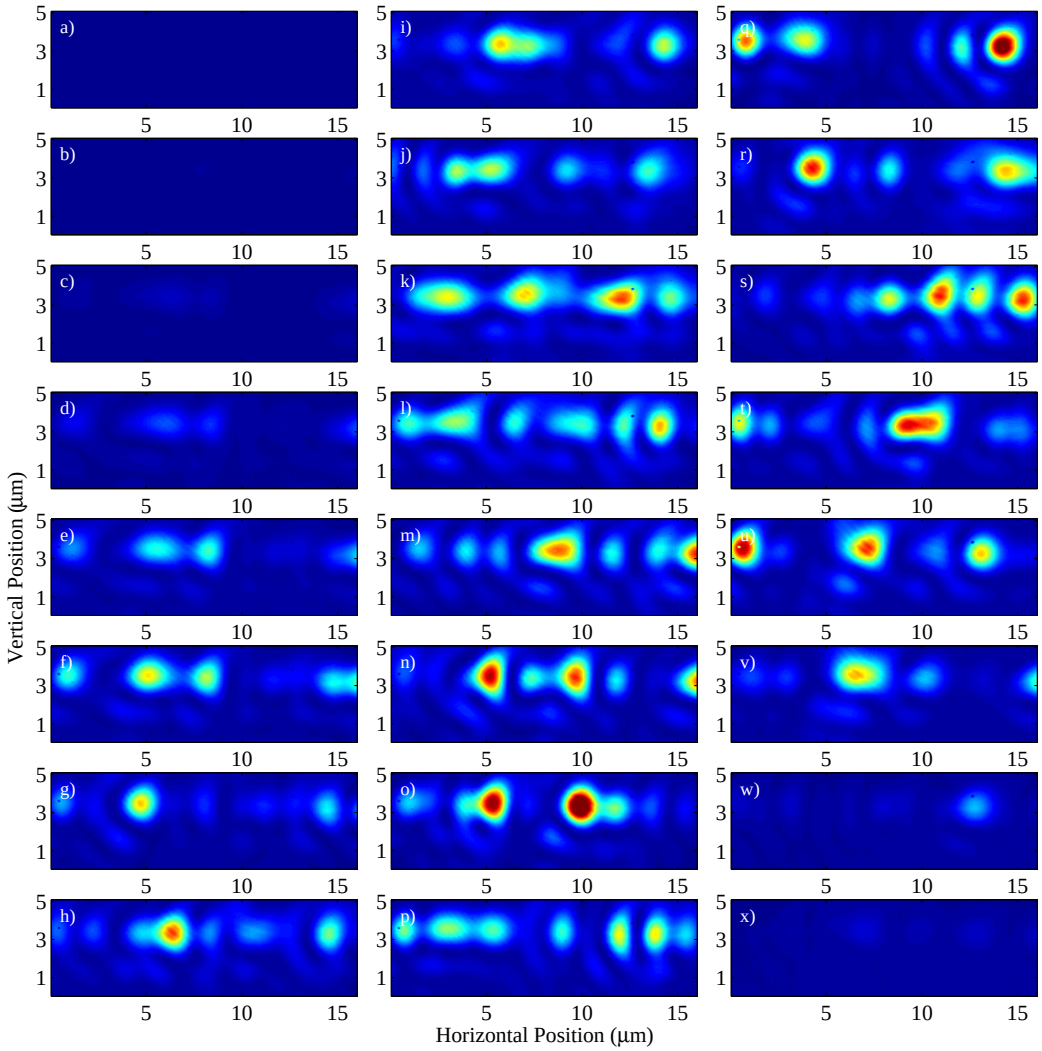

Figure 2.16: Images of the output from a fifteen wire array consisting of 420 nm×220 nm wires with wall-to-wall separations of 600 nm. The images were recorded using the same IR CCD camera used previously, whilst the input coupling lens was translated across the array from left to right in ∼600 nm steps. The image scales are approximate, based on the ratio of the image distance to focal length of the output lens, with each image pixel corresponding to ∼ 50 nm of object size. Note that on this scale, the waveguides would be just 4 pixels high and approximately 8 wide. Images should be viewed in alphabetical order from (a) to (x), with each image corresponding to the input lens be translated an additional 600 nm across the array input. Red and blue indicate high and low light intensities respectively.

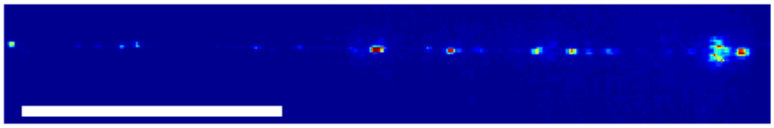

Figure 2.17: Example top view of the same array as shown in Fig. 2.16. Light is coupled into the array from the right, with strong scattering points clearly visible as the lighter blue and red points distributed randomly along the length of the array. The scale bar is 1 mm in this case with red and blue indicating high and low light intensities respectively.

above. Again, this would suggest that scattering, possibly due to side-wall roughness, or more likely a specific defect or scattering point in or around the waveguide structure, is causing a coupling of the supermodes of the array.

Using the IR CCD camera mounted above the same array, it was also possible to image the light scattered out of the array from above as the input lens was translated across the input. An example of such an image is shown in Fig. 2.17. Here light is being coupled into the array from the right, with a faint output spot visible at the far left. In addition, at random positions along the array points of strong scattering are clearly visible. The fact that these occur at specific points along the array would suggest they are arising due to specific defects, such as stitching errors or possibly dust on the arrays, as opposed to side-wall roughness, which one would assume would be more constant along the entire length of the array. It is also worth mentioning that as the input lens was moved across the array, certain scattering points disappeared with others appearing in different locations, suggesting certain defects affected specific wires within the array only.

Both the output images and images of the scattered light from above would therefore suggest the presence of considerable scattering points along the length of the array. This in turn could lead to a coupling between the individual supermodes of an array and the multiple fringes observed in the interferograms discussed earlier in the chapter.

2.7 Conclusions

The work in this chapter has verified experimentally the presence of coupling-induced dispersion in strongly coupled SOI photonic wire arrays, through measurements of n_g for the symmetric and antisymmetric supermodes of two coupled wires. Experimental results show good agreement with the modelled data, demonstrating that the region of anomalous dispersion is restricted for the symmetric TE supermode and extended for the antisymmetric TE supermode, relative to a single wire. This has strong implications for the observation of nonlinear optical effects that require anomalous dispersion. For example, solitons and modulation instability [51], should be observable in arrays at wavelengths where the effects would not be supported in a single wire, provided that the antisymmetric mode can be excited. Experimentally, efficient coupling into the antisymmetric supermode can be achieved by controlling the tilt of the input beam, thereby introducing a phase shift between the light in each wire. There is also strong experimental and modelled evidence to suggest the cut-off of the antisymmetric TE supermode, while the symmetric TE supermode continues to propagate as a slot mode. The presence of an anti-crossing between the antisymmetric TE and symmetric TM supermodes, due to asymmetric supermode expansion, is also predicted. These results were published in Optics Letters [89]. The work carried out in this chapter also led on to nonlinear measurements of modulation instability in a SOI directional coupler, carried out by co-workers at the University of Bath [90]. A short investigation into the causes of the multiple fringes observed in the interferograms for large differences in n_g was also carried out, by imaging the output and top scattered light from a larger array of wires. The resulting images suggest the presence of scattering due to a combination of defects or fabrication errors, resulting in the scattering of light between the symmetric and antisymmetric supermodes.

Chapter 3

Linear Properties of 1D Photonic Crystal Microcavities in Silicon

In recent years optical microcavities ([37] and references therein) have been the subject of considerable research due to their ability to store light for extended periods in increasingly small volumes, thanks to their large Q-factors and small cavity mode volumes, V. The increased confinement leads to greatly enhanced light-matter interactions, making it possible for optically active materials placed within such a cavity to become coupled to the electromagnetic mode of the cavity. Optical microcavities thus provide an opportunity to observe the effects of quantum electrodynamics (QED), including the possible enhancement or suppression of spontaneous emission in the case of weak-coupling [91] and vacuum Rabi oscillations in the strong-coupling regime. Soliton effects [92] and chaos can also be observed in optical microcavities [93]. Their wavelength selectivity and small size, coupled with the fact they are often made from semiconductor materials such as Si, means they are also of fundamental importance in integrated optics. Optical filtering [94], modulation [35], switching [95], logic and memory [96] have all been successfully demonstrated using microcavities. Novel laser sources, where the laser cavity takes the form of an optical microcavity, have also been developed allowing for low threshold pump powers [97] and increased functionality. The continued quest for higher Q-factors and diffraction limited volumes has led to a myriad of cavity designs and geometries, from the simple ring cavity to those making use of whispering-gallery modes (WGM's) and the photonic band-gap (PBG) effect. In this chapter the linear properties of one type of microcavity, the 1D photonic crystal (PhC) microcavity, are investigated.

3.1 Review of Optical Microcavities

As stated in Chapter 1, the ratio of circulating intensity to input power is proportional to Q/V, where Q is related to the cavity storage time, τ. This makes the ratio Q/V an important figure of merit for the devices described below. The various types and designs of optical micrcavity all have relative advantages and disadvantages, both in terms of fabrication and in their ability to achieve high Q-factors and small volumes. In this section a brief overview of some of the most common microcavity designs is given, although it is in no way intended to be a complete review.

Perhaps the simplest example of a generic optical microcavity is the so-called microring resonator[1] [98], consisting of a single waveguide looped around on itself to from a ring, as shown in Fig. 3.1 (a). Resonances will then occur when the optical path length of the loop is an equal number of whole wavelengths. In the case where the sides of the ring are elongated with straight sections the term racetrack resonator is often used. In the standard configuration, coupling into and out of the ring is achieved through the use of a single input, or bus, waveguide, evanescently coupled to the ring. The strength of this coupling is an important consideration when designing such microrings [99]. Due to the large refractive index of Si and other semiconductors, such as AlGaAs, in the spectral region around 1500 nm, on-chip microrings can be fabricated from strip waveguides with bend radii as small as $\sim 3\,\mu$m without the detrimental effects of excessive bend-loss. Ring microcavities with bend radii of $5\,\mu$m and Q-factors of the order of 10^4 are common, with bend radii as low as $1.5\,\mu$m also having been demonstrated [100]. Even in this case however V was estimated at $1\,\mu\text{m}^3$, which is still some way off the diffraction limit of $(\lambda/2n)^3$ (which for a wavelength of 1550 nm and a refractive index of 3.48 equates to approximately $0.01\,\mu\text{m}^3$). The cavity Q-factor in this instance was also just 9,000 due to increased bend-loss. Improvements in design and fabrication have, however, led to significant increases in *intrinsic* Q-factors for microring resonators, with values of 200,000 - 300,000 [101] and 2.2×10^7 [102] demonstrated for radii of $5\,\mu$m and 12.5 mm respectively. It is important to note however, that the intrinsic Q-factor refers to the Q-factor of an *isolated* cavity i.e. it characterises the rate of energy dissipation from the cavity in the absence of coupling to a bus waveguide. Of course, a way of coupling light into and out of the microring resonator is needed in order for it to be useful, and so some form of bus waveguide is nearly always present. This additional coupling mechanism ensures the total Q-factor is always lower than than the intrinsic Q-factor. Often microring resonators are designed so that the rate of

[1]The terms resonator and cavity are often used interchangeably.

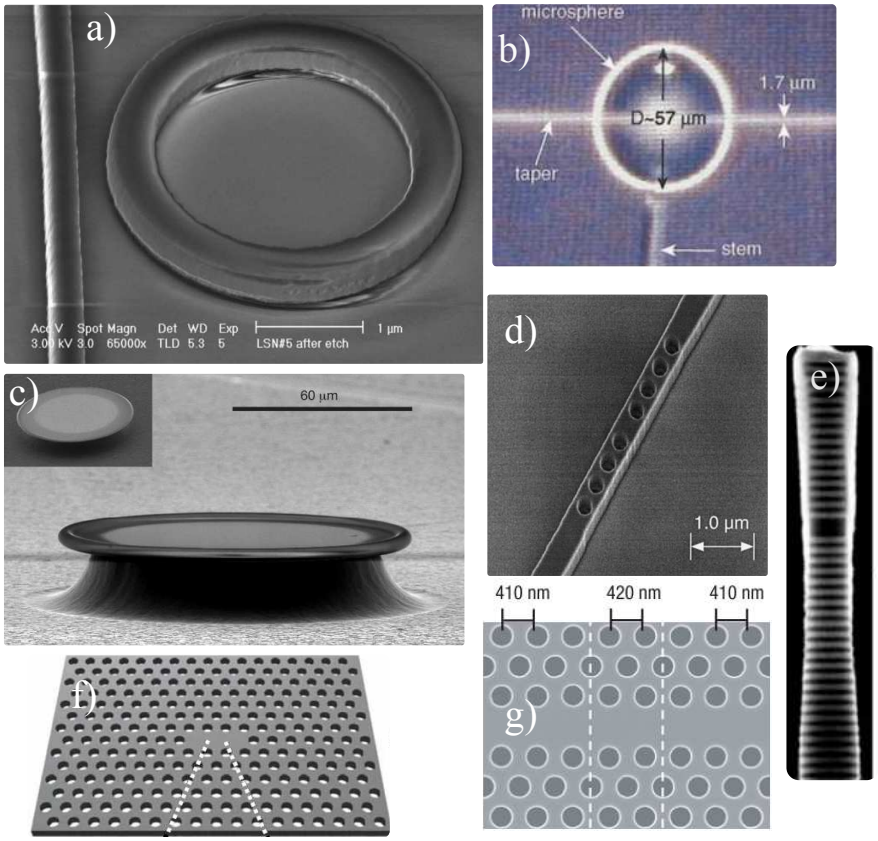

Figure 3.1: Examples of different optical microcavities. a) A Si microring resonator [100]. b) A tapered-fibre coupled silica microsphere [106]. c) A silica on Si microtoroid [107]. d) An early 1D PhC microcavity in Si [108]. e) A GaAs/GaAlAs micro-pilllar [109]. f) A schematic of a 2D PhC microcavity. g) A 2D PhC heterostructure cavity [110].

coupling into the ring from the bus waveguide is equal to the rate of energy lost from it by scattering and absorption losses. This condition, known as critical-coupling [99], provides the highest possible cavity Q-factor and also the largest contrast between on and off resonance transmission. In this case the Q-factor of the complete device is half that of the intrinsic Q-factor. The above references help to illustrate one of the main drawbacks with using microring resonators; the difficulty in simultaneously achieving ultra-high Q-factors and close to diffraction limited volumes, thereby ensuring a large Q/V ratio and small device footprint. Despite this limitation, microring resonators have proved popular, with optical modulation [35], switching, filtering and frequency generation [103] achieved using microrings. It is also possible to add an additional waveguide to create an add-drop configuration [104], or to include a series of multiple coupled or cascaded microrings to increase functionality [105].

Other types of microcavity, including microdisks [111], microtoroids [112] and microspheres [113] like those shown in Fig. 3.1 (b) and (c), make use of optical whispering-gallery modes [114], named after their acoustic analogues first proposed by Lord Rayleigh in relation to St Paul's Cathedral, London. Light is guided around the perimeter of these dielectric structures through 'continuous total-internal-reflection', meaning their Q-factors are strongly influenced by surface roughness and defects at the air-dielectric boundary. Microspheres formed from droplets of molten silica possess almost atomically smooth surfaces, due to the effects of surface tension, and have been shown to possess Q-factors of 8×10^9 [113] at wavelengths around 700 nm. Their high Q-factors make microspheres highly suited to cavity QED as well as for the fabrication of low threshold lasers. Microtoroids have been shown to possess similarly high Q-factors, but with the additional benefits of more easily controllable and chip based fabrication [107], making them far more useful for integrated circuit applications. However, their increased dimensions result in volumes of tens of cubic microns [112], much larger than the diffraction limited mode volume. Coupling to both types of microcavity is often achieved through the use of a tapered optical fibre, where the the modes of each are phase-matched to allow efficient coupling [115].

Another important type of optical microcavity is the micropillar [116], an example of which can be seen in Fig. 3.1 (e). Typical diameters are of the order of a few microns, with optical confinement achieved through index guiding and distributed Bragg mirrors (DBMs) in the transverse and longitudinal (parallel to the pillar axis) directions respectively. These consist of alternating layers of, typically two, high and low refractive index materials. The thickness of each layer is chosen so that, for a particular wavelength, the multiple Fresnel reflections from each interface interfere destructively in the forward direction, so that any incident light is reflected by the mirror. Often the layers are chosen to be $\lambda/4$ thick to provide the highest possible reflectivity, whilst the range of wavelengths reflected, known as the stop-band, can be increased by using layers with a larger index contrast. High reflectivities can be achieved with mirrors of this type, particularly when multiple layers are used, resulting in high Q-factors exceeding 150,000 [109]. The cavities themselves are formed by introducing a single layer that is slightly thicker than the rest, often $\sim \lambda$ thick, resulting in cavities with small volumes of around $1\,\mu\text{m}^3$. Their large Q/V ratios make these cavities useful for QED [91] experiments and in particular applications in which good light extraction is necessary, such as the construction of a microlaser [117]. Light emitted by objects such as quantum dots inside the cavity escapes efficiently in the directions parallel to the micropillar in single-lobed, Gaussian-like patterns.

2D PhC slab microcavities make use of both the PBG effect and index guiding for in-plane and out-of-plane confinement respectively. As can be seen from the example cavities shown in Figs 3.1 (f) and (g), the semiconductor slab has a periodic array of air holes etched into it. Light in the slab will experience a periodic modulation of refractive index as it propagates through the high index semiconductor and low index air holes, giving rise to multiple coherent reflections. For a certain range of wavelengths or photon energies, known as the photonic band-gap, these coherent reflections result in a forbidden band in which light cannot propagate inside the structure [118]. This is analogous to the electronic band-gaps observed in solid-state physics, where electrons propagating through a crystal experience a periodic potential. The term photonic crystal is thus used to describe periodic dielectric structures, which can be seen as the optical analogue of electronic crystals [119]. Note that this behaviour is similar to the DBMs mentioned above, which can be viewed as a type of 1D PhC, except that in this case confinement is achieved in two dimensions, as opposed to just one. As with DBMs, in order for a PBG to exist, the high and low index features must be comparable in size to the wavelength of light being confined, which means dimensions of just hundreds of nanometres for light at 1550 nm in Si. The arrangement of the high and low index regions, often in the shape of a triangular/hexagonal lattice, their spacing (pitch), their relative amounts (filling-fraction) and the index contrast between them all effect the position and width of the PBG. Microcavities with close to diffraction limited volumes of around $(\lambda/2n)^3$ can be fabricated straightforwardly by introducing defects into the PhC slab [120]. These provide locations at which light within the PBG can propagate and therefore become trapped, just as defects in an electronic lattice can trap electrons. Defects in this case are anything that breaks the periodicity of the PhC and can include changes to the pitch (see Fig. 3.1 (g)), the size of air holes or even their complete removal from the lattice. A common example of a 2D-PhC slab microcavity is the so-called 'L3 cavity', achieved by removing 3 holes, as can be seen in Fig. 3.1 (f). Bus waveguides for input and output coupling can be straightforwardly incorporated on chip by removing an entire row of holes creating a 'line-defect' that acts as a waveguide for light within the PBG [121]. Initially Q-factors for hole-defect type cavities were limited to just a few thousand [122], before enhancements were achieved by a careful rearrangement, or tuning, of the the holes in the immediate vicinity of the defect(s) [123, 124]. This led to a reduction in cavity losses due to vertically scattered light, resulting in Q-factors of around 10^5 [125]. Further increases in Q-factor have been achieved with the fabrication of 2D PhC heterostructure cavities. These consist of a line-defect waveguide where the hole spacing (or lattice constant) of the surrounding PhC is changed at points along the waveguide [126], providing confinement in the propagation direction through the

mode-gap effect [127]. Changing the lattice constant of the surrounding 2D PhC slab only in the direction of propagation shifts the transmission band of the waveguide in that region, relative to the others, so that certain wavelengths can propagate and become localised in the central region. An example of this type of microcavity can be seen in Fig. 3.1 (g), where the dashed white lines separate the regions of differing lattice constant. Through use of heterostructures, or even double-heterostructures, Q-factors of up to 800,000 have been demonstrated [110] in cavities with volumes as low as $1.2(\lambda/2n)^3$. These types of microcavity thus provide large Q/V ratios, making them highly useful for all manner of experiments and devices [128].

Having given a brief outline of the various types of optical microcavity, the following section will be used to give a more in-depth view of the type of microcavity that is the subject of this chapter, namely the 1D PhC microcavity. One of the earliest examples of such a cavity is shown in Fig. 3.1 (d).

3.2 1D Photonic Crystal Microcavities in Silicon

Like their 2D counterparts, 1D PhC microcavities make use of both index-guiding and the PBG effect to achieve complete confinement of light in all three dimensions. As can be seen from Fig. 3.1 (d), the basic configuration is that of a single strip-waveguide into which a periodic array of holes has been etched [108]. The waveguide, often fabricated from Si as outlined in Chapter 1, typically supports a single guided-mode (for each quasi-polarisation) and provides confinement in the transverse directions. The etching of a periodic array of holes into the waveguide down to the substrate creates the 1D PhC structure, which exhibits a PBG over the desired range of wavelengths through careful design of the centre-to-centre spacing, a, and diameter of the holes, d. The cause of the PBG, namely the destructive interference arising from the coherent reflections at the air-dielectric interfaces, is identical to that for the DBMs and 2D PhC structures. An alternative, and equally valid interpretation, is that the periodicity in the longitudinal direction of the waveguide, caused by the introduction of the holes, leads to a periodicity in β. For a waveguide with holes etched along its entire length (or any other type of periodic modulation in dielectric constant), the values β can take are now restricted to the range $-\pi/a \leq \beta \leq \pi/a$, which defines an effective Brillouin Zone similar to that for electrons in solids. The result is a splitting of the β versus ω plot for a uniform strip waveguide, so that two modes are now supported with a frequency gap between them for which no modes are supported; a PBG [129]. As stated previously

the spectral width of the gap, which for Si and air as considered here is around 400 nm, is dependent on the index contrast of the structure. The PBG exhibited by this type of structure is however incomplete; it exists only for the TE polarisation [130]. As will be demonstrated below, TM polarised light is unaffected by the PhC mirrors and so for all of the following work only TE polarised light, with the principal electric field component parallel to the silica substrate, is used.

In a similar manner to 2D PhC structures, omitting a single hole creates a defect in which light within the PBG can be localised in an extremely small volume [129]. The physical cavity length, defined as the distance between the inner edges of the holes on either side of the defect as shown in Fig. 3.2, can be as small as $\sim$ 500 nm for microcavities operating in the region around 1550 nm. For the device shown in Fig. 3.1 (d), the estimated cavity volume was just 0.055 μm^3, or $\sim 5(\lambda/2n)^3$, however the Q-factor was only 265.

The holes forming the 1D PhC structure to either side of the defect can be viewed as 1D PhC mirrors, exhibiting properties similar to the DBMs used in the fabrication of micro-pillar cavities. Light is confined within the defect region and decays exponentially into the PhC mirrors, which, due to their finite size, allow light to be coupled out of the cavity by tunnelling. In contrast to many of the other types of microcavity discussed above the cavity is formed directly from, and is thus 'in-line' with, the input waveguide, meaning the maximum transmission is achieved on-resonance, as opposed to off-resonance for microring resonators and other side-coupled microcavities. This also eliminates the need for the careful positioning of a bus waveguide, making coupling into and out of the cavities relatively straight forward.

3.2.1 A Fabry-Pérot Description

The resonant properties of this type of microcavity have been shown to be amenable to a Fabry-Pérot type description [131], like that described in Chapter 1. The cavity mode can be assumed to be a standing-wave pattern, formed from the fundamental mode of the unpatterned strip waveguide within the defect being reflected back and forth between the PhC mirrors. A modal reflectivity, $r = |r|e^{i\phi_r}$, can be used to describe how well the mirrors reflect a particular mode, with the mirror reflectivity given by $R = |r|^2$. As previously stated, under the Fabry-Pérot approach, a resonance occurs when the cavity length is equal to an integer number of half-wavelengths. This

is entirely equivalent to a phase-matching condition requiring the phase accumulated over half a cavity round-trip to equal an integer number of π. This can be written as,

$$\Phi_T(\lambda_{res}) = k_0(\lambda_{res})n_{eff}(\lambda_{res})L + \phi_r(\lambda_{res}) = m\pi \tag{3.1}$$

where again L is the physical cavity length, $\phi_r(\lambda_{res})$ is the phase shift due to reflection by the PhC mirrors and m is an integer that denotes the mode order. Recalling the definitions of Q-factor and $\mathcal{F}$ given in Chapter 1, it can be shown that $Q = \frac{m\pi\sqrt{R}}{(1-R)}$, where m is again the mode order. Under the assumption of a narrow resonance (high Q-factor), the Q-factor can then be expressed as [132],

$$Q = \frac{\pi}{1-R}\left[\frac{2Ln_g}{\lambda_{res}} - \frac{\lambda_{res}}{\pi}\left(\frac{\partial\phi_r}{\partial\lambda}\right)_{\lambda_{res}}\right], \tag{3.2}$$

where the wavelength dependence of R has been ignored and n_g is used instead of n_{eff} due to the dispersive nature of Si. A simplification can be made to the above expression by introducing the penetration length into the PhC mirrors [131],

$$L_p = \frac{-\lambda_{res}^2}{4\pi n_g}\left(\frac{\partial\phi_r}{\partial\lambda}\right)_{\lambda_{res}}. \tag{3.3}$$

Physically this represents the distance the cavity mode extends into one of the PhC mirrors, so that Equation (3.2) can be written more simply as

$$Q = \frac{k_0}{1-R}n_g(L + 2L_p). \tag{3.4}$$

The quantity $L_{eff} = (L+2L_p)$, often called the effective cavity length, can be thought of as the physical length of an equivalent cavity formed from two metallic mirrors. More specifically, the cavity mode of a 1D PhC microcavity is analogous to the reflection of the same defect-mode between metallic mirrors a distance L_{eff} apart. They are equivalent in the sense that they possess the same resonance wavelength and Q-factor given by eqs (3.1) and (3.4), assuming the metallic mirrors possess reflection coefficients independent of wavelength of the form $r_m = |r|exp[i(\phi - 2k_0n_{eff}L_p)]$.

Whilst Q-factors for this type of microcavity were initially limited to around 500 [108], Equation (3.4) highlights three key factors that affect the Q-factor, namely the effective cavity length, L_{eff}, group index, n_g, and mirror reflectivity, R. For this type of microcavity n_g is usually comparable to n_{eff} (whereas 2D PhC microcavities can support modes with e.g. $n_g = 15$), whilst L and therefore L_{eff} are fixed by the desired operating wavelength. The quantity most suitable for optimisation to achieve a high Q-factor is thus R. From the conservation of energy, R can be related to the mirror losses, $\mathcal{L}$, and mirror transmission, T, via

$$R + T + \mathcal{L} = 1, \tag{3.5}$$

since light incident on the mirrors can be either reflected, transmitted or lost via scattering to unbound modes.

A straightforward method for increasing the Q-factor is therefore to simply increase the number of holes, N, in the PhC mirror, thereby directly increasing R. Whilst this does indeed provide an increase in Q-factor, it also leads to a corresponding reduction in T, which could make the detection of transmitted light difficult, particularly for on-chip applications where low input powers are desired. More significantly, $\mathcal{L}$ is independent of N, and so for increasingly large numbers of holes ($N > 7$), the Q-factor begins to saturate and no further significant increases are observed [133]. In order to further increase R and thus achieve ultra-high Q-factors it is therefore necessary to reduce $\mathcal{L}$.

Considerable work has been done in this area, with the source of the mirror losses found to be out-of-plane radiation losses [134] originating from mode profile mismatches between modes of the unpatterned waveguide and the PhC mirrors [135]. (This also explains why $\mathcal{L}$ is independent of N, as the mismatch is present irrespective of the number of holes in the mirror.) The mode of the defect is that of the unpatterned waveguide, whilst the mode of the periodic mirrors is an evanescently decaying photonic Bloch mode for wavelengths within the PBG. At the abrupt interfaces between the PhC mirrors and the uniform waveguide sections there will inevitably be losses due to the incomplete overlap of the modes. The losses are similar in nature to those experienced when the end faces of two dissimilar optical fibres are brought into direct contact in a process known as butt-coupling. In this case the coupling loss between the fibres is again caused by the mismatch of the modes. The key to reducing $\mathcal{L}$ is thus to ensure a more gradual, adiabatic transition from the PhC mirrors to the unpatterned

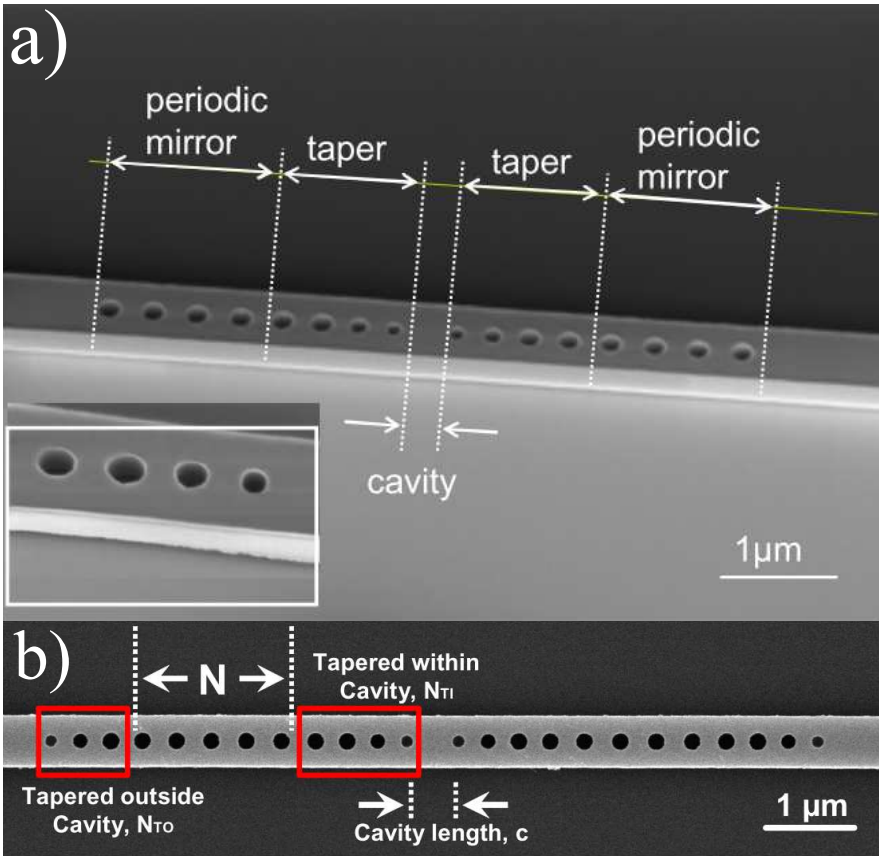

Figure 3.2: a) An example of a 1D PhC microcavity with tapers on the insides of the mirrors only. The physical cavity length, periodic mirror and tapered sections are identified, with the inset showing a close-up of one of the tapered sections [136]. b)An example of an ultra-high Q/V 1D PhC microcavity, achieved through the use of tapered sections on both the inside and outside of the periodic mirror sections [44].

waveguide sections. This type of Bloch mode engineering allows a gradual conversion of the photonic Bloch modes of the mirrors into the cavity mode and back again, reducing the modal mismatch and consequently out-of-plane scattering losses. The principle is similar to approaches used in fibre-optics, in which the diameter of a fibre can be changed by gradually tapering it over a length scale longer than any diffractive effects may occur, allowing a transition with minimal losses.

In the case of 1D PhC microcavities, the gradual transition was achieved initially through the use of tapered sections on the inner sides of the mirrors [136], closest to the cavity defect, as can be seen in Fig. 3.2 (a). These tapered regions consist of a number of holes of increasing (decreasing) diameter, and non-uniform spacing. The use of such

tapers, with the hole positions and sizes optimised through computational methods, led to dramatic increases in Q-factor. For example, the microcavity in Fig. 3.2 (a) has an experimentally measured Q-factor of 58,000, combined with an ultra-small V_{eff} of just $0.6(\lambda/n)^3$. Further improvements have been made by incorporating additional tapered sections on the outside of the 1D PhC mirrors, like those shown in Fig. 3.2 (b), leading to a cavity with a Q-factor of 149,000 [44]. More recently it has been suggested that cavities with a physical length of 0 nm could provide even higher values of Q-factor [137]. In this case the cavity consists of just a single 'modulated Bragg mirror' in which the cavity mode is located, such that their is no physical defect and hence the cavity can be thought of as having a 0 nm physical length. The possibility of achieving such high Q-factors in conjunction with their inherently small mode volumes ensures 1D PhC microcavities can possess extremely large Q/V ratios, and combined with their chip-based fabrication makes them highly suited to on-chip applications.

3.2.2 Cavity Mode Volume

The ratio Q/V has emerged as a key figure of merit for optical microcavities, however until now no mention has been made of how V is defined. The issues faced are similar to those encountered when estimating A_{eff} for a waveguide mode (see Chapter 1). Due to the often complicated cavity mode profiles, the fact that the modes decay exponentially away from the confining structure and can often penetrate some way into the PhC cladding or mirrors, it is not sufficient to simply calculate the physical volume of the cavity region. Thus an effective cavity volume, V_{eff}, is used [112],

$$V_{eff} = \frac{\int_V \epsilon(r)|\vec{E}(r)|^2 dV}{\max(\epsilon(r)|\vec{E}(r)|^2}. \tag{3.6}$$

where $\epsilon(r)$ is the permittivity of free space, $\vec{E}(r)$ is the electric field of the cavity mode and the integral is performed over all space. Physically, this definition is related to the energy density of the optical mode and represents the equivalent volume the mode would occupy if its energy were distributed evenly in space at the peak value of energy density. A problem arises, however, due to the finite Q-factors of all microcavities, which leads to propagating fields outside the cavity region, causing the integral to diverge. For relatively high-Q-factor microcavities the introduction of a quantization volume over which the integral in Eq. (3.6) is performed can be introduced in order to prevent this [138].

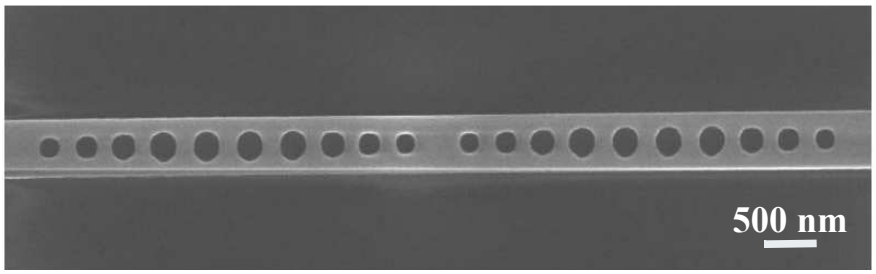

Figure 3.3: Example SEM of a cavity from chip A with $N = 4$ and 3-hole tapers on the inside and outside of the cavities.

3.3 Linear Characterisation of 1D PhC Microcavities

Two chips were provided by co-workers from the University of Glasgow, chips A and B, each with a large number of different device geometries, varying the cavity length and the number and diameters of the holes in the PhC mirrors. The heights and widths of the wires into which the holes were etched remained constant, at 220 nm and 500 nm respectively, leading to structures similar to those shown in Fig. 3.2 (b). With three repetitions of each geometry there were a total of 216 individual microcavities on each chip, along with 10 unpatterned, reference waveguides for comparison. An example SEM of a microcavity from bar A is shown in Fig. 3.3. Such a large number of devices was necessary in order to ensure both a high Q-factor and resonant wavelength within the tuning range of the laser used for the experiments, since the resonant properties of the microcavities are very sensitive to fabrication errors.

3.3.1 Experimental Setup

Initial characterisation of the devices was undertaken using the experimental set-up shown in Fig. 3.4. The light source used was a fibre-coupled, continuous-wave (CW) laser (*CoBrite*; DX1), step-tunable from 1528 nm to 1566 nm and providing output powers from 2.5 mW to 30 mW. The output was coupled into a polarisation maintaining (PM) fibre patch-cord (*Thorlabs*; P1-1550PM-FC-1) in order to preserve the linear polarisation of the laser light, before being coupled into each device. In addition, a variable neutral density (ND) filter provided additional power control, whilst a pair of $\lambda/2$-plates and a polarising beam splitter (PBS) were used to rotate the polarisation of the input light for coupling purposes and remove any unwanted polarisations respectively. After the chip a second PBS was included to remove any substrate guided light

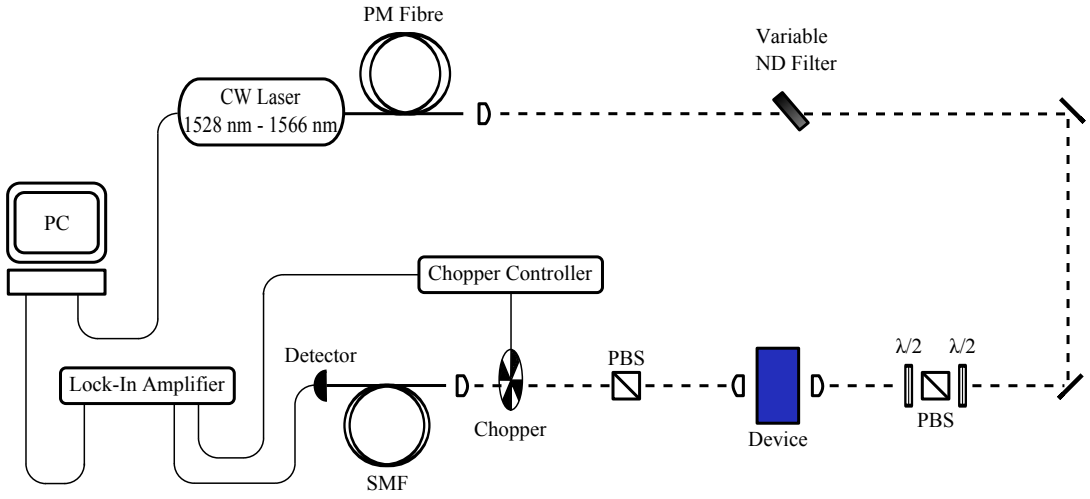

Figure 3.4: Initial experimental set-up used for micrcocavity device characterisation (PBS = polarising beam splitter; ND = neutral density; $\lambda/2$ = half-wave plate; PM = polarisation maintaining fibre; SMF = single mode fibre).

with the wrong polarisation that may have interfered with the measurements. Detection was performed in an identical manner to that used in Chapter 2 when looking at arrays of coupled wires. The output was collected using a short SMF-28 patch-cord and directed onto the same photodiode (*New Focus* Femtowatt Photoreceiver; Model 2153), used in conjunction with the same lock-in amplifier (*Stanford Research Systems*; SR830 DSP) again referenced to an optical chopper positioned after the PBS. Both the laser and data acquisition were controlled using a PC via a custom written LabVIEW programme.

Unlike with the arrays, the microcavity devices contained polymer coated tapers at the input and output in order to improve coupling efficiencies [139]. As a result lower magnification, 40× singlet lenses (NA = 0.55, *New Focus*; 5722-C) could be used for input and output coupling, instead of the 60× lenses used previously. Reproducible coupling was once again achieved using the IR camera, first mounted above the chip to image top scattered light and ensure the correct device was selected. The camera could then be positioned immediately after the output coupling lens and PBS in order to image the output from a given device. Coupling could then be optimised through a combination of maximising the output viewed on the IR camera and the transmitted signal as measured by the lock-in amplifier.

Prior to testing any of the microcavity devices an estimate of the input and output coupling losses was made by measuring the transmission of the unpatterned, reference

wires included on the chip. The insertion losses (IL) of five wires were measured by coupling into each in turn, as outlined above, and then measuring the input power, P_{in}, immediately before the input coupling lens and the output power, P_{out}, after the output coupling lens and PBS. The power meter used (*Newport*; 1830-C) was capable of measuring powers as low as just a few nWs. The insertion loss for each reference wire could then be calculated using,

$$IL = -10 \log_{10} \frac{P_{out}}{P_{in}}. \tag{3.7}$$

The average IL of the five reference wires was found to be 11±1 dB. This is a considerable improvement over the approximately 25 dB IL of the array used in Chapter 2, measured in the same way, and shows the effectiveness of the polymer coated tapers. This total IL calculated above is a combination of the input coupling, propagation and output coupling losses respectively. Prior to shipment, the propagation losses of these wires were measured by co-workers at the University of Glasgow using a Fabry-Pérot resonance technique [140] and were found to be ≈ 2.5 dBcm^{-1}. The loss due to propagation along the length of the 5 mm wires is therefore ≈ 1.75 dB, so that of the 11 dB IL of the wires, around 9.75 dB can be assumed to be due entirely to input and output coupling losses. In the extreme case that all of the loss is incurred at the input of the wires (meaning the output coupling loss is 0 dB) the input coupling loss would be around 9.75 dB. Of course in reality, due to the identical lenses and polymer tapers used at the input and output, it is much more likely that the remaining loss would be split almost evenly between the input and output. A reasonable estimate then is that the total IL consists of ∼4.6 dB of input coupling loss, $\sim$ 0.5 dB of propagation loss and $\sim$ 4.6 dB of output coupling loss. A value of $\sim$ 4.6 dB will therefore be assumed for the remainder of this work, which at worst is likely to underestimate rather than overestimate the input coupling loss.

One difficulty experienced when coupling into the microcavities of course is that for these types of 'in-line' cavity, the off resonance transmission is very low. Thus, if λ_{res} for a specific device is not known *a priori*, coupling can be difficult. In order to circumvent this issue it was possible to use the $\lambda/2$-plate immediately before the chip to rotate the polarisation of the incoming light to TM (or vertically polarised), as for this polarisation the PBG does not exist. For this reason the PhC mirrors will have no effect on the TM polarised light (aside from causing some increased scattering losses due to the refractive index perturbations caused by the holes), which will pass through the cavity unaffected. It was therefore possible to couple into the microcavities using

first TM polarised light of any λ and maximising the measured signal, before switching back to TE polarised and performing a wavelength scan to locate the cavity resonance. Once λ_{res} was located the on resonance transmission could then be maximised for the TE polarisation.

Example images of the top scattered light from a microcavity for a number of different input wavelengths and polarisations are shown in Fig. 3.5. As mentioned previously the images are obtained using an IR camera mounted directly above the chip, with Fig. 3.5 (a) showing an image of the scattered light for a TE input off resonance. The input light is incident from the bottom in the figure, with the waveguide leading to the cavity visible as the light blue vertical line. In this case it is clear no light propagates beyond the microcavity, located in the dashed white square and shown in close up in the inset. For TE polarised light with a wavelength equal to λ_{res} the cavity can now be seen to glow, with high intensity mapped as red (Fig. 3.5 (b)) as the power circulating inside is greatly enhanced on resonance, leading to a dramatic increase in scattered light. In the case of a TM input either off or on resonance (Figs 3.5 (c) and (d)), scattered light can be seen along the entire length of the wire, indicating the the TM polarised light is passing through the cavity without being affected.

3.3.2 Low Q-factor Cavities

The first set of devices tested were those on chip A. The resonance positions and Q-factors of the microcavities were determined by performing low power transmission measurements, obtained by stepping the input frequency in 5 GHz steps. A P_{in} of 10 µW was used to ensure an in-waveguide power of just microwatts after input-coupling losses, so that any nonlinear effects were negligible. Unfortunately, a large number of devices were found to have resonant wavelengths outside of the tuning range of the laser, whilst those resonances that were accessible had Q-factors ranging from just 1,000 - 2,500. These were far below the Q-factor values expected and the cavities on chip A proved unusable for the nonlinear experiments described in Chapter 4.

An example of a typical transmission spectrum for a microcavity from Chip A is shown in Fig. 3.6. The microcavity in this case has λ_{res} = 1536.3 nm and a Q-factor of just 1,500. The resonance itself is also strongly modulated with multiple peaks and is representative of the micrcavity resonances that could be measured on chip A. Figure 3.7 shows the the transmission spectrum of another microcavity, again exhibiting a broad, strongly modulated resonance. In this case there is also pronounced off reso-

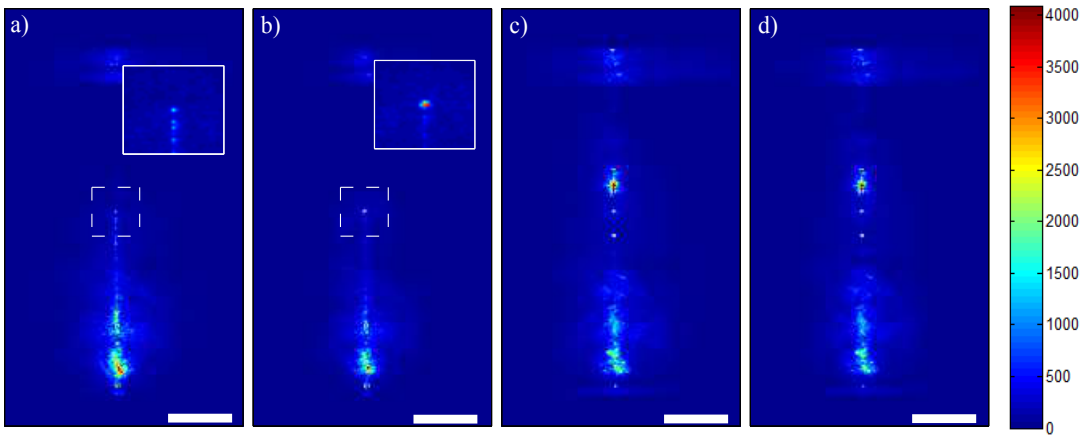

Figure 3.5: Top down view of the scattered light from a microcavity, recorded with the IR camera mounted on a microscope and positioned directly above the chip. The input light is incident from the bottom in each image, with the device visible as the lighter blue vertical line. a) The incident light is TE polarised with $\lambda \neq \lambda_{res}$, resulting in low transmission and hence no scattered light visible beyond the cavity. The inset is an expended view of the region around the cavity enclosed in the dashed square. b) As with a), but $\lambda = \lambda_{res}$ and the incident light is on resonance. The cavity is visible as the bright red dot in the inset, as due to the field enhancement experienced on resonance there is more scattered light and the cavity 'glows' brightly. c) The input light is TM polarised with $\lambda \neq \lambda_{res}$. Scattered light is visible along the entire length of the device, indicating the mirrors are no longer reflecting and thus no PBG exists for the TM polarisation. d) As with c), but $\lambda = \lambda_{res}$, again demonstrating the lack of PBG for TM polarised light as no field enhancement is observed in the cavity. The scale bar is each case is 1 mm.

nance transmission, with a series of small peaks in transmission superimposed on the cavity resonance. These effects may be due to reflections from the waveguide end faces, which can be large due to the large index contrast between air and Si, particularly if the end faces are well cleaved. This can effectively lead to the formation of a second cavity between the waveguide end faces, whose transmission spectrum would be superimposed over the 1D PhC microcavity transmission spectrum. As well as improving coupling efficiencies however, the polymer tapers at the input and output of the devices are also designed to reduce the strength of the reflections from the end faces, making this explanation less likely. There also seems to be an additional periodic modulation of the transmission spectra at a higher frequency (shorter wavelength spacing), as is clear from the inset of Fig. 3.7.

By assuming each set of resonances can be associated with an effective Fabry-Pérot cavity formed somewhere within the device, it is possible to measure the spacings (FSR) of each of the sets of resonance-like features and obtain an estimate of the lengths of the additional cavities being formed. The spacings are found to be ∼1.1 nm and ∼0.14 nm respectively, so that one can use the formula for FSR given in Chapter 1 to calculate the lengths of the effective cavities associated with each. To be truly accurate, n should be replaced by n_g due to the dispersive nature of the Si wires, however as $n_g \sim n$ in these types of waveguide, $n = 3.45$ for bulk Si can be used to obtain a suitable estimate. The lengths associated with each are thus $L_1 = 0.25\,\mu\text{m}$ (for FSR = 1.4 nm) and $L_2 = 2.5\,\mu\text{m}$ (for FSR = 0.14 nm). Neither of these lengths can be associated with any specific device features and so the origin of the resonances is unclear. These sorts of double Fabry-Pérot effects have been observed before and could potentially be associated with problems during fabrication such as stitching errors [139]. These arise because only a finite area of the Si wafer on which the devices are fabricated can be patterned by the electron beam at any one time. Consequently, the Si wafer must be moved during fabrication to pattern the entire set of devices and accuracy is required when aligning a pattern to a previously written one.

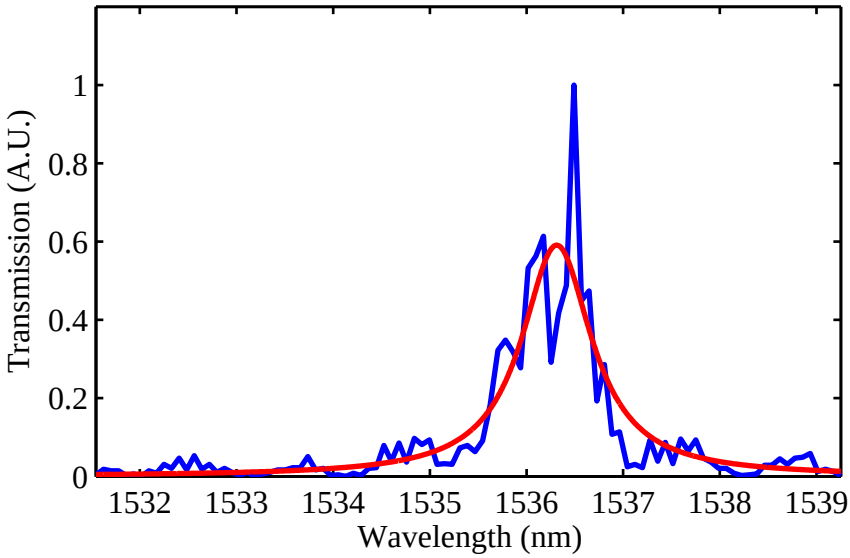

Figure 3.6: Example transmission from a cavity fabricated on chip A. The blue curve is the experimentally measured transmission spectrum and the red curve is a Lorentz fit to the data. For this particular cavity λ_{res} was found to be ∼1536.3 nm and the Q-factor was ∼1,500.

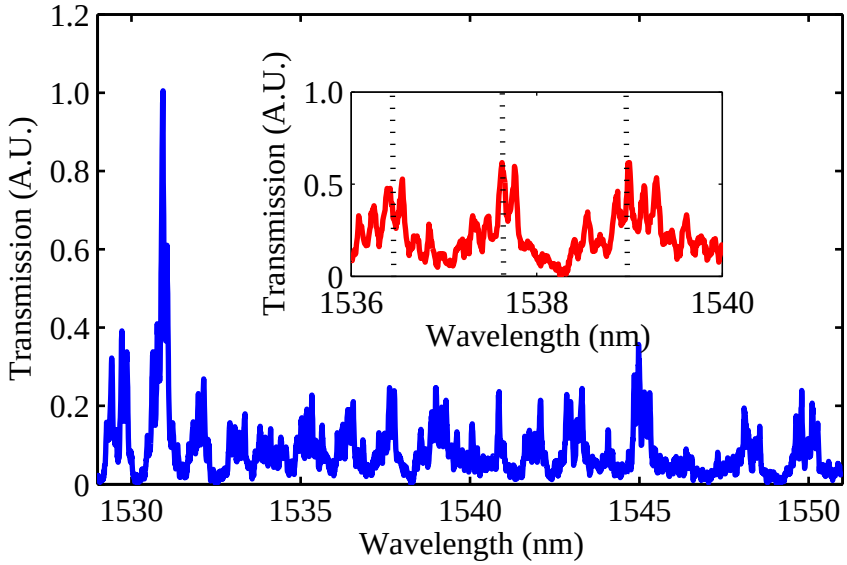

Figure 3.7: Another example transmission spectrum from a microcavity fabricated on chip A. The cavity resonance is clearly visible at $\lambda_{res} = 1530.9$ nm, but again is heavily modulated. There is also pronounced off resonance transmission showing resonance-like features. The inset shows an expanded view of the background transmission between 1536 nm and 1540 nm, with the black dashed lines indicating the locations of other resonance-like features. The spacing between these features is ∼1.1 nm. There also appears to be a further series of periodic modulations with an even smaller spacing of just ∼0.14 nm superimposed over the device response.

3.3.3 High Q-factor Cavities

As the majority of the microcavities on chip A were found to have resonances outside the tuning range of the laser, whilst those that were accessible had very low Q-factors, the devices on chip B were considered next. As with chip A, chip B contained a range of different geometries in an attempt to ensure a large Q-factor and suitable λ_{res}. In this case the periodic mirror sections consisted of N = 2-7 holes, with diameters of either 216 nm or 220 nm and separations of 420 nm. The physical cavity lengths ranged from 610 nm to 710 nm in 20 nm steps, whilst the 3-hole taper regions inside and outside the microcavity were the same for each variation. The holes had diameters of 154 nm, 176 nm and 198 nm, with centre-to-centre spacings of 361 nm, 381 nm and 406 nm respectively.

The cavities where characterised in exactly the same way as previously and whilst the resonances of a large number of devices were again found to lie outside the accessible tuning range, several were found with Q-factors of around 40,000. Whilst these are in no way the highest Q-factors obtained for this type of microcavity, with Q ~150,000 having been demonstrated [44], they were sufficient for the nonlinear experiments presented in Chapter 4 at the power levels available. The underlying physics will the be same for high or ultra-high Q-factor cavities, with the only difference being the P_{in} required to observe the effects.

An example transmission spectrum for a cavity with N = 4, a physical cavity length of 610 nm and hole diameters of 216 nm is shown in Fig. 3.8. The microcavity has λ_{res} = 1563.35 nm and $\Delta\lambda$ = 39 pm, which is a significant improvement over the cavities found on chip A. The transmission falls away smoothly to zero and remains low away from λ_{res} allowing a good fit to a Lorentzian line shape, suggesting a Q-factor of ~40,000. The additional Fabry-Pérot effects observed for the low Q-factor cavities on chip A are also absent, most likely due to better device design and fabrication. More specifically, there may be fewer stitching errors or other defects, reducing the amount of unwanted reflections that could lead to undesired effects. Additionally, some of the cavities on chip B contained a greater number of holes in the PhC mirrors forming the microcavities compared to chip A, which should increase the reflectivity of the mirrors and therefore the Q-factors of the devices.

One issue that did arise however was a drift in the position of the cavity resonances, noticed when consecutive scans were performed. An example of 3 repeat measurements

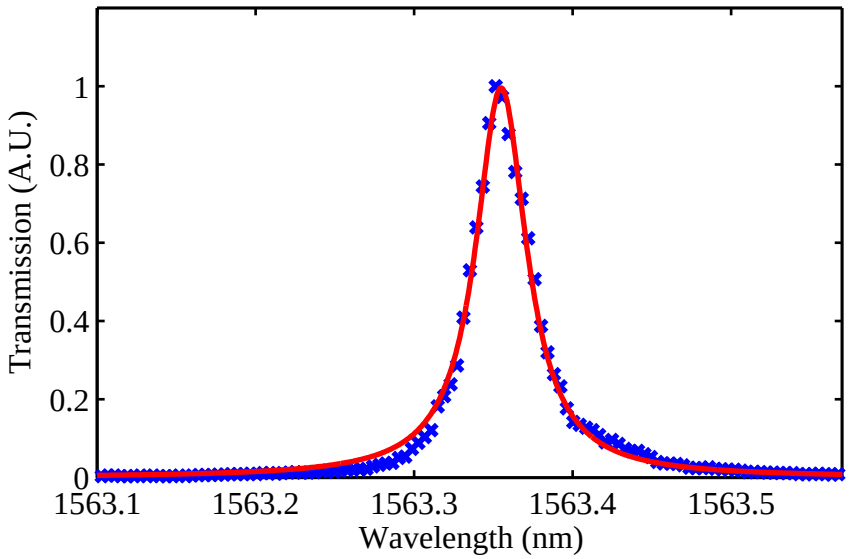

Figure 3.8: Example transmission spectrum of a high Q-factor microcavity from chip B, with $N = 4$, $L = 610$ nm and a hole diameter of 216 nm. The blue points are the experimentally measured data and the red curve is a Lorentz fit showing good agreement, indicating Q ~40,000.

performed consecutively (over a duration of $\approx$ 9 mins) for a different cavity on chip B are shown in Fig. 3.9. Whilst the shape and Q-factor of the resonance does not change appreciably, λ_{res} is seen to drift by 10 pm on this occasion. Despite this being a relatively small shift in absolute terms, given $\Delta\lambda$ is around 40 pm, a shift of 10 pm or potentially more is significant. This is particularly true if, for a given experiment, it is necessary to sit at a fixed detuning relative to λ_{res}, which would be impossible if the resonance is drifting. For this reason time was spent attempting to stabilise the resonances, prior to attempting the nonlinear measurements presented in Chapter 4.

3.3.4 Thermal Stabilisation and Tuning

It was felt that the most likely explanation of the shifting λ_{res} was that of thermal drift, given silicon's relatively large thermo-optic coefficient (TOC) [141],

$$\frac{\Delta n}{\Delta T} = +1.86 \times 10^{-4}\ \mathrm{K}^{-1}, \tag{3.8}$$

where ΔT is the change in temperature, T. Since λ_{res} depends on n a variation in

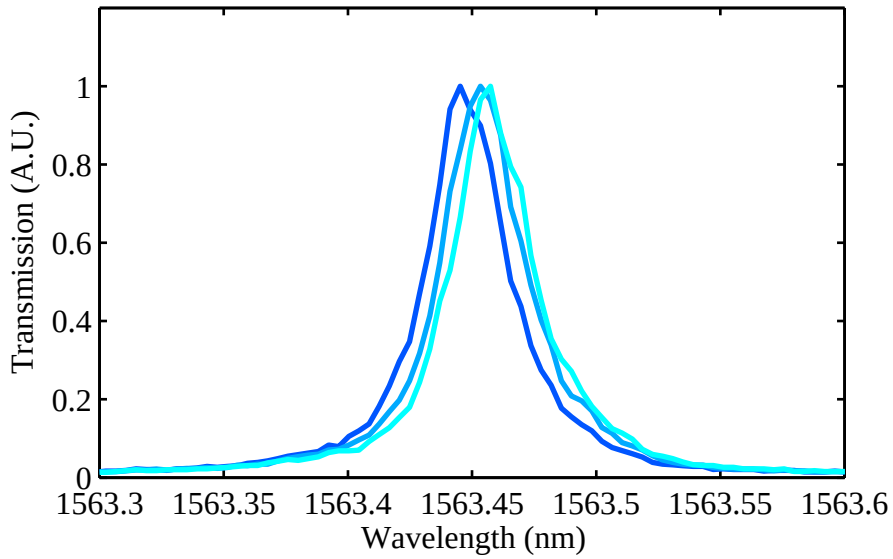

Figure 3.9: Consecutive scans of the same cavity resonance showing a drift in λ_{res} of up to 10 pm in this instance, which was assumed to be caused by small changes in environmental temperature.

T would lead to a change in n through the thermo-optic effect (TOE), resulting in a corresponding shift in λ_{res}. One may also ask what effect a change in temperature would have on the cavity length, another parameter that affects λ_{res}. The thermal expansion coefficient of Si at room temperature however is around $2{\times}10^{-6}$ K^{-1} [142], two orders of magnitude less than silicon's TOC, and it can therefore be expected the TOE will dominate. To first order then,

$$\Delta\lambda_{shift} = \Delta T \left(\frac{\lambda_{res}}{n}\right)\left(\frac{\Delta n}{\Delta T}\right) \tag{3.9}$$

where the refractive index n can once again be assumed to be that of bulk Si. Taking $n = 3.48$, $\lambda_{res} = 1563$ nm, $\Delta T = 1$ K and using Equation 3.9 suggests a possible wavelength shift $\Delta\lambda_{shift}$ of ~ 80 pm K^{-1}. A temperature change of just 0.125 K would therefore be enough to cause a $\Delta\lambda_{shift}$ of 10 pm, making temperature stabilisation necessary to prevent thermal drift.

Due to the way the sample was mounted on an aluminium block, attached to a linear translation stage, it was not possible to attach anything directly to it. For this reason it was decided instead to incorporate two Peltier devices, capable of both heating and

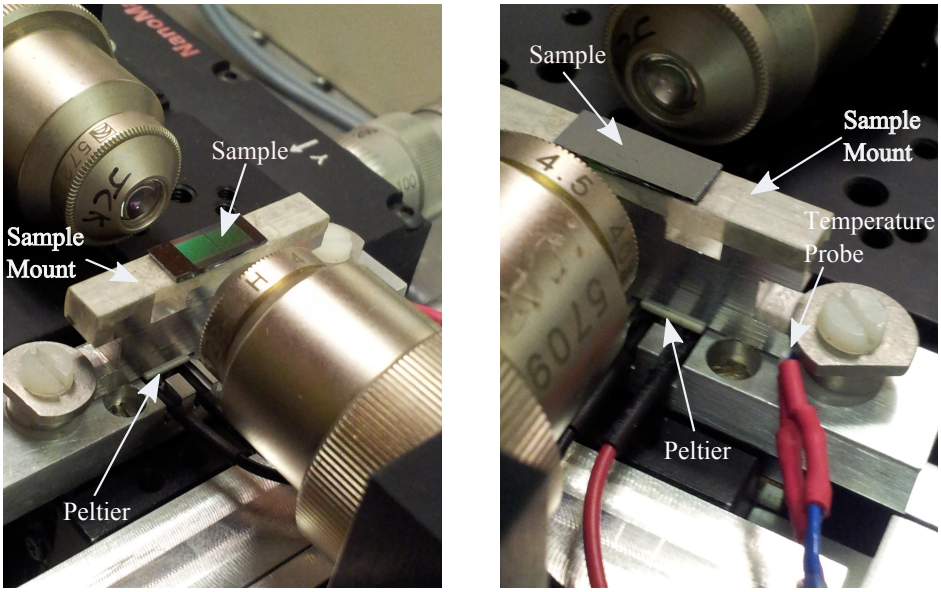

(a) (b)

Figure 3.10: Images of the chip mounted on the aluminium mount aligned between the input and output coupling lenses. a) One of the Peltier devices is visible below the sample mount. b) The second Peltier device is visible on the other side of the sample mount, along with the temperature probe that is held in place by the nylon screw.

cooling, underneath the aluminium block the sample was mounted on. A temperature probe (*RS*; PT1000 RTD) was then attached to the side of the block to monitor its temperature and provide feedback to a laser diode temperature controller (*ILX Lightwave*; LDT-5500B) that was used to control the Peltiers. The temperature of the chip was therefore controlled indirectly, by stabilising the temperature of the aluminium block on which it was mounted. In order to thermally isolate the aluminium block the Peltier devices sat slightly above the linear stage forming a pedestal on which the aluminium block could sit, separating it from the stage below. Two images of the sample mounted on the aluminium block between the input and output coupling lenses are shown in Fig. 3.10. In both images the chip, which has a width of 5 mm and a length of 1.8 mm, is visible atop the aluminium mount, between the input and output coupling lenses. Each of the Peltier devices are visible just below, attached to the red wires in Fig. 3.10 (a) and (b). In Fig. 3.10 (b) the position of the temperature probe can be seen, attached to the blue wire and held in position against the chip mount by the nylon screw.

Using this method it was possible to stabilise the temperature of the mount, and it was assumed therefore the chip also, to 0.001±0.002 K. Figure 3.12 shows the result of

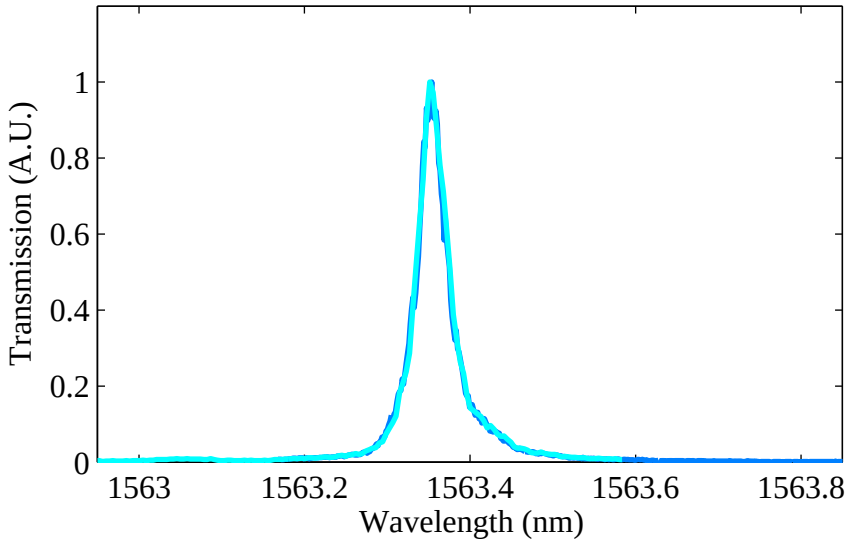

Figure 3.11: Reproducible transmission spectra obtained using the temperature stabilisation methods described in the text.

two consecutive wavelength sweeps employing the temperature stabilisation described above. The thermal drift has successfully been minimised, with λ_{res} the same for each repeat within an experimental error of ± 3 pm.

Having stabilised the temperature some additional scans were performed, keeping the wavelength constant and varying the input power as a precursor to the nonlinear measurements described in the next chapter. Performing repeated low power (10 µW) wavelength scans immediately after this showed a shift of the resonance to shorter wavelengths, sometimes of up to 20 pm. If the microcavity was being heated during the power sweeps however, one would expect λ_{res} to shift to longer wavelengths instead. To ensure the apparent shift was not caused by a slow variation of the sample temperature caused by the Peltiers, laser diode controller and probe, these were switched off and the above process repeated. In this case a shift of λ_{res} to shorter wavelengths was still observed. The possibility that the output wavelength from the laser was drifting and causing only an apparent shift in resonance position was also considered. The laser itself has a specified lifetime accuracy of ± 1.5 GHz and an output variation of $<$100 MHz in one day was measured by a co-worker using acetylene, suggesting it was sufficiently stable. A simple test to confirm this was done by varying the output power of the laser at a fixed wavelength as above, but blocking the beam so no light was incident on the microcavity. Subsequent low power wavelength scans showed no shift of the resonance, clearly indicating light needs to be incident on the microcavity to

cause the observed shift of the resonance to shorter wavelengths. The final possibility considered was that something in the air was being deposited on the microcavity, which would cause a shift in the effective mode index and therefore resonance. For increasing input powers whatever had been deposited may undergo desorption, either caused by the increase in microcavity temperature or directly through photodesorption, shifting the position of the resonance. Removing the sample from the set-up and placing it in a vacuum desiccator for 24 hours in an attempt to remove any contaminants proved successful, as the positions of the resonances had shifted even further to shorter wavelengths, suggesting something had been removed from the devices during the process. Performing power sweeps followed by low power wavelength scans also showed no sign of the shift to shorter wavelengths observed previously. For this reason, the sample was removed from the set-up and stored in the vacuum desiccator when not in use. Given the hydrophilic nature of the HSQ layer on top of the Si and the high humidities experienced in the laboratory, it is most likely that the contaminant was water being absorbed by the sample.

Following this the thermal tuning of the cavity was then investigated by setting the mount temperature to a range of different values and performing wavelength scans to locate the position of the resonance. Temperatures from 22°C to 40°C in 2°C steps were used, with the resulting transmission spectra shown in Fig. 3.12. Each spectrum is normalised so that the maximum transmission is 1 A.U. for clarity, however there was a considerable variation of 5 dB in actual maximum transmitted power across the temperature range. Care was taken to re-optimise the coupling at each temperature as the mount would undergo thermal expansion when heated, causing the optical alignment and therefore input and output coupling to change. This may account for some of the variation in maximum transmitted power, whilst it is also possible that as λ_{res} shifts with temperature the microcavity is no longer operating at the optimal wavelength, leading to increased losses. Some of the resonances in Fig. 3.12 also possess pronounced shoulders and are no longer truly Lorentzian in shape, which may be caused by additional Fabry-Pérot resonances.

From the data shown in Fig. 3.12 the resonance wavelengths were extracted allowing λ_{res} to be plotted as a function of T, shown in Fig. 3.13. Over the full 18°C temperature range λ_{res} was shifted by over 0.5 nm, whilst the experimental data points show excellent agreement with a linear fit (dashed red curve in Fig. 3.13). The linear fit has a slope of 0.0770 ± 0.0004 nm K^{-1}, which is very close to the value of ~ 0.080 nm K^{-1} estimated earlier assuming the wavelength shift is caused entirely by the TOE, and

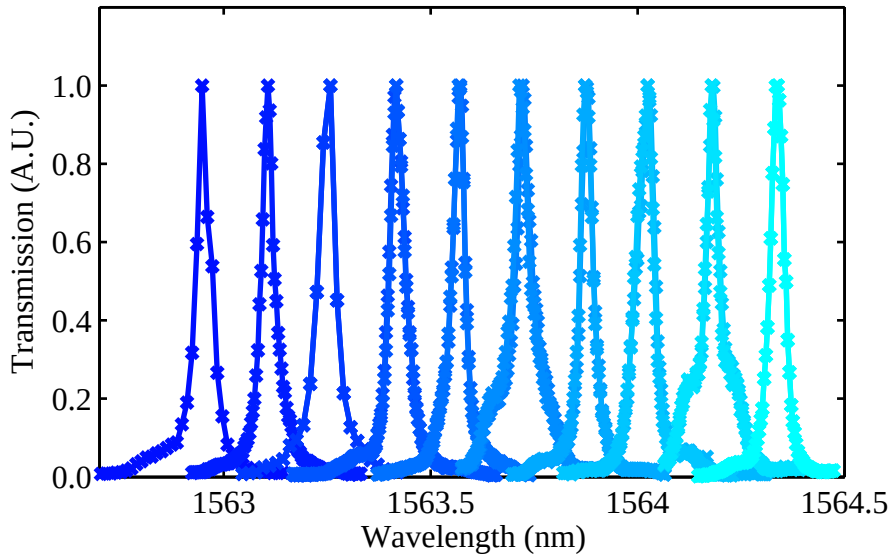

Figure 3.12: Measured microcavity transmission spectra for temperatures of 22°C (darkest blue) to 40°C (lightest blue) in 2°C steps. The position of the resonance is red-shifted with increasing temperature due to silicon's positive TOC, whilst a shift of > 0.5 nm over the 18°C temperature range was observed.

further confirms the need for suitable temperature control. It can also be concluded that the observed tuning is mainly due to the change in refractive index of Si with temperature and not thermal expansion. There may of course be some error on the absolute temperature due to incorrect calibration of the temperature probe, or more likely because it is the mount being heated and not the sample directly, however this should have little impact on the slope of the fit.

3.4 Conclusions

In this chapter the linear transmission properties of two sets of 1D PhC microcavities fabricated on two separate chips were investigated. A large number of devices were found to possess resonance wavelengths outside the tuning range of the laser, whilst the remainder on chip A suffered from low Q-factors and heavily modulated transmission spectra. This may have been caused by additional cavities being formed from multiple reflections, possibly due to stitching errors, although the exact origins are unclear at this time. Fortunately a number of cavities with moderately high Q-factors of ~40,000 were located on chip B. Reproducible wavelength scans were achieved after successfully

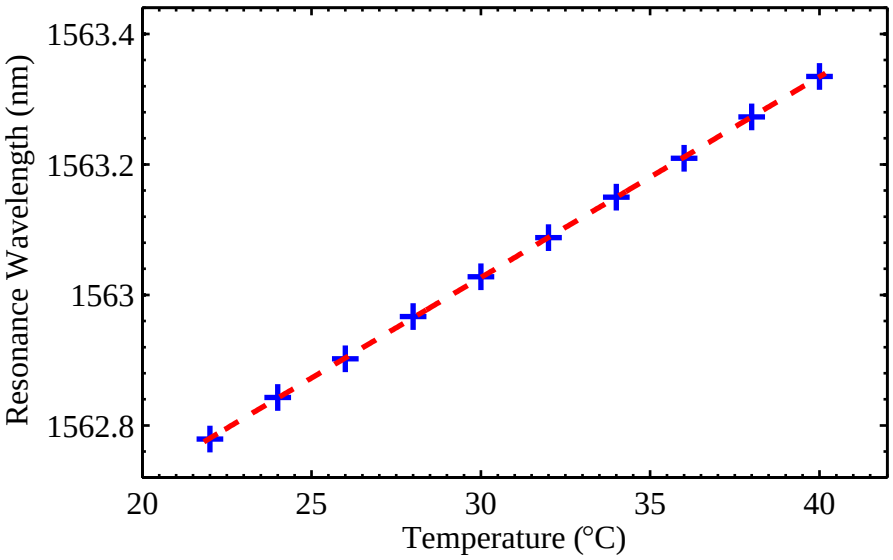

Figure 3.13: Plot of resonance wavelength as a function of temperature for a microcavity. The experimental data points (blue crosses) show excellent agreement with the linear fit (red dashed curve) that has a slope of 77 pm K^{-1}. Error bars are too small to plot on this scale.

stabilising the temperature of the chip to prevent thermal drift of the resonance and by storing it in a vacuum desiccator when not in use to avoid contamination. The thermal stabilisation was achieved through the use of a pair of Peltier devices incorporated into the experimental set-up to stabilise the temperature of the sample mount. This allowed the potential for thermally tuning the resonances to being investigated, with a wavelength shift of $\sim$0.077 nm K^{-1} being measured. Having identified cavities with suitably high Q-factors and stabilised their resonances, the work presented in Chapter 4 will focus on the nonlinear response of these microcavities.

Chapter 4

Nonlinear Properties of 1D PhC Microcavities

Following on from the previous chapter in which the linear transmission of a set of 1D PhC microcavities was examined, the nonlinear properties of those cavities with the highest Q-factors will now be investigated. Nonlinear effects are of particular importance, both from a fundamental point of view and because they are often at the heart of active optical devices. For these reasons nonlinear optics in photonic wires and microcavities has been studied extensively in recent years, with the aim of uncovering new physics and adding to the functionality of on-chip devices. One effect that has received particular attention in microcavities is that of optical bistability, which has been observed in a range of different cavity types utilising a number of different mechanisms. Optical bistability is of great importance for all-optical signals processing, as it can be exploited to create devices capable of displaying optical switching, memory and gain. Here the nonlinear response of the 1D PhC microcavities to CW input light resulting in thermal bistability will be explored, before switching to ns pulses to look at free carrier induced bistability. Finally, longer ns pulses will be used as an input, allowing the interplay between thermal and free carrier effects to be observed.

4.1 Introduction to Optical Bistability

Bistable systems, for which there are two possible states the system can rest in separated by some form of energy barrier, are fundamental to nature and occur in a variety of physical systems in chemistry [143], physics [144] and biology [145]. Typically, the system will involve some kind of positive feedback that gives rise to the bistability. First suggested theoretically [146] and demonstrated experimentally [147] in connection with nonlinear Fabry-Pérot resonators, optical bistability [41] occurs when two different resonant transmission states are possible for a given input or optimal power. In the case of optical devices with feedback, such as laser cavities and resonators, the bistability is typically either absorptive or refractive in nature [148]. In the former, a saturable absorber with an intensity dependent optical loss is used, whilst in the latter a mechanism that typically relies on the intensity of circulating light is used to change the refractive index of the cavity medium. More recently, optical bistability of this type has been observed in a variety of different microcavities, from ring resonators [39] to 1D [149] and 2D PhC microcavities [150], where the index change is usually optically induced and its magnitude depends on the amount of light circulating inside the cavity.

The origin of the positive feedback leading to the bistable behaviour in the case of optical microcavities can be understood intuitively, by considering what happens as the input power, P_{in}, to the microcavity is increased. For a fixed input wavelength, λ, detuned from resonance by an amount $\delta = \lambda - \lambda_{res}$, as P_{in} to the cavity is increased the refractive index, n, of the cavity medium changes, leading to a shift in λ_{res} (since λ_{res} depends on n). Under the right conditions λ_{res} can shift towards the input wavelength, λ, reducing δ and allowing more light to be coupled into the microcavity. This in turn increases the optical power circulating inside the microcavity, increasing the shift of λ_{res} and further increasing the coupling efficiency. This positive feedback leads to a sharp jump in transmitted power, P_{out}, at a particular input power when the input is swept from low to high powers. Thus for a bistable microcavity P_{out} is a strongly nonlinear function of P_{in} [151]. It is also possible for such systems to exhibit hysteresis loops, like that shown schematically in Fig. 4.1, when observing P_{out} as P_{in} is swept from low to high powers and back again. As P_{in} is increased the positive feedback leads to a sudden switch from low to high transmission as described above. Conversely, when sweeping in the opposite direction sufficient power remains circulating inside the microcavity to maintain the shifted position of the resonance and ensure high transmission down to lower powers on the downward seep. A bistable cavity therefore behaves as though it has a 'memory' of its previous state, with the upper or lower branch of the hysteresis loop in Fig. 4.1 followed depending on whether P_{out} was previously high or low.

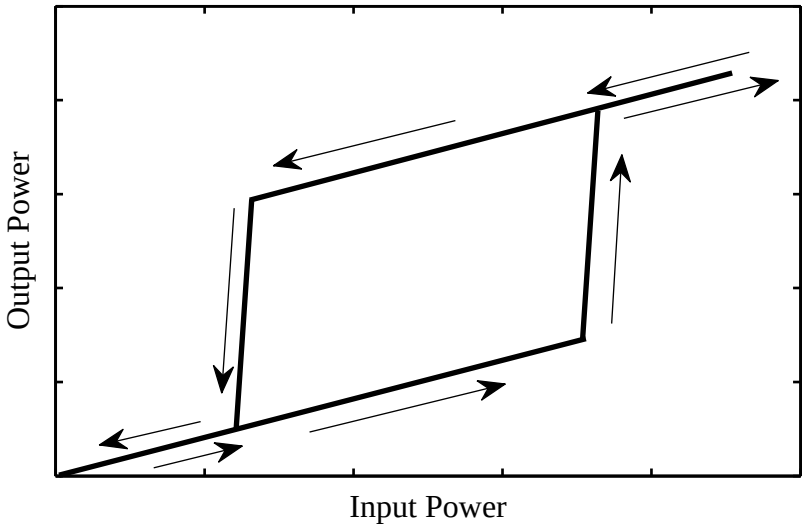

Figure 4.1: Schematic of a hysteresis loop observed when plotting P_{out} as a function of P_{in} for a bistable cavity. The arrows indicate the path taken around the loop when sweeping from low to high values of P_{in} and back again. The width of the hysteresis loop is dependent on the initial detuning δ.

The transmission, $T(\lambda)$, of the 1D PhC microcavities considered in this work can be approximated by a Lorentzian, which in the presence of an optically induced resonance shift, $\Delta\lambda_{res}$, can be written as

$$T(\lambda) = \frac{P_{out}(\lambda)}{P_{in}(\lambda)} \approx \frac{\left(\frac{\delta\lambda}{2}\right)^2}{\left[(\lambda - \lambda_{res} - \Delta\lambda_{res})^2 - \left(\frac{\delta\lambda}{2}\right)^2\right]}, \tag{4.1}$$

where λ is the input wavelength, and λ_{res} and $\delta\lambda$ are the resonance wavelength and FWHM as defined previously. As $\Delta\lambda_{res}$ is dependent on the power circulating (or alternatively energy stored, U) in the cavity, which is in turn proportional to QP_{out}, it is possible to re-write $\Delta\lambda_{res}$ in terms of P_{out} [152]. This leads to a cubic expression for P_{out} in terms of P_{in}, which for

$$|\delta| = |\lambda - \lambda_{res}| > \frac{\sqrt{3}}{2}\delta\lambda \tag{4.2}$$

becomes multi-valued, with one unstable solution that cannot be accessed physically, and two stable solutions corresponding to the upper and lower branches of the hysteresis

curve [153]. The minimum power required to observe bistability is therefore obtained for a detuning of $\delta = \frac{\sqrt{3}}{2}\delta\lambda$, with the exact value depending on the mechanism used to induce the refractive index change. This threshold power is found to be proportional to Q^2/V [154], since a higher Q-factor results in a narrower resonance so that a smaller resonance shift is required to significantly modulate the transmission of the cavity. At the same time, a higher Q-factor leads to a stronger enhancement of the circulating fields on resonance, since light is confined for longer, leading to a larger index change and therefore resonance shift. This explains the Q^2 dependence. At the same time, the intensity of the circulating light is inversely proportional to the cavity volume, since for a given circulating power a smaller cavity mode volume results in a higher intensity. It is for this reason that optical microcavities are particularly suited to observing optical bistability, as their superior confinement ensures they can posses ultra-high Q-factors and close to diffraction limited volumes, resulting in low power thresholds for bistability.

4.1.1 Optically Induced Refractive Index Changes

As stated, the optically induced refractive index changes that cause the shift of the microcavity resonance depend on the amount of light circulating in the microcavity, whilst they can usually be attributed to one of three different mechanisms. The first is the optical Kerr effect, which occurs in materials possessing a third-order optical nonlinearity (non-zero $\chi^{(3)}$) [47]. This results in an intensity dependence of the refractive index that is often written as

$$n(I) = n_0 + n_2 I, \tag{4.3}$$

where n_0 is the linear contribution to the refractive index, I is the intensity of the light and n_2 is the nonlinear index. For Si, n_2 takes a value between 10^{-18} $\mathrm{m^2W^{-1}}$ [62] and 10^{-17} $\mathrm{m^2W^{-1}}$ [155], which is two to three orders of magnitude larger than for silica, out of which microdisks, toroids and spheres are often fabricated. Silicon nitride, another material out of which high Q-factor cavities have been fabricated [156], has an n_2 of just 2.4×10^{-19} $\mathrm{m^2W^{-1}}$ [157] ensuring low nonlinear losses but making them less suited to the observation of nonlinear effects. The n_2 of Si is also comparable to that of aluminium gallium arsenide, which has $n_2 \approx 1.5 \times 10^{-17}$ $\mathrm{m^2W^{-1}}$ and is also used to fabricate microresonators [156].

The positive sign of n_2 in Si leads to a refractive index that increases with increasing intensity, which would cause λ_{res} to shift to a longer wavelength (red-shift) in the case of a cavity fabricated from Si. However, the small magnitude of n_2 for most materials means that high intensities are required to observe an appreciable index change through the Kerr effect. For this reason ultra-short, femtosecond optical pulses are often used, whilst the material itself is assumed to respond instantaneously to the incident light. For this reason, the induced index change begins to occur as soon as the light enters the material and is assumed to last only for the duration of the pulse. The Kerr effect thus provides the fastest method of modulating the refractive index, with the potential for rapid switching between the high and low transmission states of a bistable cavity [158]. One issue however, is that ultra-short pulses necessarily have a large spectral bandwidth e.g. a transform limited pulse 100 fs in duration with a central wavelength of 1500 nm may have a bandwidth in excess of 10 nm. Trying to couple such a pulse into a cavity with even a moderately high Q-factor would lead to a substantial amount of the pulse being reflected out of the cavity, as its bandwidth would exceed the width of the cavity resonance. This necessitates the use of microcavities with relatively low Q-factors, or alternatively that the pulse used to induce the index change is incident on the microcavity from above, rather than being coupled into it [159]. The practicality of the latter approach is questionable for on-chip devices however.

Another issue that can arise when using such high powered pulses in semiconductor cavities is the increased level of TPA, which leads to the generation of free-carriers as discussed in Chapter 1. The presence of the free-carriers will lower the refractive index of the microcavity via the plasma dispersion effect, causing the resonance to shift to shorter wavelengths (blue-shift), in direct opposition to the optical Kerr effect [160]. In silicon, the change in refractive index caused by the change in free-carrier concentrations can be accounted for empirically using the relation [161],

$$\begin{aligned} \Delta n_f &= \Delta n_e + \Delta n_h \\ &= -[8.8 \times 10^{-22} \Delta N_e + 8.5 \times 10^{-18} \Delta N_h^{0.8}]. \end{aligned} \tag{4.4}$$

Here Δn_e is the refractive index change due to the electron concentration change; Δn_h is the refractive index change due to the hole concentration change; ΔN_e is the electron concentration change in cm^{-3} and ΔN_h is the hole concentration change in cm^{-3}. The additional free-carriers also increase the absorption of the optical medium, as mentioned

briefly in Chapter 1, with the change in absorption calculated in a similar manner to the above [161], as

$$\begin{aligned}\alpha_f &= \alpha_e + \alpha_h \\ &= 8.5 \times 10^{-18}\Delta N_e + 6.0 \times 10^{-18}\Delta N_h,\end{aligned} \tag{4.5}$$

where α_e and α_h are the changes to the optical absorption due to the changes in electron and hole concentrations respectively. Whilst detrimental to the optical Kerr effect, the index change caused by the increase in free-carrier concentration can also be used to induce bistability in a microcavity in its own right [43]. If it is assumed that the optical power absorbed due to TPA is P_{TPA}, then the density of free-carriers is given by [43]

$$\frac{\mathrm{d}N}{\mathrm{d}t} + \frac{N}{\tau_c} = \frac{P_{TPA}}{2h\nu V}, \tag{4.6}$$

where $h\nu$ is the energy of a single photon and τ_c is the free carrier lifetime. The associated index shift can then be calculated using Equation (4.4).

In the case of Si microcavities, free-carriers can be generated via TPA due to the high optical intensities that occur for light coupled into the microcavity on resonance, or alternatively via linear absorption if an optical pulse containing photons with energies exceeding ∼1.12 eV is incident on the cavity from above. It is also possible to inject free-carriers through the use of p-i-n junctions integrated on-chip, with this technique having been used successfully to create electro-optic modulators in silicon [35, 162].

For the case where free-carriers are generated through optical absorption, they will begin to accumulate as soon as light is incident on the microcavity region. However, regardless of how the free-carriers are generated, the time taken for them to recombine is fixed by τ_c. This ultimately places a limit on how quickly the refractive index can be modulated, since the microcavity resonance will remain blue-shifted until the free-carriers have recombined. As stated in Chapter 1, τ_c depends on the material and waveguide geometry, with smaller cross-sections usually resulting in a shorter τ_c due to a more rapid recombination of electrons and holes at surface defect sites. For a typical Si waveguide with sub-micron dimensions, τ_c is of the order of nanoseconds, so that refractive index modulations in the GHz range are possible [163]. A more rigorous

description of the index change induced by free-carriers would take into account the non-uniform concentration of electrons and holes in the microcavity region, the diffusion of carriers away from the microcavity region and also a spatially varying τ_c, due to the varying proximity of the electrons and holes to the surface of the silicon where recombination takes place [153].

The final mechanism that has been exploited to induce optical bistability in microcavities is the temperature dependent index shift caused by the TOE [42]. This was discussed in the previous chapter and used successfully to tune λ_{res} by changing the temperature of the aluminium block on which the devices are mounted. Using this method $\Delta\lambda_{shift}$ was found to be ~ 0.077 nm K^{-1}. Using Equation (4.2) and assuming a $\delta\lambda$ of around 40 pm, a temperature change of approximately 0.5 K should therefore be sufficient to observe thermally induced bistability in the high Q-factor microcavities identified in the previous chapter.

As Si is an indirect semiconductor both linear absorption and TPA, as well as electron-hole recombination, are phonon-assisted processes [164], so that all of the light absorbed in the microcavity is eventually converted to thermal energy. Note also that the generated-free carriers are free to absorb as well, leading to further heating. The resulting temperature increase red-shifts λ_{res} due to the positive TOC of Si, leading to a bistable cavity response. Of course, light scattered from the cavity, either through side-wall roughness or at the PhC mirrors, is lost and does not contribute to the microcavity heating. If P_A is the total power absorbed by the cavity, then the change in temperature is given by [43],

$$\frac{\mathrm{d}\Delta T}{\mathrm{d}t} + \frac{\Delta T}{\tau_\theta} = -\frac{P_A}{\rho C V}, \tag{4.7}$$

where τ_θ is the thermal dissipation time, $\rho = 2.3\times10^{-3}$ kg cm^{-3} is the density of silicon and $C = 705$ J kg^{-1} K^{-1} is the thermal capacity. Just as τ_c places a limit on how quickly the cavity index can be modulated using free-carriers, τ_θ places a limit on how quickly the cavity index can be modulated using the TOE. Essentially this is because, although the rate of heating can be increased by increasing the circulating power in the cavity, leading to a larger P_A, the rate at which the cavity cools is fixed by τ_θ. Thus, whilst the initial shift of the resonance can be made to occur more quickly by heating the cavity more rapidly, the time taken for the microcavity resonance to recover to its original position is determined by how quickly the cavity cools and hence τ_θ. This

will of course depend on the exact cavity geometry and materials, which will affect how rapidly heat diffuses away from the microcavity region, but is often found to be of the order of microseconds for Si [141]. Despite the relatively large TOC of Si then, thermally induced changes to the refractive index of Si will occur on much slower time scales than refractive index changes caused by optical Kerr and free-carrier effects.

In reality of course, more than one of these effects can occur, with the resulting index change and resonance shift due to a combination of the above [153]. This is particularly true of thermal and free-carrier effects. Whilst the optical intensities may not be sufficient to induce a noticeable index change due to the Kerr effect, the thermal energy required to cause an increase in temperature occurs because of absorption in the cavity, which requires the generation of free-carriers. Fortunately, the relative time scales over which the three effects occur, combined with the sign of the induced index change (positive for thermal and Kerr; negative for free-carriers), provide a means of distinguishing the dominant effect for a particular situation. For example, thermal effects will always dominate free-carrier effects for a CW input, so that it is necessary to use short pulses to observe the latter. Also, as will be seen at the end of this chapter, with pulses of suitable duration it is possible to operate in a regime in which both thermal and free-carrier effects can occur with similar magnitudes, leading to a strongly modulated cavity transmission.

4.2 Thermally Induced Bistability

The initial experimental set-up used to characterise the thermal response of the cavities was identical to that used in Chapter 3. As well as varying P_{in} at a fixed input wavelength, λ, to observe thermal bistability, another common method involves obtaining transmission spectra by performing continuous wavelength sweeps for different, fixed values of P_{in}. In this situation, if the wavelength is swept from shorter to longer wavelengths through λ_{res}, the resonance is red-shifted and can become locked to the input wavelength, resulting in an increasingly asymmetric transmission spectrum [165]. This is because, as λ is tuned towards λ_{res} from the short wavelength side, more light is coupled into the cavity resulting in increased absorption and a temperature increase. This in turn leads to a red-shift of the resonance via the TOE, so that λ_{res} shifts in the same direction as the input wavelength. As the detuning between the input light and the red-shifting microcavity resonance is reduced, more light is coupled into the cavity further red-shifting λ_{res}. Eventually there will come a point however, when the circulating

power inside the microcavity is no longer enough to maintain this continued red-shift of the resonance. At this point, as λ continues to be tuned to longer wavelengths the coupling to the cavity will be reduced. For a resonance shift, $\Delta\lambda_{res} > \sqrt{3}/2\delta\lambda$, this results in what was previously a positive-feedback loop becoming a negative-feedback loop. As the coupling to the cavity is reduced, the cavity begins to cool resulting in λ_{res} blue-shifting back towards the original 'cold-cavity' resonance position, further reducing the coupling efficiency. The net result is a sharp drop in cavity transmission, indicating a bistable cavity response [95]. It is clear then that a higher P_{in} will result in a greater red-shift and more asymmetric transmission spectra. At the same time, to maximise the red-shift for a given P_{in} it is necessary to sweep the input wavelength sufficiently slowly to allow the microcavity time to heat up.

Unfortunately the laser used here is not capable of continuous wavelength tuning and instead must be stepped, with the laser output switching off whilst tuning to each new wavelength for a given scan. This means that during each wavelength step the cavity has time to cool, allowing the resonance time to shift back to the 'cold-cavity' resonance position between individual measurements. Even using this method however, one would still expect to observe an asymmetry in the measured transmission spectra, as the microcavity is briefly heated by the input light, before cooling again as the laser switches off and tunes to the next wavelength. Measurements of the transmission spectra for varying input powers were thus performed here using a CW input, with the wavelength stepped from shorter to longer wavelengths. With a frequency step of 0.5 GHz the corresponding scan times were of the order of a minute i.e. slowly enough for both the cavity to heat up during the scan and also for the reading on the lock-in amplifier to stabilise, given the 30 ms time constant. This method of examining the thermal response of the microcavities was preferred initially, as it should allow a more accurate estimate of the threshold power for observing bistability. This is because this approach is less likely to be affected by temperature fluctuations than attempting to sit at a fixed detuning and varying P_{in} to observe hysteresis loops, even with the methods used to stabilise the temperature outlined in Chapter 3.

A number of different transmission spectra obtained for P_{in} varying from 30 µW to 320 µW are shown in Fig. 4.2 for a cavity with $Q \sim 40,000$. The red-shift of the cavity resonance along with the increasing asymmetry is clear as P_{in} is increased. For powers in excess of 240 µW (grey and black plots in Fig. 4.2) the sharp fall in transmission on the long wavelength side of the resonance associated with a bistable cavity response is also clearly visible. This implies a threshold P_{in} of around 240 µW to

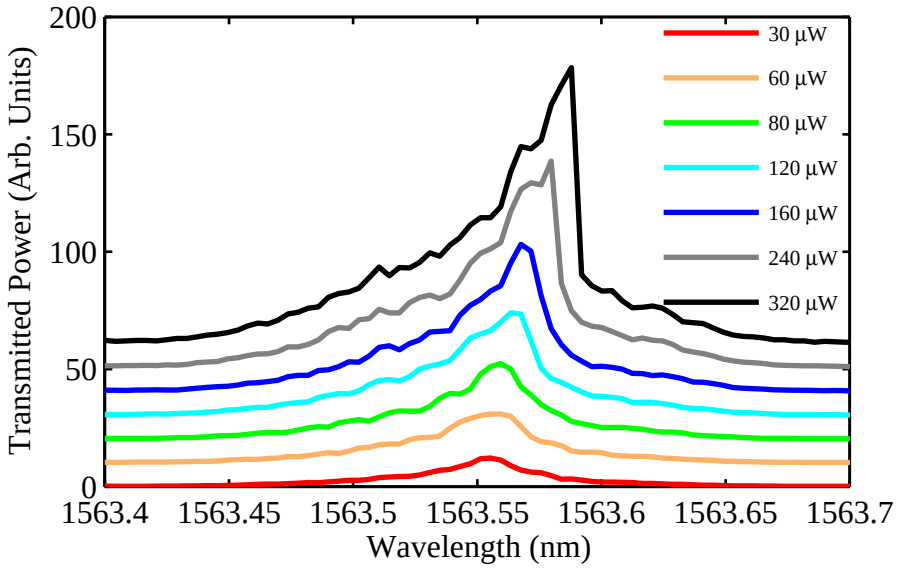

Figure 4.2: Measured microcavity transmission spectra performed for increasing input powers, measured before the input coupling lens. The wavelength of the input light is stepped from shorter to longer wavelengths, resulting in a broadening and red-shift of the resonance at higher powers due to cavity heating. The red-shift and asymmetry of the spectra increases with increasing input power, whilst the sharp transition from high to low transmission characteristic of optical bistability is observed for input powers of ∼240 µW and greater (grey and black curves).

observe bistability in this particular cavity. It is also possible to extract the wavelength of peak transmission from each of the spectra shown in Fig. 4.2, in order to produce a plot of peak wavelength as a function of P_{in}, like that shown in Fig. 4.3. From this it can be seen that for input powers up to 70 µW there is insufficient power in the microcavity to cause a measurable red-shift of the resonance. However, for input powers exceeding this there is an approximately linear relationship between peak wavelength and P_{in}, illustrated by the red curve in Fig. 4.3 which is a linear fit to the experimental data (excluding the first five data points). The slope of the linear fit indicates a wavelength shift of 120 pm mW^{-1}. The data measured in the previous chapter that suggested a wavelength shift of $\sim$ 80 pm K^{-1} therefore implies an optically induced temperature change of 1.5 K mW^{-1}. This is consistent with the values measured by Lipson et al. [42] who noted a 200 pm mW^{-1} resonance shift due to the TOE in silicon-on-insulator ring resonators. The slightly stronger dependence of peak wavelength on input power noted there may be due, at least in part, to the fact that the laser used here is step tuned and so switches on and off between tuning. The microcavity thus has a chance to cool

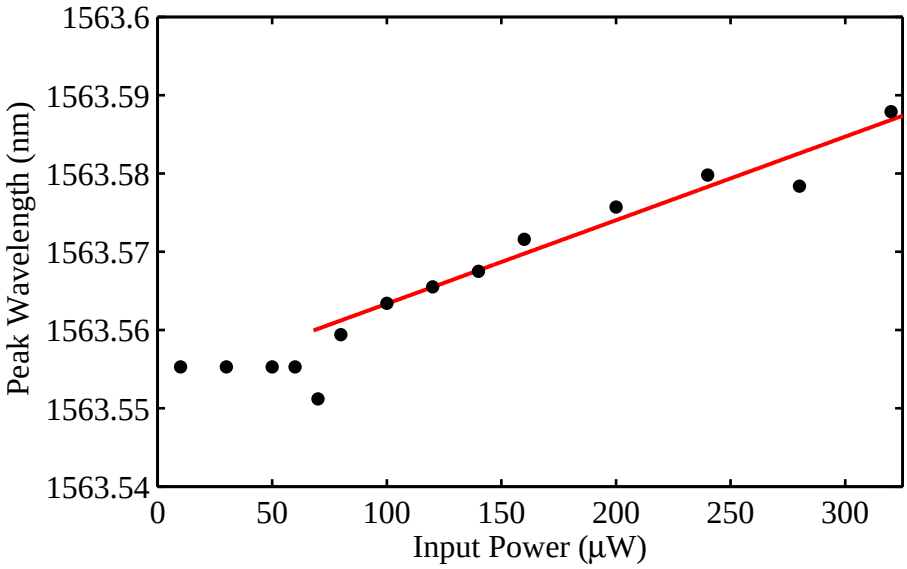

Figure 4.3: Plot of peak wavelength as a function of input power, extracted from the experimentally measured data shown in Fig. 4.2. For input powers exceeding approximately 70 µW the cavity resonance begins to red-shift, with an approximately linear relationship between λ_{res} and P_{in}, as evidenced by the red curve which is a linear fit to the experimental data.

down between each wavelength step, so that the maximum possible shift is reduced. The fact that the wavelength shift appears to be a linear function of input power would suggest that either linear absorption, or possibly TPA-induced free carrier absorption, is the dominant form of absorption occurring within the microcavity and not nonlinear TPA, which one may have expected. It is also important to note that the estimated threshold power of 240 µW required to observe bistability in this case is measured immediately before the input coupling lens. Taking into account the estimated input coupling loss of ~ 4.6 dB from the previous chapter, a power of 240 µW corresponds to an in-waveguide power of around 80 µW. This is a lower threshold power than in [42], which is not surprising given the increased Q-factor and reduced V of the microcavities used here, but the result also compares favourably with measurements taken for other 1D microcavities specifically designed for a strong thermal response [149]. Here a threshold power of just 1.6 µW was measured for a so-called 'air-bridge' microcavity, but the Q-factor was considerably higher at 220,000.

Next, measurements of P_{out} as a function of P_{in} were obtained for the same microcavity for a range of different detunings, δ, with the aim of observing hysteresis loops. The power sweeps, like the wavelength scans, were for a CW input and automated via a

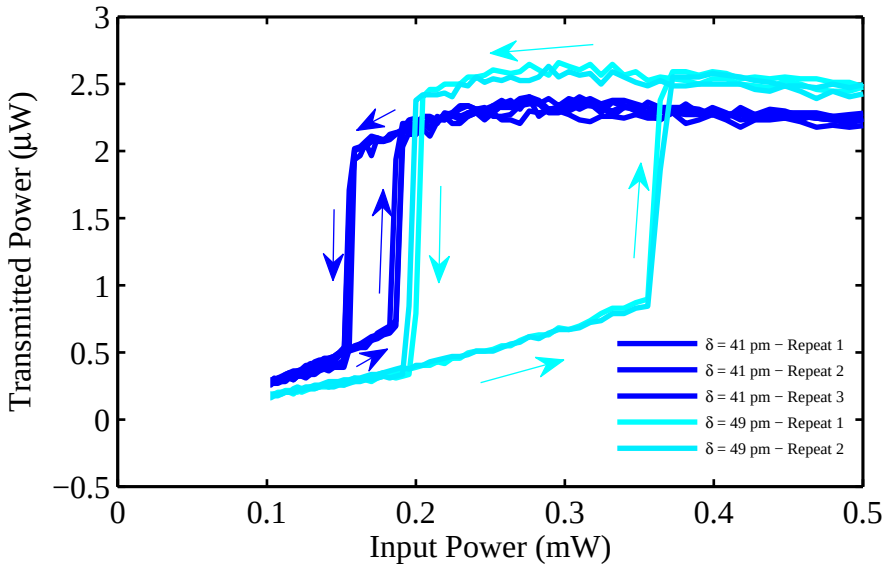

Figure 4.4: Repeat measurements of P_{out} as a function of P_{in} for two different positive detunings, demonstrating the repeatability of the power sweeps. Hysteresis loops indicating bistable operation are observed for both detunings, with the arrows indicating the path taken around the loop when stepping up and down in power.

custom written LabView script, with additional power control again provided by the variable ND filter before the chip. It is important to note however that the laser was not switched off throughout the scans as the power was varied, unlike for the wavelength scans performed previously. The output powers were obtained by calibrating the lock-in amplifier signal using a known power, measured after the output coupling lens and PBS using the same power meter used in Chapter 3. Again, it was necessary to ensure the input power was varied slowly enough to allow the cavity to heat up and cool down. Initially, in an attempt to ensure maximum reproducibility of the results obtained, as well as stabilising the temperature of the device (see Chapter 3), low power wavelength scans were performed between each power sweep. This allowed any possible drift of the resonance to be accounted for by adjusting λ to maintain a constant δ, although ultimately this proved unnecessary as the resonance position remained stable. It also allowed the input coupling to the device to be monitored, as any change to the coupling would lead to a change in the maximum transmitted power on resonance. Repeat measurements of P_{out} as a function of P_{in} are shown for two different values of δ in Fig. 4.4. In each case, hysteresis loops are observed and show good reproducibility for each δ.

Having established that the power sweeps could be repeated reproducibly, more were obtained for positive values of δ from +20 pm to +49 pm, the results of which are plotted in Fig. 4.5. Starting with δ = +20 pm, no hysteresis is observed although P_{out} is a nonlinear function of P_{in}. As δ is increased the curve becomes steeper, until eventually there is a step transition from low to high transmission and back again, corresponding to δ = +29 pm in Fig. 4.5. The sharp transition and lack of hysteresis corresponds to the ideal detuning for optical switching. For larger values of δ the cavity is operating in the bistable regime, with hysteresis loops like that shown schematically in Fig. 4.1 clearly visible. For an increasing P_{in} the lower path is taken, corresponding to the low transmission state, whereas when sweeping P_{in} from high to low, the upper path is taken and the microcavity transmission remains high.

Interestingly, the threshold power for bistability, which corresponds to the location of the large jump in transmitted power on the upward sweep, is around 50 µW for δ = 34 pm (the smallest value of δ for which bistability is observed) after taking into account insertion losses. This value is close to the 80 µW threshold obtained from the wavelength sweeps for a fixed P_{in} described above. As δ is increased the power required to switch from a low to high transmission increases, since λ_{res} needs to be shifted further to coincide with λ, resulting in wider hysteresis loops. It is also clear from Fig. 4.5 that on the upper branches of the hysteresis loops, as the input power is increased the output power varies sub-linearly and then actually begins to decrease. This could potentially be due to some nonlinear saturation of the transmitted power, due to either TPA or possibly TPA-induced FCA. It may also be that as the input power is increased further the cavity continues to heat up, eventually causing the resonance to red-shift beyond the input wavelength, causing the detuning to increase and the transmitted power to drop. The hysteresis loops shown in Fig. 4.5 were all obtained for positive detunings i.e. $\lambda > \lambda_{res}$, which is necessary to ensure the positive feedback required for bistability as the increase in temperature of the microcavity causes the resonance to red-shift. Conversely, for a negative detuning ($\lambda < \lambda_{res}$) one would expect to observe no hysteresis, as the resonance is now being shifted away from the input wavelength as P_{in} is increased. Figure 4.6 shows P_{out} as a function of P_{in} for δ = -33 pm, confirming that indeed, no hysteresis is observed for negative detunings. This also confirms that the dominant mechanism causing the change in refractive index in this case (CW input) is the TOE. At this particular detuning, δ = -33 pm, for powers above approximately 0.25 mW, P_{out} begins to vary sub-linearly with increasing P_{in} implying that P_{out} will eventually saturate, suggesting the microcavity is displaying optical limiting effects. Again, this can be understood intuitively by considering what

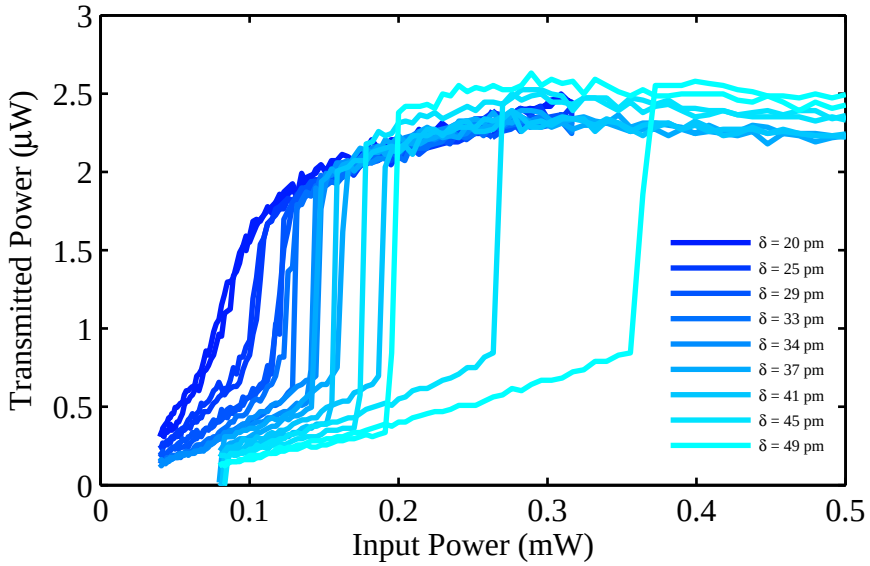

Figure 4.5: Measurements of P_{out} as a function of P_{in} for a number of positive detunings. The hysteresis loop begins to open up between $\delta = 33$ pm and $\delta = 34$ pm at around 140 µW of input power and continues to broaden for increasing δ.

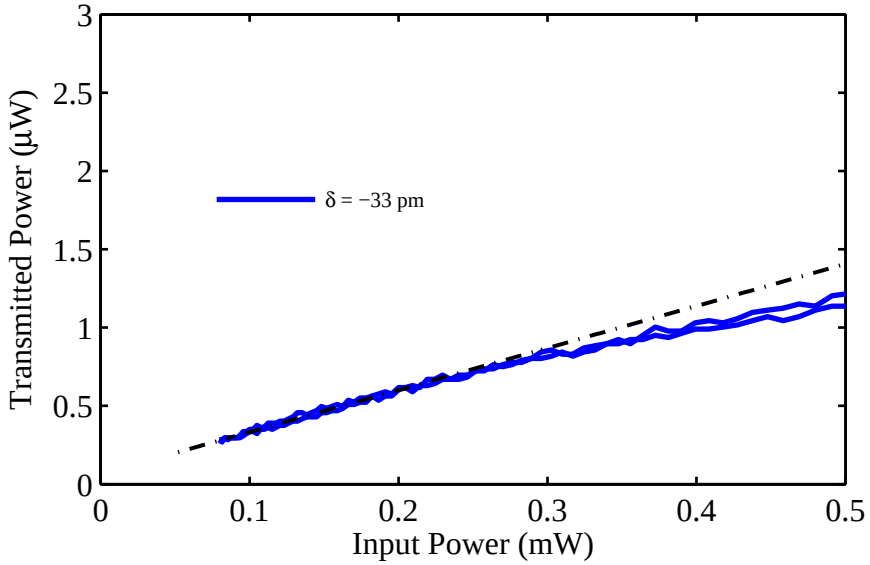

Figure 4.6: Measurement of P_{out} as a function of P_{in} for a single negative detuning of $\delta = -33$ pm. Compared to an equal, positive detuning (see Fig. 4.5) no hysteresis is observed because, as P_{in} is increased the positive TOC of Si causes the resonance to shift away from the wavelength of the input light, as opposed to towards it for the case of positive detuning. The dashed-dotted curve is a linear plot for comparison.

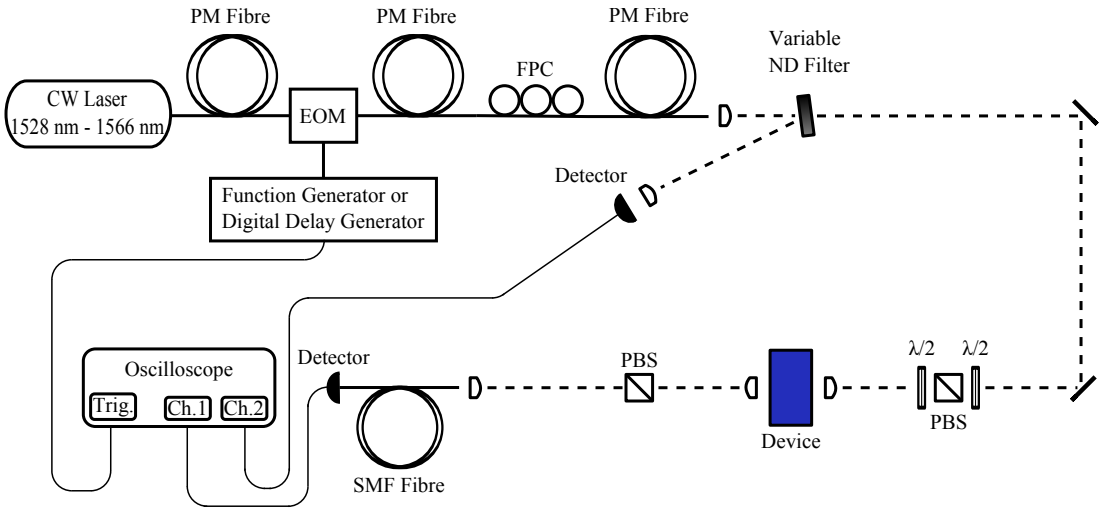

Figure 4.7: Experimental set-up used for the remaining experiments. The addition of the electrooptic modulator (EOM), driven using either a function generator or digital delay generator, necessitates the use of a fibre polarisation controller (FPC) after it, to preserve the linear polarisation of the laser light. The reflection from the ND filter is directed to a lens and focussed onto a detector to monitor the input signal to the microcavities.

happens as P_{in} is increased. More light will be coupled into the microcavity, causing an increased red-shift of λ_{res} so that it moves further from λ. Thus the increase in incident power is compensated for by the reduced coupling efficiency to the microcavity, caused by the increasing δ, resulting in a saturation of the transmitted power at a much lower value than seen for the case of positive detuning.

One of the main applications of optical bistability is all-optical memory, in which the output power is switched between two, stable transmission states. This is achieved below through a modulation of the input power, making it possible to move to different points on the hysteresis curve for a particular microcavity. In order to modulate the CW input light and at the same time monitor P_{in} it was necessary to modify the initial experimental set-up. Figure 4.7 shows a schematic of the experimental set-up used for the all-optical memory demonstration and for the remaining experiments in this chapter. A 10 GHz electro-optic modulator (*Thorlabs*; LN56S-FC), driven by either a digital delay generator (*Stanford Research Systems*; DG645) or digital function generator (*TTi*; TG5011) provided the modulation of P_{in}. The input waveform was monitored by taking the reflection from the ND filter and focussing it onto a detector (*Thorlabs*; PDA10CS) connected to channel 2 of a 300 MHz oscilloscope (*Tektronix*; DPO 3032), triggered from either the delay or function generator respectively. The

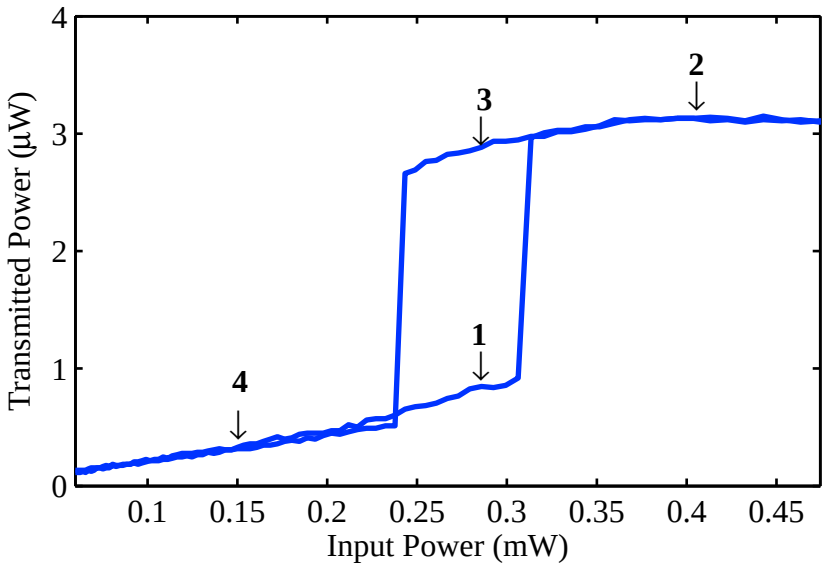

Figure 4.8: Measurement of P_{out} as a function of P_{in} for $\delta = 40$ pm showing hysteresis. The arrows labelled 1 to 4 indicate the values of P_{in} used as the modulated input to the microcavity in order to demonstrate all-optical memory.

oscilloscope also replaced the lock-in amplifier used previously for recording of the transmitted signal, with the output from the detector connected to channel 1 of the oscilloscope. This allowed continuous monitoring of the input and output waveforms simultaneously. It was also necessary to replace the detector used previously to measure the output from the microcavities with a detector with a larger bandwidth (*Thorlabs*; PDA10CF), in order to accurately measure P_{out}.

To demonstrate all-optical memory it was first necessary to again record a hysteresis loop for the microcavity, which is shown in Fig. 4.8. A detuning of $\delta = +40$ pm was used as this was large enough to ensure hysteresis in the power sweep, a condition for all-optical memory, but one that was not so large that it would require large modulations of P_{in} to observe the effect. It is interesting to note that this is the same microcavity as that used for the measurements shown in Fig. 4.5, however the width of the hysteresis loop and the threshold power have increased relative to the previous measurements. This may be due to changes to the input and output coupling, or possibly degradation of the sample over time, however the measured cavity Q-factor was the same as when the previous measurements were taken. Of course this does not affect the observation of all-optical memory, other than to slightly change the input powers involved.

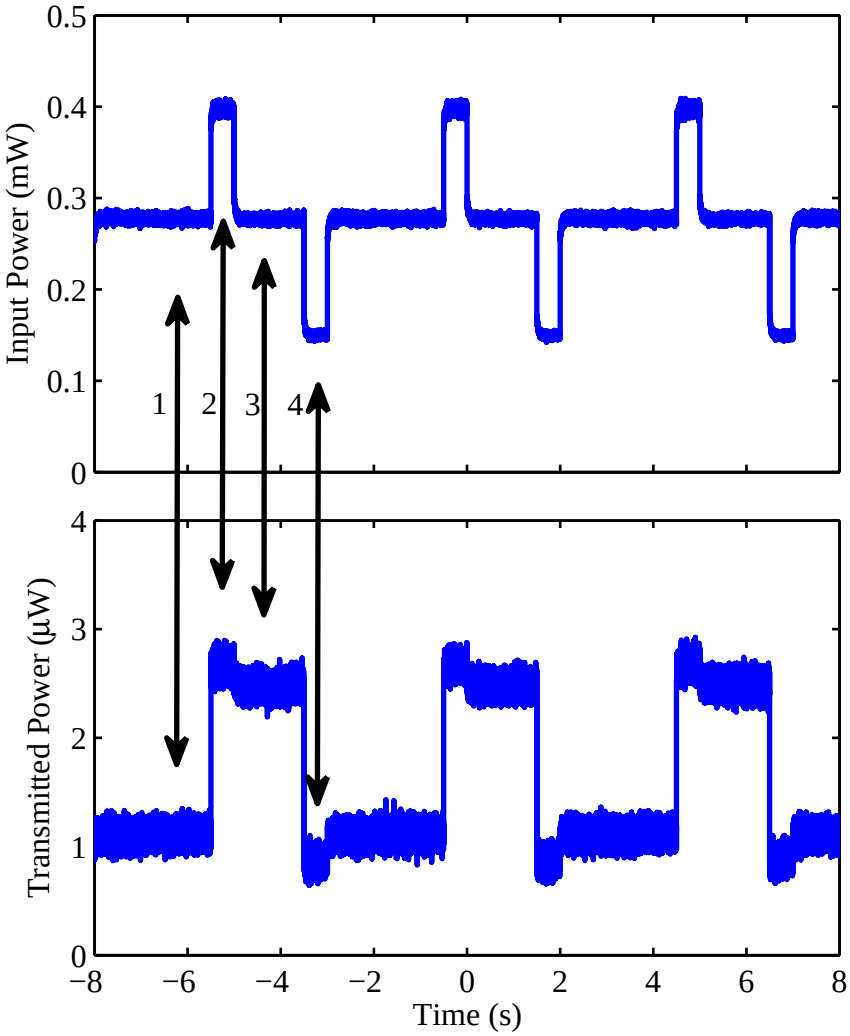

Figure 4.9: Top - Measured input waveform for observing all-optical memory for $\delta = 40$ pm. Bottom - Resulting measured microcavity transmission, showing the modulation of the output between high and low transmission states, demonstrating all-optical memory functionality. Note the time scale is of the order of seconds, showing the stability of each state. The double-headed arrows labelled 1 to 4 link these time-domain plots with the positions on the hysteresis curve shown in Fig. 4.8.

From Fig. 4.8 it can be seen that P_{in} = 2.8 mW (arrow 1) lies within the hysteresis loop, meaning there are two possible transmission states for this value of input power. Assuming this is the initial value of P_{in}, the cavity will be in the stable, low transmission state with $P_{out} \sim 900$ nW, whilst an increase in P_{in} to a value of $\sim$ 0.4 mW (arrow 2) would shift the transmission of the microcavity to a value outside of the hysteresis loop, with $P_{out} \sim 3\,\mu$W. A subsequent reduction of P_{in}, back to the initial value (arrow 3), would result in a shift of P_{out} to the high transmission state, $P_{out} \sim 2.8\,\mu$W. In order to return to the low transmission state it is then possible to reduce the value of P_{in} to 0.15 mW, a value below the hysteresis loop (arrow 4), before again returning to the initial value of P_{in}.

The top plot in Fig. 4.9 shows the input to the microcavity used to display optical memory in the time domain. The input powers used are those described above, with the numbers 1 to 4 indicating the position on the hysteresis curve and the double-arrows linking to the positions on the output signal, shown in the bottom plot of Fig. 4.9. As can be seen, starting in the low transmission state (double-arrow 1), the input power is increased briefly to 0.4 mW (double-arrow 2), causing the cavity to switch to the high transmission state, in which it remains (double-arrow 3) until P_{in} is briefly reduced to 0.15 mW (double-arrow 4), when it switches back to the low transmission state. This demonstrates the microcavities are capable of displaying optical-memory, with, in this case, a 3 dB difference between the high and low transmission states, which are stable for time-scales of at least seconds. The measured transmitted powers shown in the bottom plot of Fig. 4.9 also show good agreement with those in Fig. 4.8 at each point on the hysteresis loop. The threshold switching powers here are an order of magntnitude smaller than those obtained for a Si ring-resonator utilising the TOE effect [42], however the transmitted powers in this case are two orders of magnitude smaller due the higher transmission losses of the 1D PhC microcavity used here.

Due to the relatively long time-scales involved in the measurements shown in Fig. 4.9 the transitions between the high and low transmission states appear to be instantaneous. Of course, the microcavities take a finite amount of time to heat-up and cool down, so that the transitions actually occur over a finite time-scale, related to τ_c, corresponding to the non-steady-state. In order to better show this the above measurements were repeated, but with the durations of the increase in power (double arrow 2) and decrease in power (double arrow 4) reduced to just 5 µs, as shown in the top plot of Fig. 4.10. The bottom plot in Fig. 4.10 again shows the measured output in the time domain, where the switching between states is once again clearly visible. Unlike in Fig. 4.9 however,

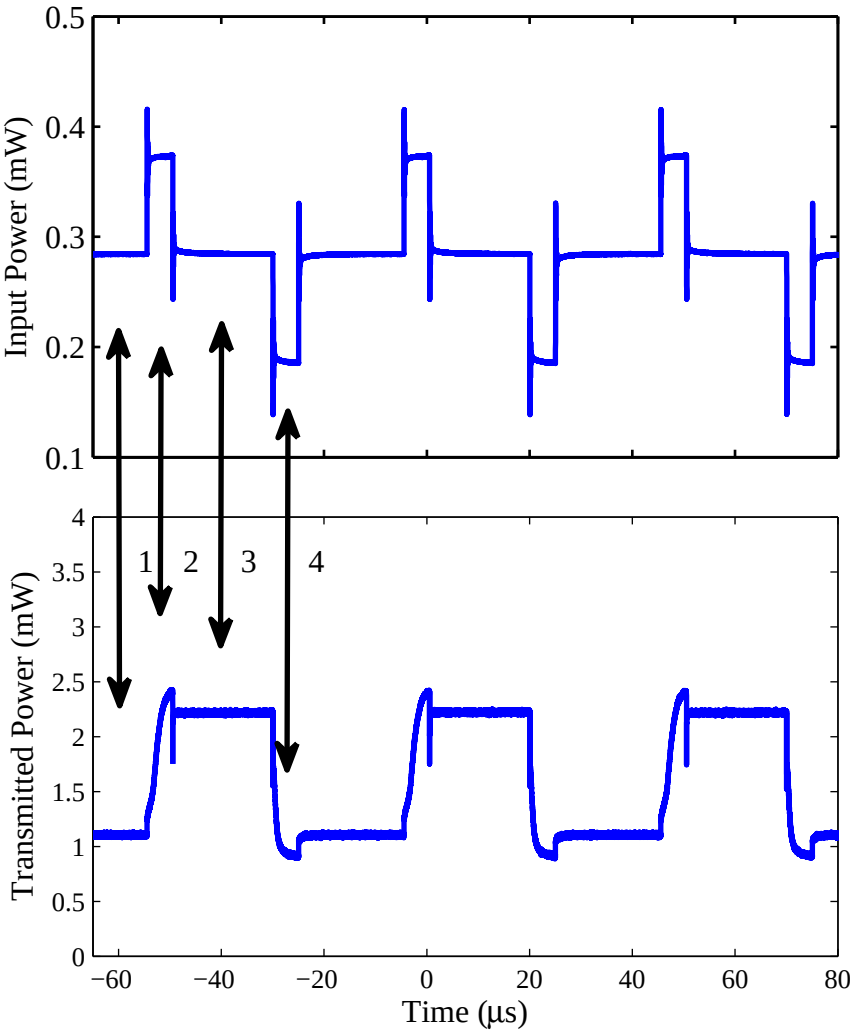

Figure 4.10: Top - Measured input waveform for observing all-optical memory for $\delta = 40$ pm on microsecond time-scales. Bottom - Resulting measured microcavity transmission, again showing the successful modulation of the output between high and low transmission states, but for microsecond durations. The finite time taken for the microcavity to heat-up and cool down is clearly visible, as the output does not immediately follow the input (top). Some 'ringing' in the measured signals can also be observed, which is an artefact due to both detectors' inability to respond to step changes in the signal. The double-headed arrows labelled 1 to 4 again link these time-domain plots with the positions on the hysteresis curve shown in Fig. 4.8.

the time scales are now sufficiently short that the non instantaneous time-scales for the transitions can be seen. When looking at the measured signals in Fig. 4.10, some 'ringing' is visible, even though the bandwidth of the detectors used to measure both the input and output should be sufficient to respond to the changing signals. This is most likely due to the fact that the input contains step increases and decreases in power, whilst the detectors are optimised for bandwidth and not impulse response. Despite this, comparing the input waveform (Fig. 4.9 (top)) with the output waveform (Fig. 4.9 (bottom)), it is clear that whilst the input still varies in a step wise manner, resembling a square wave, the delayed response in the output is evident as the cavity first heats up and then cools down. At this particular detuning and for the power levels considered here it was possible to make the step up in power (double arrow 2) as short as 2 µs and the transition would still occur, whilst for shorter times the microcavity would remain in the low transmission state, implying there was insufficient time for the cavity to heat-up. At the same time the step down in power (double arrow 4) could be made as short as 1 µs before the microcavity would no longer switch back to the low transmission state.

Assuming the temperature variation, ΔT, of the microcavity that induces the wavelength shift, $\Delta\lambda_{shift}(\Delta T)$, varies exponentially with time according to [166],

$$\Delta T = T_0 e^{-\frac{t}{\tau_\theta}}, \tag{4.8}$$

where T_0 is the maximum temperature increase, this can be incorporated into the expression for the microcavity transmission, Equation 4.1. The resulting expression can then be fitted to a section of the falling part of the curve in Fig. 4.10 to extract an estimate of τ_θ. Using this method a value of 0.6 µs for τ_θ provides a good fit to the experimentally measured data, as can be seen in Fig. 4.11.

The time the microcavity takes to heat-up at a given δ will of course depend on the input power used to induce the change to the high transmission state, which for the results shown in Fig. 4.9 (top) and Fig. 4.10 (top) correspond to the maximum input power. A larger increase in P_{in} will lead to a greater absorbed power, causing a more rapid heating of the microcavity, which should in turn lead to a more rapid transition from the low to high transmission states. The effect of varying the maximum input power to a microcavity is shown in Fig. 4.12, where an expanded view of the transition from low to low high transmission is shown for four different powers. For the lowest maximum input power shown in Fig. 4.12 ($P_{in} = 0.72$ mW, brown curve), the maxi-

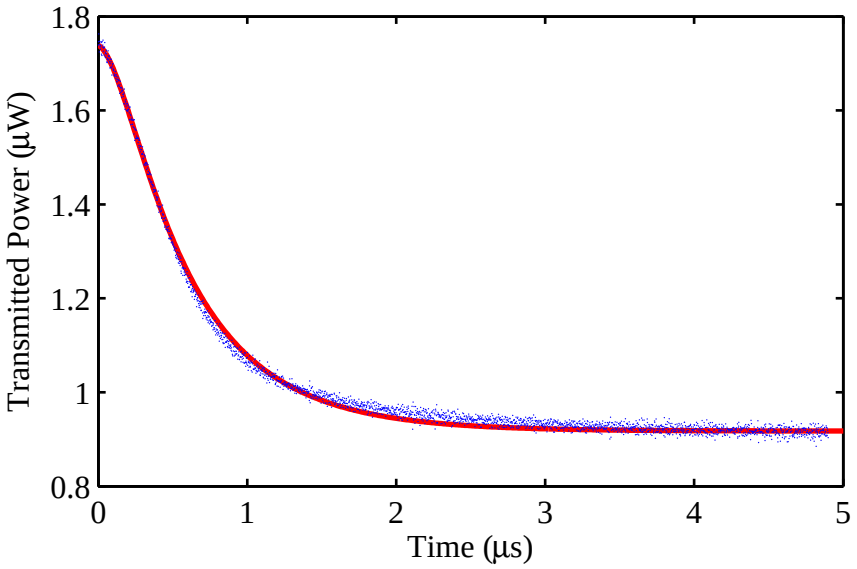

Figure 4.11: A fit (red curve) to a section of the experimental data (blue dots) shown in Fig. 4.10, assuming an exponential dependence of the temperature variation of the microcavity. The thermal time constant extracted from the fitted curve is estimated to be 0.6 µs.

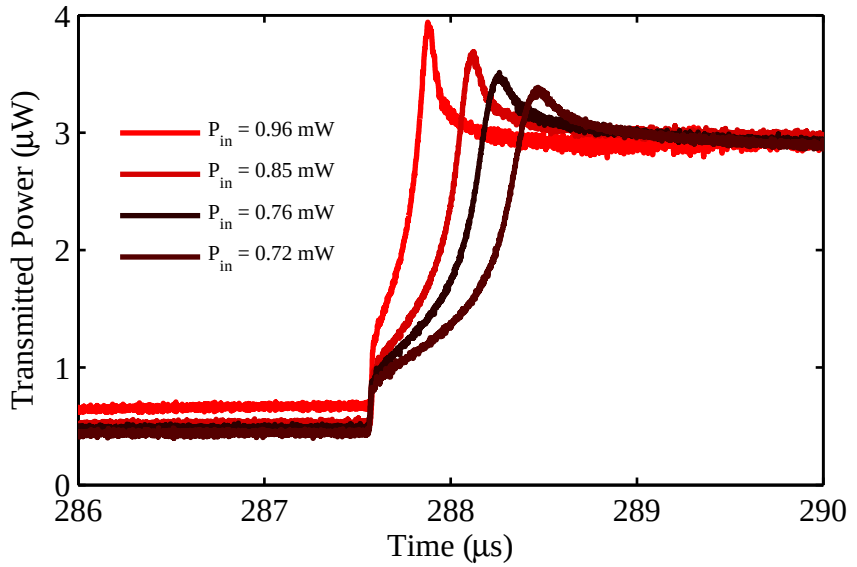

Figure 4.12: Measured transmission of a microcavity, showing an expanded view of the transition from the low to high transmission state for different maximum P_{in}'s. From the plot it is clear that increasing the maximum P_{in} leads to a more rapid transition, as the microcavity heats up more quickly.

mum transmission occurs approximately 1 µs after the input power is increased (at $\sim$ 287.6 µs), whilst for the highest power (P_{in} = 0.96 mW, red curve) the time to reach the maximum transmission is <0.5 µs. This clearly demonstrates that rapid switching of the optical microcavity between the two stable transmission states is possible, with sub-microsecond switching times accessible for sufficiently high values of P_{in}.

Another method that can be used to estimate the thermal switching times of the microcavities considered here is to sit at a fixed positive δ and vary P_{in} sinusoidally over a range of powers for which bistability can be observed in the steady-state. The presence of bistability will distort the sinusoidal input so that the measured transmission will resemble a square wave. As the frequency of the input sine wave is increased, there will come a point when the microcavity will no longer be able to heat-up rapidly enough for bistability to occur (for the given δ and range of input powers used), so that the output signal will no longer be distorted and will resemble the input sine wave. At this point the cavity is no longer operating in the bistable regime.

For these measurements the digital delay generator used previously to drive the optical modulator was replaced by a function generator (*TTi*; TG5011), which provided the sine wave input to the microcavities. The oscilloscope was also set to the maximum number of averages (500) when recording the input and output signals, in order to reduce noise. Figure 4.13 shows the measured oscilloscope trace of the transmitted signal (bottom) for a 1 kHz sine wave input to the microcavity (top) at δ = +41 pm. The presence of bistability is clear as the transmitted signal appears much more like a square wave, due to the switching of the microcavity between the high and low transmission states as the input power is varied.

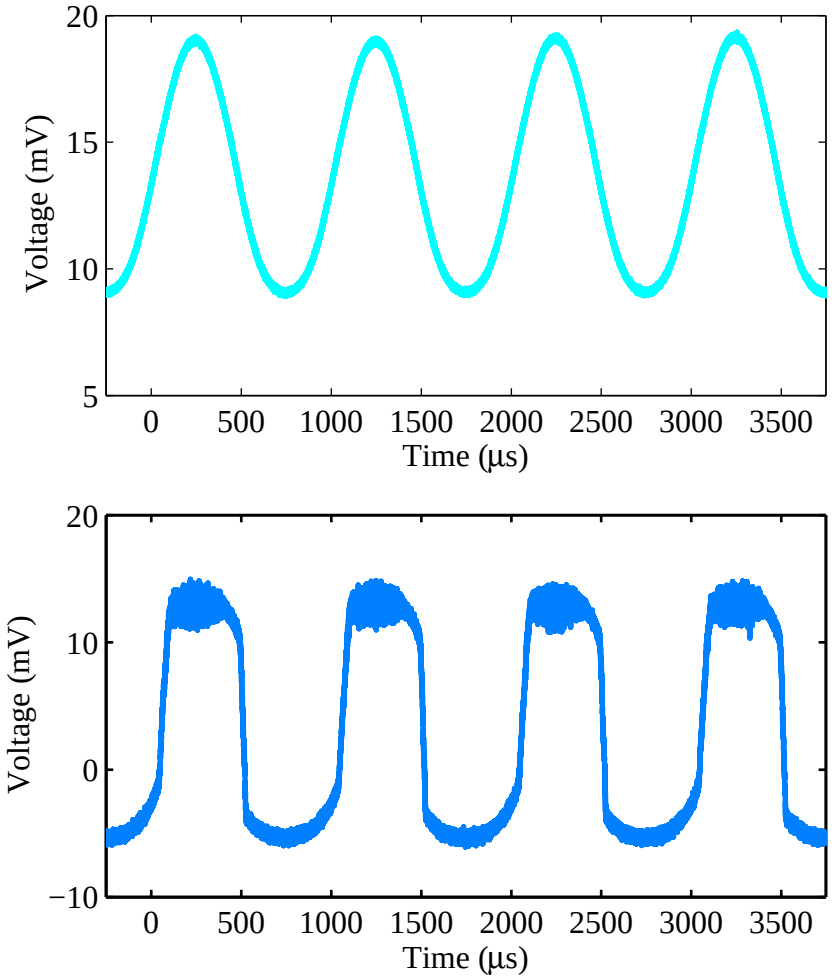

Figure 4.13: Measured oscilloscope trace for the microcavity transmission for $\delta = +41$ pm (Bottom). Optical bistability is indicated by the distortion of the output compared to the 1 kHz sine wave input (Top). The transitions between the two bistable transmission states of the microcavity as the input power is varied distorts the input, resulting in a more square-wave like transmitted signal. The sudden increase and decrease in transmitted signal are also asymmetric in time with respect to the input sine wave. The sharp drop in the transmitted signal occurs later on the falling edge of each oscillation of the sine wave than the sharp increase does on the rising edge.

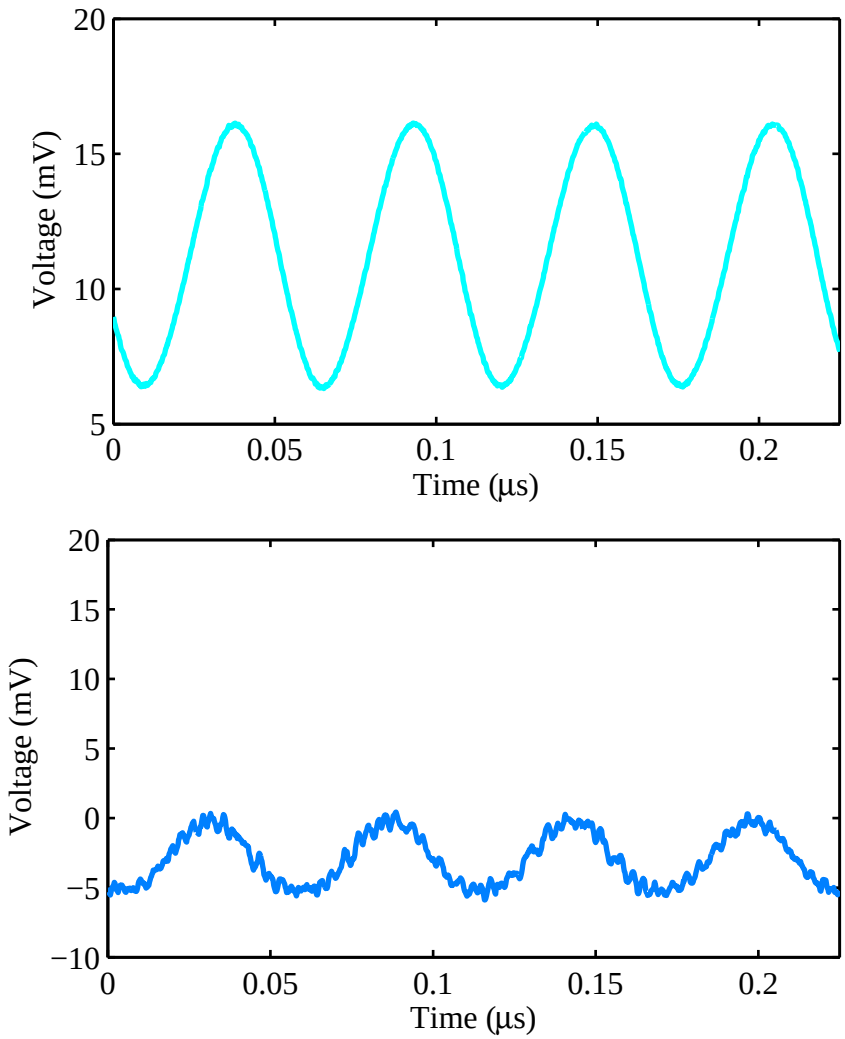

Figure 4.14: Measured oscilloscope trace for the microcavity transmission for $\delta = +41$ pm (Bottom) with a 9 MHz sine wave input (Top). At this frequency (for the given input powers and δ) no bistability is observed and the transmitted signal is a simple sine wave like the input.

For an input sine wave with a frequency of 9 MHz, like that shown in the top plot in Fig. 4.14, the microcavity no longer has sufficient time to heat-up, so that no optical bistability occurs. The resulting transmitted signal, the bottom plot in Fig. 4.14, follows the input signal and is a simple sine wave. The amplitude of the transmitted signal is also much smaller, as the microcavity is no longer switching to the stable high transmission state.

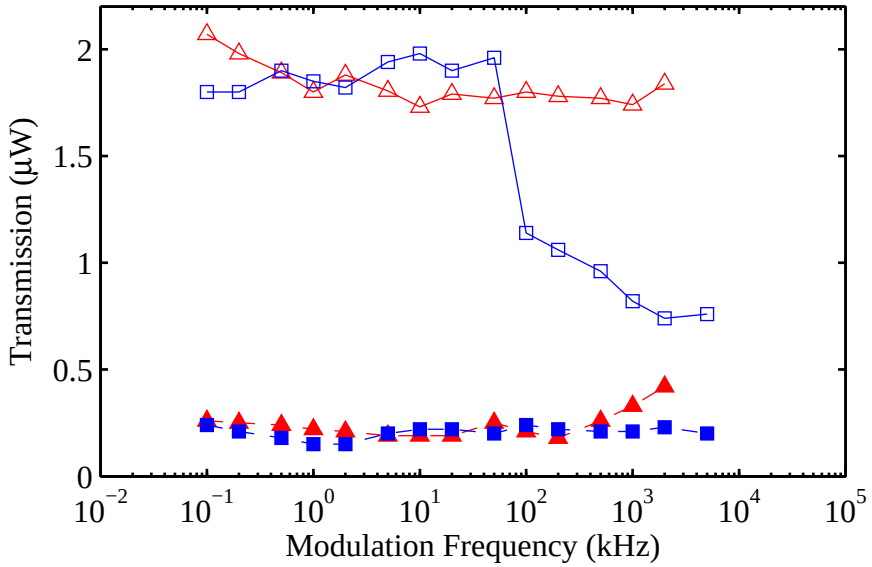

Figure 4.15: Measured maximum (hollow markers) and minimum (filled makers) transmitted power as a function of input sine wave frequency at $\delta = +41$ pm for a peak input power of 0.33 mW (squares) and 0.66 mW (triangles).

By looking at a range of input sine wave frequencies and two different amplitudes, corresponding to different maximum input powers, it is possible to further examine the thermal time response of the microcavities. A plot of maximum transmitted power as a function of input sine wave frequency is shown in Fig. 4.15 for peak powers of 0.33 mW (blue curve) and 0.66 mW (red curve). For 0.33 mW the maximum transmitted power remains fairly constant at just below 2 μW, before falling to $\sim$ 1 μW at 100 kHz, indicating that bistability is no longer occurring. By contrast, for the measurements for a peak input power of 0.66 mW, the microcavity transmission remains fairly constant at around 1.7 μW up to 1 MHz, again demonstrating that the more rapid switching can be achieved using higher powers. Interestingly however, for the higher peak input power, at frequencies above 1 MHz the square-wave distortion is no longer visible and the output resembles a sine wave, implying no optical bistability, however the maximum transmitted power remains approximately the same. This is most likely caused by the fact that at this particular power level, the microcavity, rather than not being able to heat-up rapidly enough, is instead no longer able to cool rapidly enough. Thus the microcavity resonance remains in its thermally shifted position over an entire period of the input sine wave, so that the cavity transmission remains high over the entire cycle but bistability is no longer occurring.

4.3 Free Carrier Induced Bistability

Having studied the response of the microcavities to thermally induced bistability in the previous section, the effect of free-carriers on the microcavity transmission will be considered next. As has already been mentioned, thermally induced refractive index changes will dominate at longer time-scales and for CW inputs [43], so that it becomes necessary to use short pulses to observe free-carrier induced bistability. For this reason, in order to eliminate any thermal effects, input pulses with FWHM's of $\tau_p = 5$ ns, generated using the optical modulator and function generator, were used initially as an input. Using pulses of this duration also ensured the free-carrier generation reached a steady-state within the pulse [43].

The method used to observe free-carrier bistability is essentially the same as that used to observe thermal bistability, with the input pulse acting as a power sweep that occurs over a much shorter time-scale. In this case however δ should be negative (λ is blue-detuned), as free-carriers lower the refractive index of Si, blue-shifting the resonance. Thus, for a blue-detuned input, as the pulse is incident on the microcavity the circulating power increases, leading to increased absorption and the generation of free-carriers. This will in turn lower the refractive index, shifting the resonance towards the input wavelength, λ. This increases the coupling to the microcavity, leading to increased circulating powers and therefore further absorption and free-carrier generation, providing the necessary positive feedback to observe bistability. When looking at the output from a bistable microcavity in the time domain one would thus expect to see a sharp increase in transmission at some point on the rising edge of the pulse, corresponding to a switch to the high transmission state, followed by a sharp fall in transmission on the falling edge, corresponding to a switch back to the low transmission state. This should all occur within a single pulse duration and leads to a distortion of the transmitted pulse relative to the input, indicating the presence of bistability.

In order to measure pulses with τ_p's of the order of tens of nanoseconds it was necessary to use a different, high-speed oscilloscope (*Agilent*; infinium DCA 86100A) and 45 GHz, InGaAs, IR detector (*New Focus*; Model 1014) to measure both the input and transmitted pulses (meaning the input and output could no longer be monitored simultaneously). Given the relatively low transmitted powers a 2 GHz high-speed electronic amplifier (*Femto*; HSA-X-2-40) was also required, to amplify the signal from the high-speed detector, prior to being measured by the high-speed oscilloscope. Once again the detector response was calibrated by obtaining the offset voltage for a 0 mW

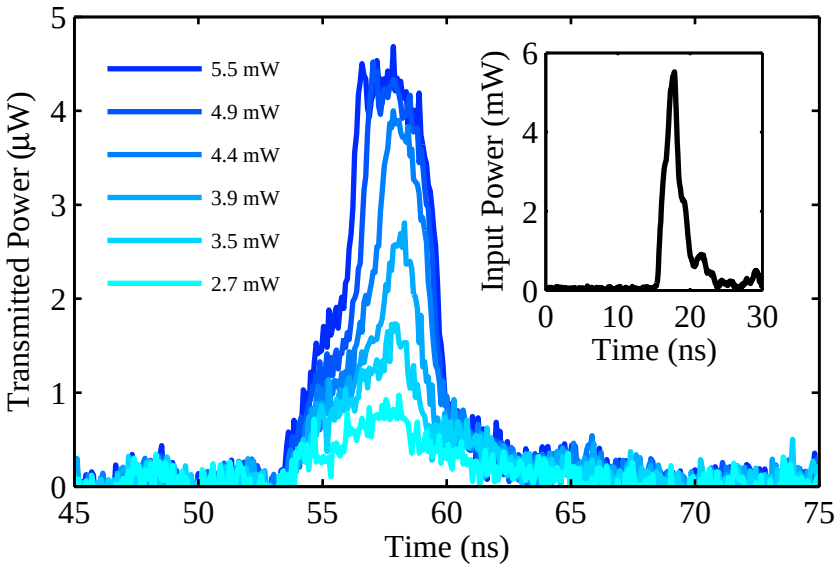

Figure 4.16: Measured microcavity transmission for 5 ns pulses with different peak powers and $\delta = -41$ pm. The inset shows the measured input pulse for a peak power of 5.5 mW.

input and for a CW input of known power, in order to convert the voltage measured by the oscilloscope to a transmitted power.

Initially, 5 ns pulses with a blue-detuning of $\delta = -47$ pm and a range of peak powers from 2.7 mW to 5.5 mW were used as an input to the microcavity. The resulting transmission measurements are shown in Fig. 4.16, along with the measured input pulse (inset) for comparison. A clear distortion of the transmitted pulse shape relative to the input for peak powers of 3.9 mW and greater demonstrates the presence of free-carrier induced bistability. There is a sudden, rapid increase in transmitted power on the leading edge of the pulse that occurs earlier as the peak power is increased, whilst the transmission remains high for longer on the trailing edge before an equally rapid fall in transmission. This leads to the observed asymmetry in the transmitted pulse and is caused by the generation of free-carriers that blue-shift the resonance towards the input pulse wavelength, causing the increase in transmission on the rising edge of the pulse. For increasing peak powers, free-carriers are generated more rapidly causing the sharp jump in transmission to occur earlier in the pulse. By contrast, on the falling edge of the pulse as the circulating power in the cavity is reduced the rate of free-carrier generation is reduced and the resonance begins to shift back to the original resonance position, eventually leading to the sharp drop in transmission. The threshold peak

power of 3.9 mW is comparable to that obtained for free-carrier induced bistability measured in silicon ring resonators [43]. It is also worth highlighting that the observed transitions between high and low transmission within the pulse duration occur over sub nanosecond time scales, suggesting the possibility of rapid switching between the high and low transmission states. To the best of the author's knowledge this is also the first time that free-carrier induced bistability has been observed using this method in Si 1D PhC microcavities.

Next a comparison was made between the transmission of red and blue-detuned pulses of 10 ns durations. First red-detuned pulses, with $\delta = +41$ pm, were used as an input to the microcavity for a range of peak powers. The resulting transmission measurements are shown in Fig. 4.17, with the input pulse shown in the inset for $P_p = 3.5$ mW. The transmitted power increases with increasing P_p up to ~ 800 nW, but there is no evidence of any bistable response in this case. This is of course to be expected as in this case λ is red-detuned and so any generated free-carriers will shift the resonance away from λ, ensuring no positive feedback. The measured transmission for the same input pulses but for $\delta = -41$ pm are shown in Fig. 4.18. For $P_p = 1.11$ mW and higher there is a large increase in the transmitted power, which is also much higher than for the red-detuned case. For $P_p = 1.11$ mW the distortion in the profile of the output pulse relative to the input is also evident, with the maximum transmitted power occurring after the peak of the pulse which is centred at $t = 60$ ns. As observed previously with the 5 ns pulses, as P_p is increased the switch to high transmission occurs earlier in time, so that the pulse becomes less and less asymmetric. The fact that the distortion to the transmitted pulses occurs only for blue-detuned pulses is further evidence that the bistability is free-carrier induced.

Next, the effect of varying the input pulse duration, τ_p, on the microcavity transmission was considered. The measured transmission for the same blue-detuning for τ_p ranging from 10 ns to 500 ns is shown in Fig. 4.19, along with the input pulse for $\tau_p = 500$ ns. For all of the pulse durations there is a rapid increase in transmission over the first 5 ns, from 0 µW to just above 2 µW, followed by a more gradual increase to a maximum transmission of just over 3 µW. For $\tau_p = 20$ ns and greater the increase in transmission is followed by a sharp drop almost to zero transmission, suggesting the microcavity is no longer on resonance with the input wavelength. Interestingly, the rapid switch off resonance occurs at exactly the same time (70 ns in Fig. 4.19) for all of the pulses. For pulses longer than 20 ns this sharp drop is followed by a gradual recovery of the transmission to around 1 µW over a duration of $\sim 60\ ns$. The transmission thus does

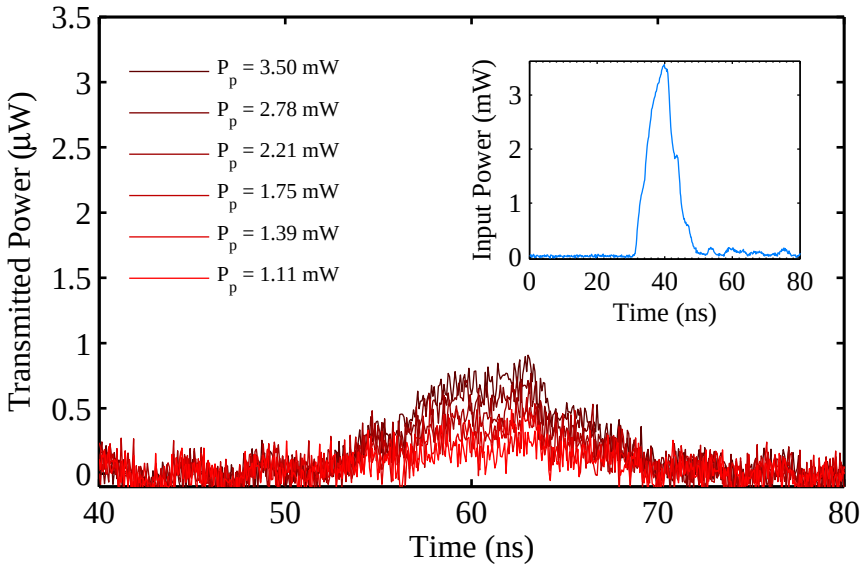

[H]

Figure 4.17: Measured microcavity transmission for 10 ns pulses with different peak powers and $\delta = +41$ pm. The inset shows the measured input pulse for a peak power of 3.5 mW.

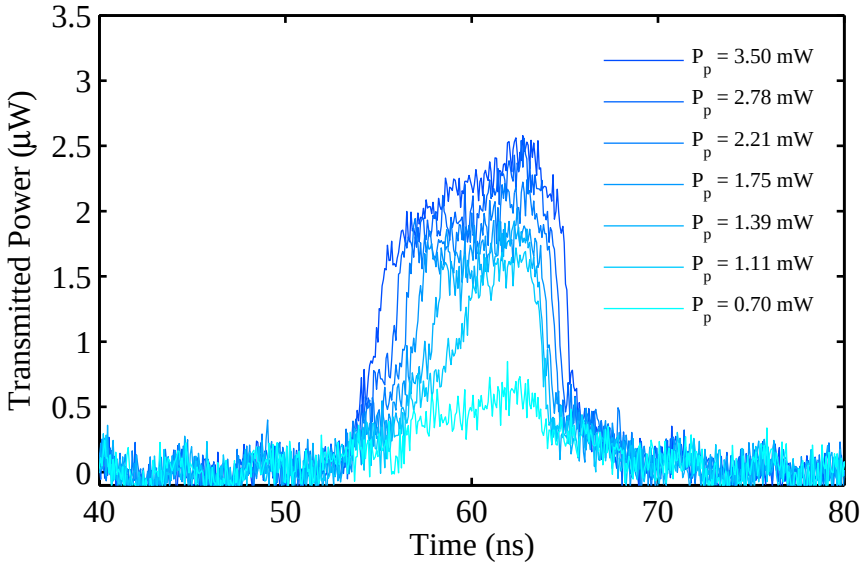

Figure 4.18: Measured microcavity transmission for 10 ns pulses with different peak powers and $\delta = -47$ pm. In this case bistablility occurs as the free-carrier induced shift moves the resonance closer to the input wavelength, leading to a distortion of the input pulse shape.

not return to the maximum value of $\sim 3\,\mu W$ before it undergoes a slight oscillation and then even more gradually begins to fall away over the remainder of the pulse for the longer durations.

This procedure was also repeated for the same red-detuning as used previously, the results of which are shown for τ_p's of 50 ns, 200 ns and 500 ns in Fig. 4.20. The measurements for the 200 ns and 500 ns pulses show a relatively slow increase in transmission up to the maximum of $3.3\,\mu W$ over a period of $\sim$ 110 ns. After this the transmission undergoes a series of oscillations in which the microcavity rapidly switches off resonance before more gradually switching on resonance again. The inset of Fig. 4.20 shows the transmission of a much longer $2\,\mu s$ pulse, for which the same oscillations are visible but begin to decay in amplitude after around 500 ns, resulting in an almost constant microcavity transmission after $1.5\,\mu s$. This suggests that by this time the detuning between the resonance and input wavelength has stabilised and the microcavity has reached a steady-state for these particular values of P_p, τ_p and δ. The complex behaviour of the microcavity transmission for longer pulse durations can be explained if one assumes that, in this regime, the free-carrier and thermal effects are competing with each other.

For red-detuned pulses, any optically induced free-carriers would initially cause the resonance to blue-shift away from the input wavelength. However, through a combination of linear and nonlinear absorption the incident pulse will also heat the cavity, increasing its temperature leading to a red-shift of the resonance towards the input wavelength. This is observed as the relatively slow increase in transmitted power over the first $\sim$160 ns of the pulses in Fig. 4.20. However, as the detuning between the input and resonance wavelengths are reduced the circulating power inside the cavity increases dramatically, leading to significantly increased rates of free-carrier generation. These newly generated free-carriers cause an even more rapid blue-shift of the cavity resonance, shifting it away from the input wavelength. The result is a much more rapid fall in transmitted power. A drop in transmitted power necessarily implies a drop in circulating power, which causes the rate of free-carrier generation to drop, whilst those already generated recombine, heating the cavity causing another red-shift of the resonance back towards the input wavelength. This causes the cavity transmission to increase again, so that the process repeats itself resulting in a series of oscillations in the transmitted signal. The cavity resonance is continuously red-shifted by thermal effects towards the input wavelength, before being blue-shifted away again by free-carriers generated when the cavity is on resonance with the input. The fact that free-carrier

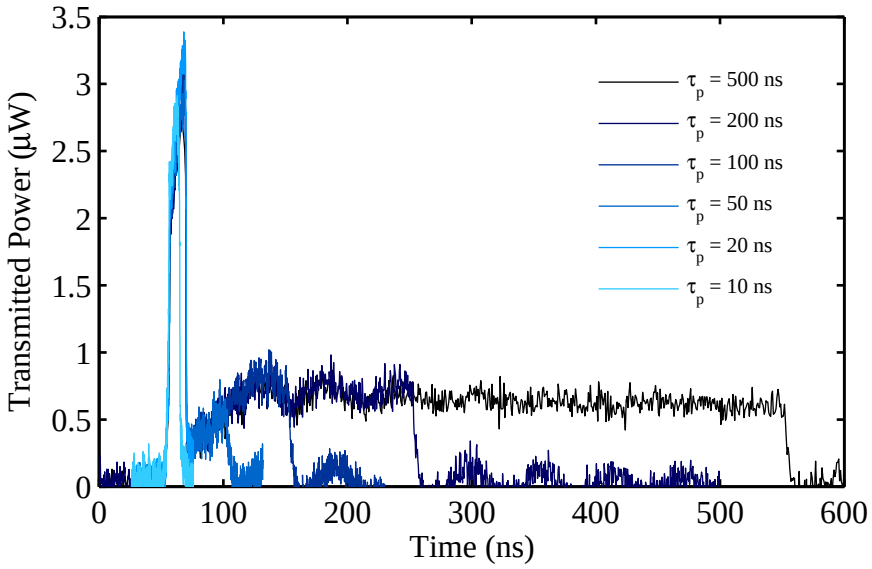

Figure 4.19: Measured microcavity transmission for varying input pulse durations, τ_p and $\delta = -41$ pm.

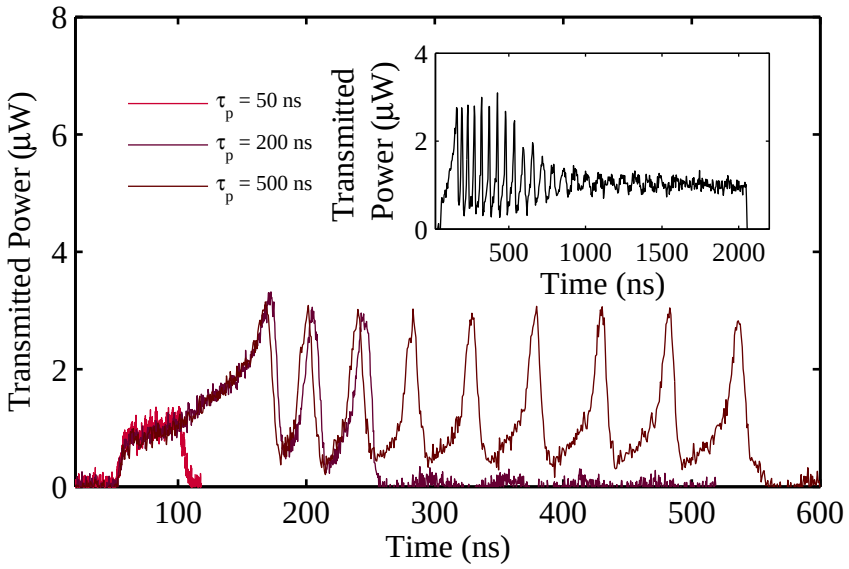

Figure 4.20: Measured microcavity transmission for varying input pulse durations, τ_p and $\delta = +41$ pm. Inset shows the measured microcavity transmission for a τ_p of 2 µs.

induced index changes can occur over a shorter time scale than any changes to the refractive index caused by thermal effects helps to explain the asymmetric shape of the oscillations in Fig. 4.20. After the very rapid switch off resonance caused by the

generation of free-carriers, the subsequent recovery of the microcavity transmission, that relies on thermal effects, is much slower resulting in the distinct shape of the observed oscillations. These types of oscillations, known as 'regenerative oscillations', 'self-oscillations', or alternatively 'self-pulsing', were predicted to occur in gallium arsenide microcavities with a non-instantaneous Kerr response [167] and semiconductor cavities due to free-carrier dispersion and absorption [168], and have been measured experimentally in a high Q-factor slicon microdisk [169] and a graphene clad silicon 2D-PhC microcavity [170].

4.4 Interplay of Thermal and Free Carrier Effects

In the previous section it was identified that for pulses with P_p of the order of a few milliwatts and durations in excess of ∼100 ns it is possible to observe a combination of both free-carrier and thermal effects, leading to oscillations of the microcavity transmission. In this section the transmission of 500 ns pulses with a range of peak powers and δ's are considered. Given the length of the input pulses the use of the high-speed oscilloscope and detector used previously was not necessary. Instead, the 300 MHz oscilloscope (*Tektronix*; DPO 3032) was used along with a detector (*Thorlabs*; DET01CFC) with a sub-nanosecond rise-time and the high-speed amplifier used in the previous section.

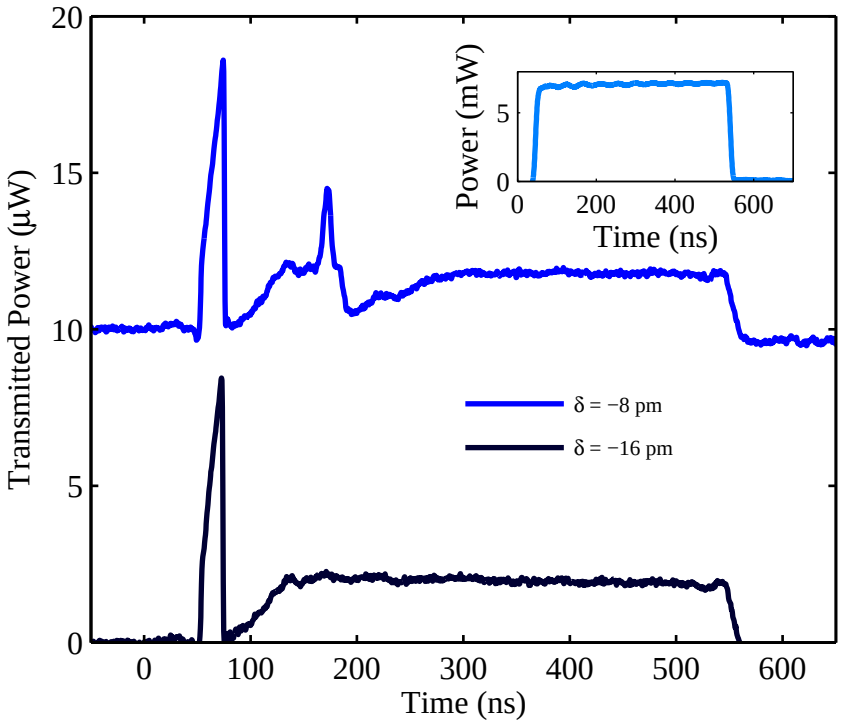

Figure 4.21: Measured microcavity transmission for 5 ns pulses with different peak powers and $\delta = -41$ pm. The inset shows the measured input pulse for a peak power of 5.5 mW.

First transmission measurements for a 500 ns pulse with a peak power of 7 mW, as shown in the inset of Fig. 4.21, were recorded for values of δ between -18 pm and +128 pm. Examples of the resulting transmitted pulses can be seen in figures 4.21 and 4.22. For both blue-detuned pulses (Fig. 4.21) the transmitted power rises rapidly to just over 8 µW before falling even more rapidly back to almost zero transmitted power. As seen in the previous section this is followed by a more gradual recovery of the microcavity transmission over around 50 ns. For $\delta = -16$ pm the transmitted power recovers to a maximum of 2 µW, before a slow decrease in transmitted power occurs over the remainder of the pulse. For $\delta = -8$ pm a second peak in transmission is clearly visible at 170 ns, although the transmitted power is ~ 4 µs in this case, followed by another sharp fall in transmission, but not to zero. Once again the transmission slowly begins to recover, before reaching a constant value.

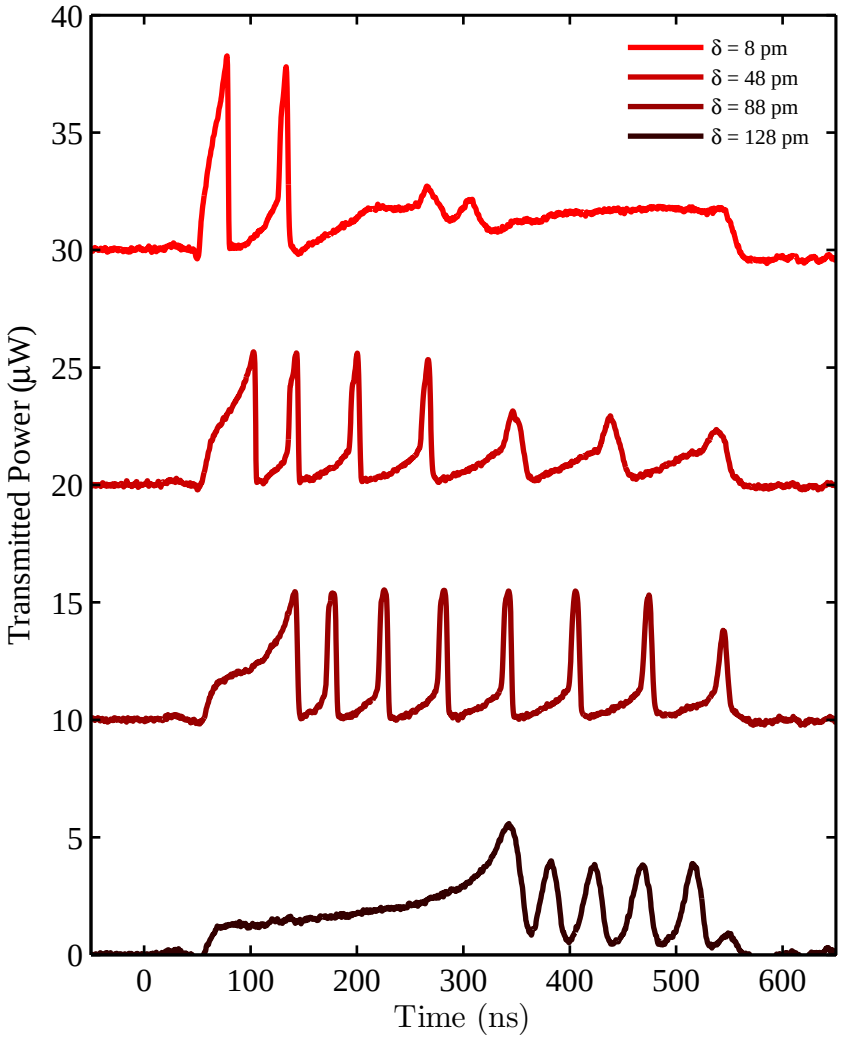

Figure 4.22: Measured microcavity transmission for 5 ns pulses with different peak powers and $\delta = -41$ pm. The inset shows the measured input pulse for a peak power of 5.5 mW.

For increasingly red-detuned pulses, like those shown in Fig. 4.22, clear oscillations in the microcavity transmission are observed. For the smallest red-detuning of +8 pm, two peaks in transmission are visible, with almost the same height of 8 μW. As δ is increased the time taken to reach maximum transmission increases, whilst the number of oscillations within the pulse initially increases and then decreases. This is of course understandable, as for increasingly large detunings the resonance has to red-shift further to be on resonance with the input, requiring a greater temperature change and therefore more time. The amplitude of the oscillations also decreases as δ is increased.

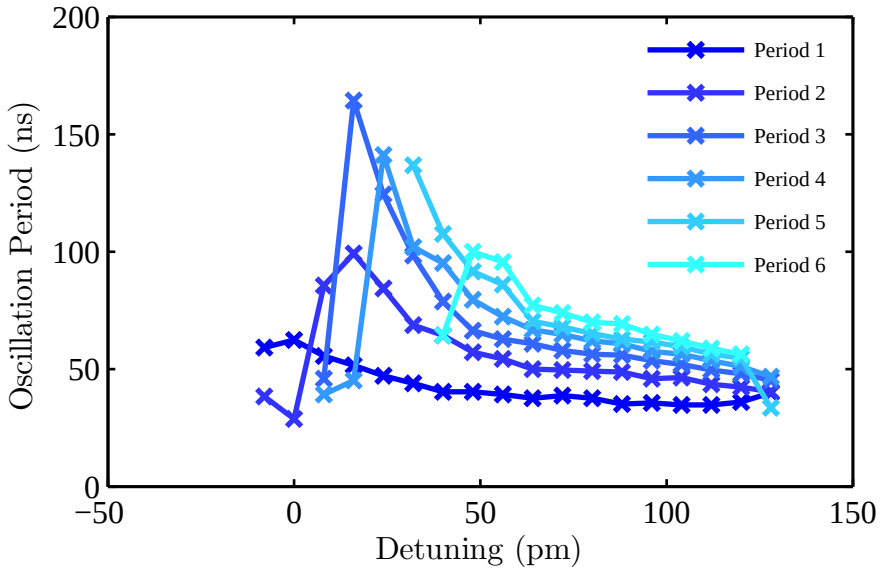

Figure 4.23: Plot of oscillation period, defined as the spacing between each maximum in transmission, extracted from the measured transmission of a 500 ns pulse for a range of δ's.

The spacing between the successive peaks in transmission for a given pulse, defined here as the oscillation period, is also seen to vary both across a single pulse and with detuning. This is in contrast to the measurements made on a graphene clad 2D-PhC microcavity mentioned earlier [170]. Figure 4.23 shows the oscillation period, extracted from each of the measured transmitted pulses like those shown in figures 4.6 and 4.22, plotted as a function of detuning. Looking at any single detuning the oscillation period is not constant throughout the pulse duration, but is instead seen to increase, i.e the spacing between successive peaks in transmission increases. At the same time the oscillation period is seen to decrease as the detuning is increased, reaching a minimum value for the maximum measured detuning of +128 pm. It can also be observed that, by contrast, the time to the first maximum in transmission increases with increased red-detuning. The increase in oscillation period over the course of a pulse appears to be caused by the microcavity taking longer to red-shift back on resonance, as opposed to the subsequent free-carrier induced switch-off taking longer. This could potentially be due to the microcavity heating up more slowly with each subsequent oscillation, or alternatively that after each peak in transmission, the subsequent blue-shift of the resonance is larger, resulting in the resonance needing to red-shift further for the transmission to recover again.

Finally, transmission measurements were obtained for a 500 ns square pulse at a fixed detuning of +97 pm for a range of peak powers from 2.8 mW to 7 mW. Examples of the measured transmissions are shown in Fig. 4.24. At lower powers the time to reach the first peak in transmission is much longer, whilst the amplitude of the subsequent oscillations are not as large and there aren't as many. Again, this is fairly intuitive as for lower input powers the cavity will heat up more slowly, resulting in longer time before peak transmission is reached. For higher powers (P_p = 7.7 mW) the time to reach the peak transmission is greatly reduced and the number of oscillations also increases. At the same time the amplitude of the oscillations also increases, such that between the successive peaks the microcavity transmission falls to almost zero within the sensitivity of the equipment used. The time to the first peak in transmission as a function of peak power, extracted from the transmission measurements, is shown in Fig. 4.25. At the lowest powers it takes ∼400 ns, a significant fraction of the entire pulse duration, to reach the maximum transmission, while for the maximum peak power of 7 mW this has fallen to around 100 ns. The overall shape of the curve is well approximated by assuming an inverse square dependence of time on peak power. As for detuning one can also plot oscillation period as a function of peak power, as shown in Fig. 4.26. In this case it can be seen that the oscillation period increases with increasing power. This is most likely due to the fact that for higher input powers more free-carriers are generated, so that the cavity has to red-shift further to compensate for the increased blue-shift resulting in a longer oscillation period. It is also worth nothing that oscillations in the transmitted pulse are observed for input powers as low as ∼3 mW (see Fig. 4.24), which is close to the levels observed in [170]. That particular cavity had Q = 7,500, compared to Q = 40,000 here, with the low threshold power of 1 mW attributed to the enhanced nonlinear response of the graphene. The results displayed above however demonstrate that it is possible to observe such oscillations in silicon 1D PhC microcavities at practical input power levels without the addition of a layer of graphene and for microcavities with only modest Q-factors. It is also reasonable to assume that using a 1D PhC microcavity with a larger Q-factor than those considered here would bring about further reductions in the threshold powers for observing regenerative oscillations. Indeed, with Q-factors in excess of 100,000 having been demonstrated for this type of microcavity [44], one would expect it would be possible to further reduce the threshold to well below those measured in [170].

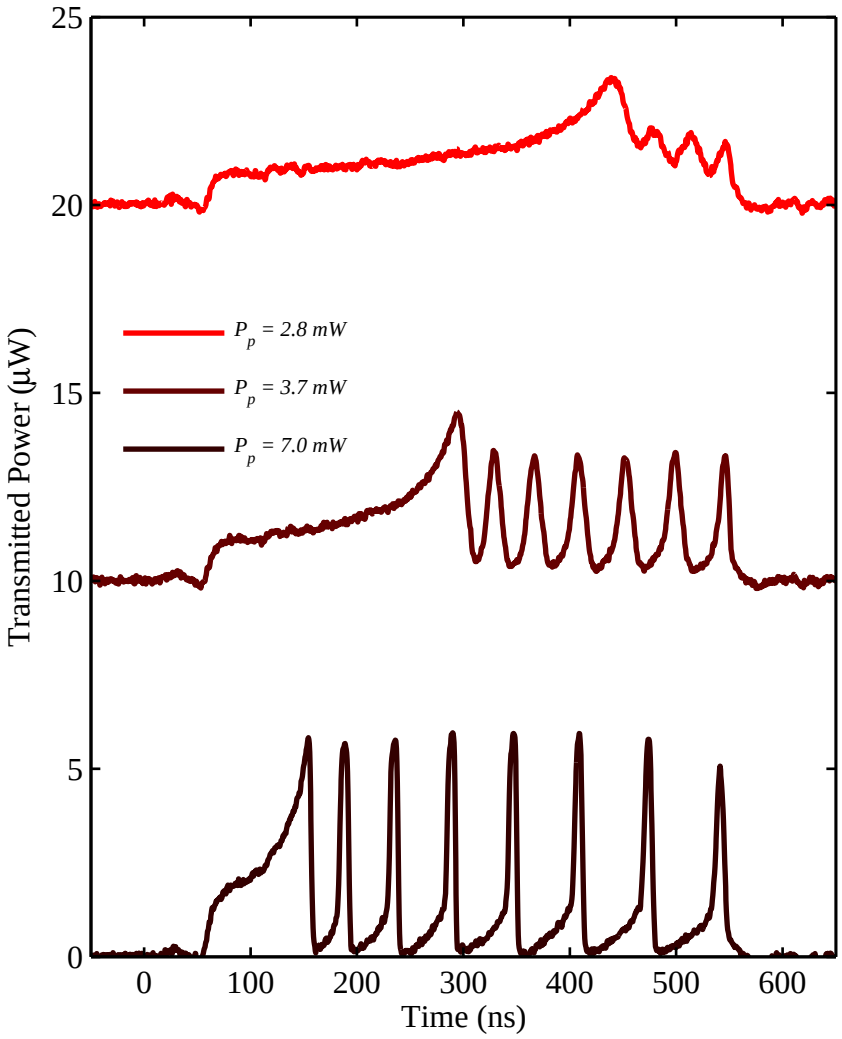

Figure 4.24: Measured transmission of 500 ns rectangular pulses with peak powers of 7.0 mW, 3.7 mW and 2.8 mW. Note that the measurements for 2.8 mW and 3.7 mW are offset by 10 µW and 20 µW on the vertical axis for clarity.

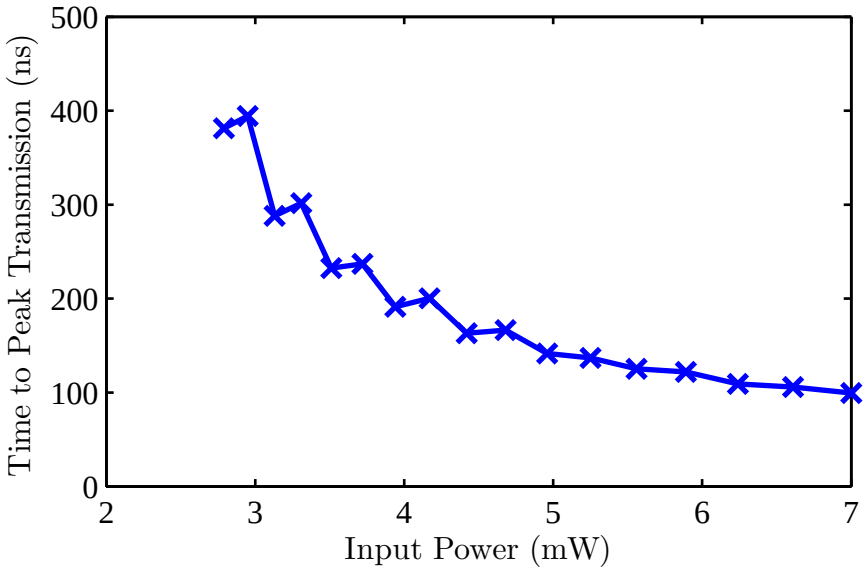

Figure 4.25: Time to first peak in transmission as a function P_p for a range of different input powers.

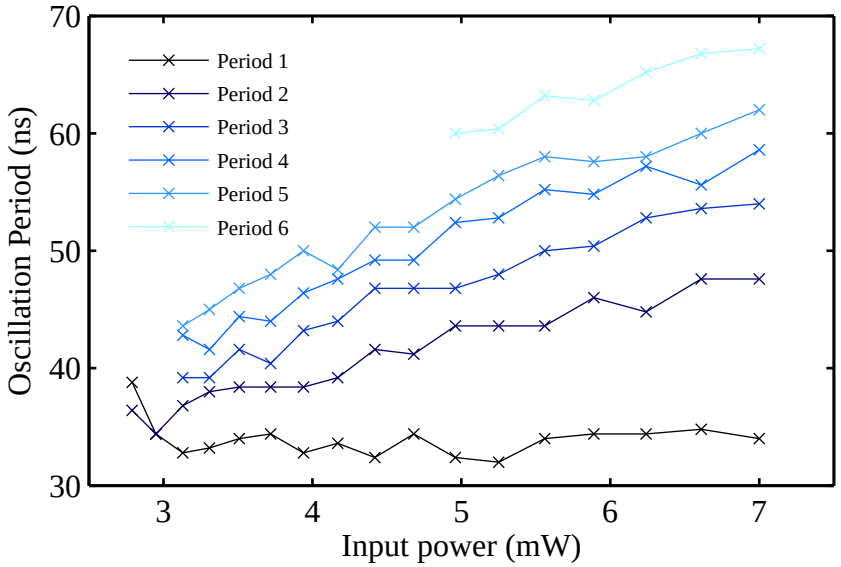

Figure 4.26: Plot of oscillation period as function of input power, extracted from the experimentally measured transmitted pulses.

4.5 Conclusions

The work undertaken in this chapter has characterised the nonlinear properties of 1D PhC microcavities in silicon. Thermally induced bistability was observed when sweeping the input wavelength at a fixed power for a microcavity with Q = 40,000, for a minimum power of $\sim 240\,\mu W$, whilst the magnitude of the wavelength shift was shown to vary linearly with input power. Hysteresis loops were then obtained for a range of positive detunings as further evidence of thermal bistability. A modulated input was then used to demonstrate that the microcavity could operate as a stable optical-memory component. For the range of powers and detuning used the high and low transmission states were stable for time scales of at least seconds, whilst a thermal time constant of $0.6\,\mu s$ was estimated for the data. This is comparable to other measurements made using silicon ring resonators and bragg cavities. The thermal response of the microcavities was investigated further using a sinusoidal input for a range of powers and detunings, indicating the frequency response of the microcavity. Following this free-carrier bistability was observed using pulses with milliwatt peak powers, the duration of which was set at 10 ns to avoid any competing thermal effects. Finally, the transmission of longer pulses hundreds of nanoseconds in duration were recorded for a range of detunings and powers. Regenerative oscillations, caused by the interplay between thermal and free-carrier effects on these time scales, were observed for input powers as low as ~ 3 mW. To the best of the authors knowledge this is the first time such oscillations have been observed in silicon 1D PhC microcavities.

Chapter 5

Conclusions and Future Work

In this thesis the optical properties of a silicon-on-insulator waveguide array, consisting of two evanescently coupled silicon photonic wires, and 1D PhC microcavities have been examined experimentally. The SOI platform and subwavelength waveguides and microcavities in general are an area currently receiving significant attention, due to their potential for both on-chip applications and also the rich new physics associated with them. The devices used throughput this work were fabricated by co-workers at the University of Glasgow.

Chapter 2 focussed on the linear properties of the two-wire array (directional coupler), specifically the dispersive properties, where the presence of coupling-induced dispersion for strongly coupled wires had been predicted. A two-wire array with a wall-to-wall separation of just 100 nm was used to ensure strong coupling and consequently a large coupling-induced dispersion. Group index measurements of the symmetric and antisymmetric TE supermodes were performed experimentally using a Mach-Zehnder interferometer over a range of wavelengths from 1200 nm to 2000 nm. As the input wavelength was increased, resulting in stronger coupling, a splitting of the interferogram was observed as the two supermodes began to propagate at different group velocities. The resulting group index plot showed good agreement between the experimental results and modelled data, obtained using a finite-element method mode solver, successfully demonstrating for the first time the presence of coupling-induced dispersion in waveguide arrays. The results obtained in this chapter were published in Optics Letters. The main consequence of this additional contribution to the dispersion was to extend the region of anomalous dispersion for the anti-symmetric supermode

and restrict if for the symmetric supermode relative to a single, uncoupled wire. The coupling strength in waveguide arrays thus provides an additional mechanism though which to control dispersion and makes it possible for light in an array to experience either normal or anomalous dispersion at certain wavelengths, depending on the supermode in which the light is propagating. Experimentally, exciting a specific supermode, although difficult, is possible by tilting the input beam when coupling into an array. The relative projections of the input light onto the supermodes of an array could also be changed by extending one of the wires at the input. The coupling-induced dispersion demonstrated here also has considerable implications for the types of nonlinear effects that can be observed in an array relative to a single wire. A natural progression of the work detailed in Chapter 1 would thus be to begin looking at the nonlinear properties of SOI waveguide arrays. As has been highlighted, work in this area has already begun, with measurements of supermodal soliton propagation [29] and modulation instability [90] in waveguide arrays having already been undertaken. In both instances the results were strongly affected by the presence of coupling-induced dispersion. There is still considerable scope for investigation however, as waveguide arrays provide a possible platform for observing spatio-temporal solitons or 'light-bullets'. These are pulses of light that are confined both in space and time through the careful balance of linear and nonlinear effects. Propagation in Si in the spectral region beyond 2.2 µm is another area receiving increased attention of late [171], [172], [67]. It would be relatively straightforward to re-optimise the array geometries for use in this wavelength region, which would bring the considerable advantage of working in a regime free from TPA. The absence of nonlinear absorption should make any nonlinear effects easier to observe, whilst potentially allowing a simpler theoretical description. Working in this spectral region may also make it easier to observe the spatio-temporal solitons mentioned above. The numerical modelling in Chapter 2 also indicated the existence of an anti-crossing between the antisymmetric TE and symmetric TM supermodes, as well as the cut-off of the antisymmetric TE supermode at around 1900 nm. The evidence for this was based on the single-mode appearance of the measured interferograms above 1900 nm, whilst the modelling also suggested that beyond this point the remaining supermode (symmetric TE) was propagating as a slot-mode. In order to prove this conclusively it may be possible to image the output of the arrays in the near-field, in order to directly observe light being confined in the low index air region between the wires.

The focus of the work reported here then shifted to the optical properties of 1D PhC microcavities in silicon, formed by introducing a series of holes into a silicon wire creating a pair of PhC mirrors that provide optical confinement in the propagation direction.

This particular microcavity design was chosen due to the potential for a high Q-factor and small V simultaneously, resulting in large values of the ratio Q/V. In Chapter 3 the transmission properties of a number of microcavities were characterised using CW, low power input light. Two cavities were found with moderately high Q-factors of around 40,000, which were used for the nonlinear measurements that followed. Although not the highest Q-factor measured for this type of microcavity, the underlying physics would remain the same, with an increase in Q-factor simply resulting in a reduced threshold power for a given nonlinear effect. A number of much lower Q-factor microcavities were also identified that possessed resonances that were strongly modulated. Initially it was believed that these background modulations were the result of Fabry-Pérot effects caused by additional reflections between the input and output facets of the waveguides. However, the spacing of the modulations indicated the reflections were occurring over a length shorter than the length of the waveguide, suggesting instead that the reflections were occurring at points along the waveguide. It was thus assumed that the reflections were arising because of fabrication defects, such as stitching errors, at various points along the devices. After identifying those microcavities with Q-factors of $\sim 40,000$ it then became apparent that it would be necessary to stabilise their temperature, in order to prevent any thermal drift of the resonances. This was achieved using a pair of Peltier devices and a platinum temperature sensor, used in conjunction with a laser diode controller to stabilise the temperature of the aluminium block on which the sample was mounted. This set-up also provided an opportunity to examine the possibility of thermally tuning the microcavities, with a resonance shift of 0.077 nm K^{-1} measured experimentally. The maximum on resonance transmission of the microcavities did vary significantly as the temperature changed however, as did the overall shape of the resonances.

The work presented in Chapter 4 moved on to look at the nonlinear response of those microcavities identified in the previous chapter. More specifically the phenomena of optical bistability, in which two stable resonant transmission states are possible for a given input, was investigated. The first mechanism used to induce a bistable response in the microcavities was the thermo-optic effect, relying on silicon's large and positive thermo-optic coefficient. Initially, nonlinear transmission spectra were recorded by sweeping the input wavelength for different, fixed input powers. As the input power to the microcavities was increased the resonances were found to red-shift and become increasingly asymmetric. For the microcavity with $Q = 40{,}000$ the sudden, sharp drop in transmission as the wavelength is swept from shorter to longer wavelengths, indicating the onset of bistability, was observed for an input power of 240 µW, corresponding to

an in waveguide power of approximately 80 µW. The wavelength shift was also found to be a linear function of the input power with a slope of 120 pm mW^{-1}, which is consistent with similar measurements made on silicon ring resonators. It was thus concluded that the dominant form of absorption occurring within the microcavities was linear in nature. Hysteresis loops, another characteristic of bistable systems, were then recorded by measuring the transmitted power as a function of the input power for a range of detunings. For sufficiently large, positive detunings hysteresis loops were observed, whilst none were observed for negative detunings. This provided further proof that the origin of the bistability in this case was thermal in nature. It was then demonstrated that the microcavities could be used as stable optical-memory elements using a modulated input. The high and low transmission states were shown to be stable for at least seconds and in addition the thermal time constant of the microcavities was estimated at 0.6 µs, which is once again consistent with other measurements obtained for silicon ring resonators and Bragg cavities. Following this, the frequency response of the microcavities was investigated further through the use of a sinusoidal input, which was distorted to resemble a square wave in the presence of bistability. Two different input powers were used for a range of different input frequencies at fixed detunings, with the microcavity showing a bistable response up to 200 kHz at the lower power. For the higher input power the bistable response was no longer present, but the transmission remained high. It was concluded that in this instance the microcavity no longer had sufficient time to cool over a single cycle, so that the resonance remained thermally shifted throughout and consequently the transmission remained high. Having examined the thermal response of the microcavities, pulses with 5 ns and 10 ns durations were employed in order to examine the effects of free-carriers on the mirocavity transmission. Pulses of this duration were necessary in order to eliminate any thermal response, which would oppose any free-carrier induced blue-shift of the resonance. A range of peak powers from 0.7 mW to 3.5 mW were used for positive and negative detunings of equal magnitude. Whilst no distortion of the transmitted pulse was observed for a positive detuning, a nonlinear dependence of the transmitted power and a distortion of the transmitted pulse were observed for a negative detuning, demonstrating the presence of free-carrier induced bistability. To the best of the author's knowledge this is the first time that these types of measurements have been made on 1D PhC microcavities. Finally, the effect of pulse duration on microcavity transmission was investigated, were it was found that red-detuned pulses with durations of hundreds of nanoseconds led to oscillations in the microcavity transmission. These regenerative oscillations, that arise here as a result of the interplay between thermal and free-carrier effects, have been observed in high Q-factor microdisks and in a graphene clad 2D-PhC microcavity, but never to

the authors knowledge in 1D-PhC microcavities. Measurements of the transmission of 500 ns pulses then demonstrated that the period of oscillation varies not only with detuning and peak power, but also within a single pulse, in contrast to measurements made on graphene clad Si 2D PhC microcavities [170]. The threshold powers at which the above oscillations were observed also demonstrate that it is possible to experimentally measure such oscillations in microcavities with only moderately high Q-factors and without the addition of graphene or other nonlinear materials. Having looked at thermal and free-carrier effects, potential future work could involve attempting to observe a modulation of the microcavity transmission due the optical Kerr effect. This is the fastest method by which to modulate the transmission of a microcavity and could possibly be implemented by having an ultra-short pulse incident on the cavity from above. Of course, the fact that any induced index change lasts only for the duration of the incident pulse would make detection of modulations to the microcavity transmission difficult to measure, so that an interferometric set-up would be necessary. The existing work could also be extended by looking at the effect of a cladding on the nonlinear response of the microcavities. Graphene has already been employed to enhance the nonlinear response of a 2D silicon PhC microcavity and, as such, it would be interesting to observe the effects of graphene on a 1D PhC microcavity like those considered here. Alternatively, a much simpler extension to the work undertaken here would be to look again at these measurements, but with microcavities with higher Q-factors to observe the effect that this has on the threshold powers required to observe the effects. Finally, taking inspiration from the work on arrays of evanescently coupled silicon wires presented in Chapter 2 of this thesis, it would also be possible to consider the linear and nonlinear properties of a series of coupled microcavities. Coupling could be achieved either by incorporating a number of microcavities into a single wire [173], or alternatively by having an array of transversely coupled microcavities [174].

Appendix A

Device Layout for the Waveguide Array Chip

Figure A.1 shows the layout of the devices on the chip containing the waveguide arrays used for the work in Chapter 2. The first half of the chip contains 12 two-wire arrays, 12 five-wire arrays, 12 nine-wire arrays and 12 fifteen-wire arrays, each made up of wires with 380 nm widths. On the second half of the chip the pattern was repeated, but the arrays consisted of individual wires with widths of 420 nm instead. This gave a total of 96 arrays on the chip in total. For each set of 12 arrays, the wall-to-wall separation of the individual wires was varied from 50 nm to 600 nm in 50 nm increments, providing arrays with a range of coupling strengths. Each array was $\sim$3.1 mm in length, whilst each individual wire had a height of 220 nm. It was also assumed that a residual layer of HSQ 160 nm thick was left on top of the Si waveguides after fabrication.

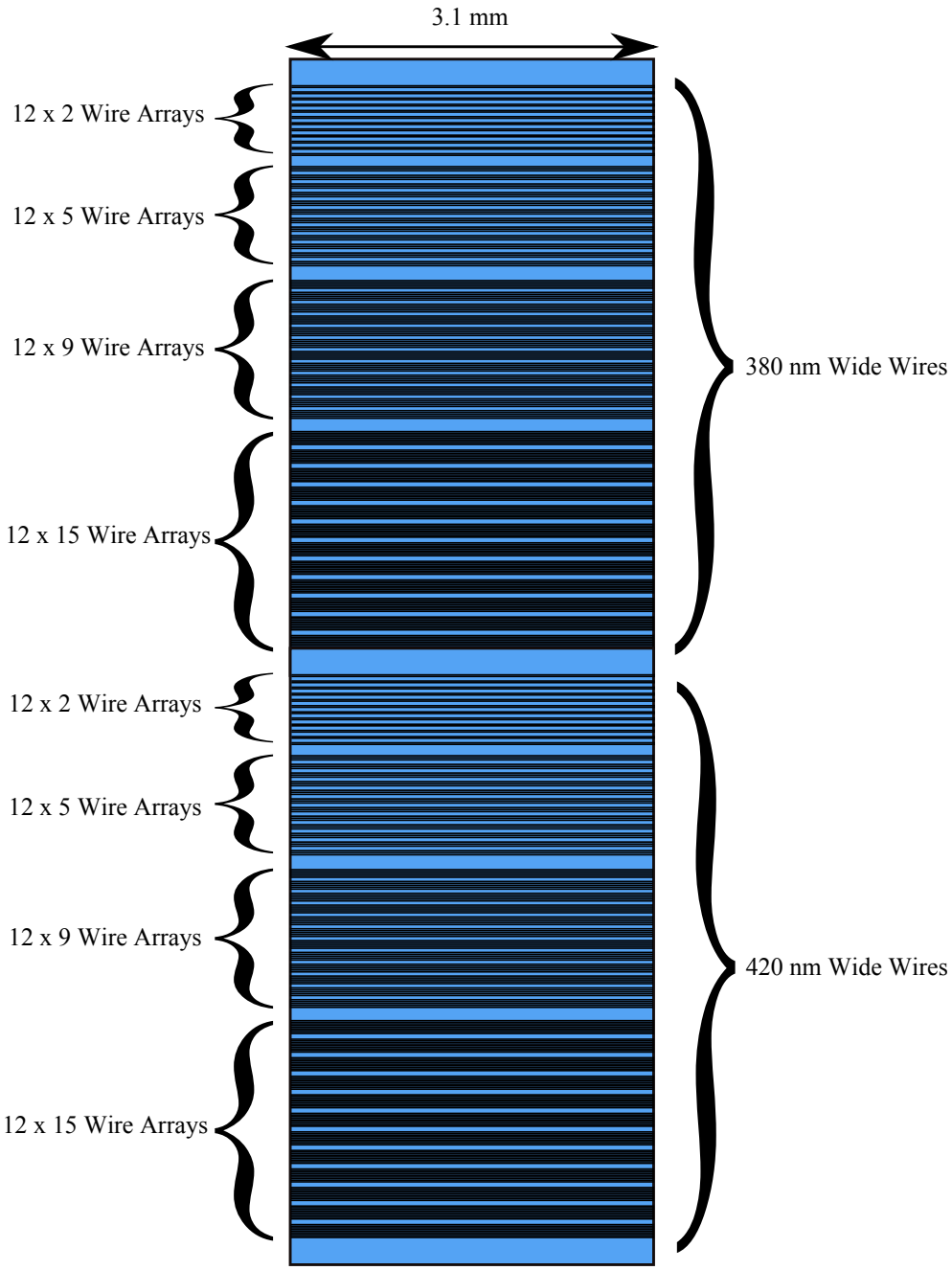

Figure A.1: Cartoon showing the layout of the waveguide arrays on the chip used for the work in Chapter 2. The first half of the chip consisted of 12 two-wire arrays, 12 five-wire arrays, 12 nine-wire arrays and 12 fifteen-wire arrays, made up of 380 nm wide wires. This pattern was then repeated, but with arrays made of 420 nm wide wires. The wall-to-wall separations in each set of 12 arrays were increased from 50 nm to 600 nm inclusive in 50 nm increments, whilst the length of each array was ∼3.1 mm. Each individual wire in the array had a height of 220 nm. Note that the diagram is not to scale.

References

[1] A. Al-Azzawi. *Photonics: Principles and Practices.* CRC Press Taylor & Francis Group, Miami, 2007.

[2] G. T. Reed and A. P. Knights. *Silicon Photonics: An Introduction.* Wiley, Hoboken, NJ, 2004.

[3] R. Soref. The Past, Present, and Future of Silicon Photonics. *IEEE Journal of Quantum Electronics*, 12(6):1678–1687, 2006.

[4] L. Pavesi and D. J. Lockwood. *Silicon Photonics.* Springer, New York, 2004.

[5] J. Bahram and S. Fathpour. Silicon Photonics. *Journal of Lightwave Technology*, 24(12):4600–4615, 2006.

[6] B. Jalali. Teaching silicon new tricks. *Nature Photonics*, 1(4):193–195, 2007.

[7] M. Lipson. Silicon photonics: the optical spice rack. *Electronics Letters*, 45(12):576–578, 2009.

[8] W. Bogaerts, R. Baets, P. Dumon, V. Wiaux, S. Beckx, D. Taillaert, B. Luyssaert, J. Van Campenhout, P. Bienstman, and D. Van Thourhout. Nanophotonic waveguides in silicon-on-insulator fabricated with CMOS technology. *Journal of Lightwave Technology*, 23(1):401–412, January 2005.

[9] J. B. Kuo and S. Lin. *Low-Voltage SOI CMOS VLSI Devices and Circuits.* John Wiley & Sons, Inc., Online, 2002.

[10] R. Hunsperger. *Integrated Optics: Theory and Technology.* Springer, 5th edition, 2002.

[11] R. A. Soref and J. P. Lorenzo. Single-crystal silicon: a new material for 1.3 and 1.6 μm integrated-optical components. *Electronics Letters*, 21(21):953–954, 1985.

[12] U. Fischer, T. Zinke, J.-R. Kropp, F. Arndt, and K. Petermann. 0.1 dB/cm Wavegide Losses in Single-Mode SOI Rib Wavegides. *IEEE Photonics Technology Letters*, 8(5):647–648, 1996.

[13] J. Cardenas, C. B. Poitras, J. T. Robinson, K. Preston, L. Chen, and M. Lipson. Low loss etchless silicon photonic waveguides. *Optics Express*, 17(6):4752–4757, 2009.

[14] M. Gnan, S. Thoms, D. S. Macintyre, R. M .De La Rue, and M. Sorel. Fabrication of low-loss photonic wires in silicon-on-insulator using hydrogen silsesquioxane electron-beam resist. *Electronics Letters*, 44(2):44–45, 2008.

[15] K. Wada, H. C. Luan, D. R. C. Lim, and L. C. Kimerling. On-chip interconnection beyond semiconductor roadmap-silicon microphotonics. *Proceedings of SPIE*, 4870:437–443, 2002.

[16] M. Lipson. Guiding, Modulating, and Emitting Light on Silicon - Challenges and Opportunities. *Journal of Lightwave Technology*, 23(12):4222–4238, 2005.

[17] H. Rong, A. Liu, R. Jones, O. Cohen, D. Hak, R. Nicolaescu, A. Fang, and M. Paniccia. An all-silicon Raman laser. *Nature*, 433(7023):292–294, 2005.

[18] D. Liang and J. E. Bowers. Recent progress in lasers on silicon. *Nature Photonics*, 4(8):511–517, 2010.

[19] Q. Lin, J. Zhang, P. M. Fauchet, and G. P. Agrawal. Ultrabroadband parametric generation and wavelength conversion in silicon waveguides. *Optics Express*, 14(11):4786–4799, 2006.

[20] L. Xu, N. Ophir, M. Menard, R. K. W. Lau, A. C. Turner-Foster, M. A. Foster, M. Lipson, A. L. Gaeta, and K. Bergman. Simultaneous wavelength conversion of ASK and DPSK signals based on four-wave-mixing in dispersion engineered silicon waveguides. *Optics Express*, 19(13):12172–12179, 2011.

[21] R. Espinola, J. Dadap, R. Osgood, S. McNab, and Y. Vlasov. Raman amplification in ultrasmall silicon-on-insulator wire waveguides. *Optics Express*, 12(16):3713–3718, 2004.

[22] M. A. Foster, A. C. Turner, J. E. Sharping, B. S. Schmidt, M. Lipson, and A. L. Gaeta. Broad-band optical parametric gain on a silicon photonic chip. *Nature*, 441(7096):960–963, 2006.

[23] G. T. Reed, editor. *Silicon Photonics the state of the art*. John Wiley & Sons, Ltd, Chichester, 2008.

[24] M. A. Foster, A. C. Turner, A. Lipson, and A. L. Gaeta. Nonlinear optics in photonic nanowires. *Optics Express*, 16(2):1070–1078, 2008.

[25] J. Leuthold, C. Koos, and W. Freude. Nonlinear silicon photonics. *Nature Photonics*, 4(8):535–544, 2010.

[26] D. N. Christodoulides, F. Lederer, and Y. Silberberg. Discretizing light behaviour in linear and nonlinear waveguide lattices. *Nature*, 424(6950):817–823, 2003.

[27] R. Morandotti, H. Eisenberg, Y. Silberberg, M. Sorel, and J. Aitchison. Self-Focusing and Defocusing in Waveguide Arrays. *Physical Review Letters*, 86(15):3296–3299, 2001.

[28] F. Lederer, G. Stegeman, D. Christodoulides, G. Assanto, M. Segev, and Y. Silberberg. Discrete solitons in optics. *Physics Reports*, 463(1-3):1–126, 2008.

[29] A. Gorbach, W. Ding, O. Staines, C. de Nobriga, G. Hobbs, W. Wadsworth, J. Knight, D. Skryabin, A. Samarelli, M. Sorel, and R. De La Rue. Spatiotemporal nonlinear optics in arrays of subwavelength waveguides. *Physical Review A*, 82(4):1 – 4, 2010.

[30] Q. Lin, O. J. Painter, and G. P. Agrawal. Nonlinear optical phenomena in silicon waveguides: modeling and applications. *Optics Express*, 15(25):16604–16644, 2007.

[31] M. Paniccia. Integrating silicon photonics. *Nature Photonics*, 4(8):498–499, 2010.

[32] G. T. Reed, G. Mashanovich, F. Y. Gardes, and D. J. Thomson. Silicon optical modulators. *Nature Photonics*, 4(8):518–526, 2010.

[33] G. Cocorullo, M. Iodice, and I. Rendina. All-silicon Fabry-Perot modulator based on the thermo-optic effect. *Optics Letters*, 19(6):420–422, 1994.

[34] W. M. Green, M. J. Rooks, L. Sekaric, and Y. A. Vlasov. Ultra-compact, low RF power, 10 Gb/s silicon Mach-Zehnder modulator. *Optics Express*, 15(25):17106–17113, 2007.

[35] Q. Xu, B. Schmidt, S. Pradhan, and M. Lipson. Micrometre-scale silicon electro-optic modulator. *Nature*, 435(May):325–327, 2005.

[36] A. V. Kavokin, J. J. Baumberg, G. Malpuech, and F. P. Laussy. *Microcavities*. Oxford University Press, Oxford, revised edition, 2011.

[37] K. J. Vahala. Optical microcavities. *Nature*, 424(6950):839–846, August 2003.

[38] H. Rong, S. Xu, Y.-H. Kuo, V. Sih, O. Cohen, O. Raday, and M. Paniccia. Low-threshold continuous-wave Raman silicon laser. *Nature Photonics*, 1(4):232–237, 2007.

[39] V.R. Almeida, C.A. Barrios, R.R. Panepucci, and M. Lipson. All-optical control of light on a silicon chip. *Nature*, 431(October):1081–1084, 2004.

[40] M. Belotti, M. Galli, D. Gerace, L. C. Andreani, G. Guizzetti, A. R. Md Zain, N. P. Johnson, M. Sorel, and R. M. De La Rue. All-optical switching in silicon-on-insulator photonic wire nano cavities. *Optics Express*, 18(2):1450–1461, 2010.

[41] H. M. Gibbs. *Optical Bistability: Controlling Light with Light*. Academic Press, New York, 1985.

[42] V. R. Almeida and M. Lipson. Optical bistability on a silicon chip. *Optics Letters*, 29(20):2387–2389, 2004.

[43] Q. Xu and M. Lipson. Carrier-induced optical bistability in silicon ring resonators. *Optics Letters*, 31(3):341–343, 2006.

[44] A. R. Zain, N. P. Johnson, M. Sorel, and R. M. De La Rue. Ultra high quality factor one dimensional photonic crystal/photonic wire micro-cavities in silicon-on-insulator (SOI). *Optics Express*, 16(16):12084–12089, 2008.

[45] E. Hecht. *Optics*. Addison-Wesley Longman Incorporated, 3rd edition, 1998.

[46] J. A. Buck. *Fundamentals of Optical Fibres*. John Wiley & Sons Inc., 2004.

[47] Y. R. Shen. *Principles of Nonlinear Optics*. John Wiley & Sons Inc., 2003.

[48] A. W. Snyder and J. Love. *Optical Waveguide Theory*. Kulwar Academic Publishers, 2000.

[49] T. Aalto. *Microphotonic silicon waveguide components*. PhD thesis, Helsinki University of Technology, 2004.

[50] J. C. Knight, T. A. Birks, R. F. Cregan, P. St. J. Russell, and J. P. de Sandro. Large mode area photonic crystal fibre. *Electronics Letters*, 34(13):1347–1348, 1998.

[51] G. P. Agrawal. *Nonlinear Fiber Optics*. Academic Press, San Diego, 3rd edition, 2001.

[52] N. A. Mortensen. Effective area of photonic crystal fibers. *Optics Express*, 10(7):341–348, 2002.

[53] J. C. Knight. Photonic crystal fibres. *Nature*, 424(6950):847–851, 2003.

[54] V. S. Afshar and T. M. Monro. A full vectorial model for pulse propagation in emerging waveguides with subwavelength structures part I: Kerr nonlinearity. *Optics express*, 17(4):2298–2318, 2009.

[55] D. F. Edwards. *Handbook of Optical Constants of Solids*. Academic Press, 1985.

[56] I. H. Malitson. Interspecimen Comparison of the Refractive Index of Fused Silica. *Journal of the Optical Society of America*, 55(10):1205–1209, 1965.

[57] A. C. Turner, C. Manolatou, B. S. Schmidt, M. Lipson, M. A. Foster, J. E. Sharping, and A. L. Gaeta. Tailored anomalous group-velocity dispersion in silicon channel waveguides. *Optics Express*, 14(10):4357–4362, 2006.

[58] C. J. Benton. *Solitons and Nonlinear Optics in Silicon-on-Insulator Photonic Wires*. PhD thesis, University of Bath, 2009.

[59] F. Grillot, L. Viv, S. Laval, and E. Cassan. Propagation loss in single-mode ultrasmall square silicon-on-insulator optical waveguides. *Journal of Lightwave Technology*, 24(2):891–896, 2006.

[60] P. Dumon, G. Priem, L. R. Nunes, W. Bogaerts, D. Van Thourhout, P. Bienstman, T. K. Liang, M. Tsuchiya, P. Jaenen, S. Beckx, J. Wouters, and R. Baets. Linear and Nonlinear Nanophotonic Devices Based on Silicon-on-Insulator Wire Waveguides. *Japanese Journal of Applied Physics*, 45(No. 8B):6589–6602, 2006.

[61] H. K. Tsang, C. S. Wong, T. K. Liang, I. E. Day, S. W. Roberts, A. Harpin, J. Drake, and M. Asghari. Optical dispersion, two-photon absorption and self-phase modulation in silicon waveguides at 1.5 μm wavelength. *Applied Physics Letters*, 80(3):416–418, 2002.

[62] Q. Lin, J. Zhang, G. Piredda, R. W. Boyd, P. M. Fauchet, and G. P. Agrawal. Dispersion of silicon nonlinearities in the near infrared region. *Applied Physics Letters*, 91(2):021111, 2007.

[63] D. Dimitropoulos, R. Jhaveri, R. Claps, J. C. S. Woo, and B. Jalali. Lifetime of photogenerated carriers in silicon-on-insulator rib waveguides. *Applied Physics Letters*, 86(7):071115–1 – 071115–3, 2005.

[64] R. Hull, editor. *Properties of Crystalline Silicon*. INSPEC, London, 1999.

[65] T. K. Liang and H. K. Tsang. Role of free carriers from two-photon absorption in Raman amplification in silicon-on-insulator waveguides. *Applied Physics Letters*, 84(15):2745–2747, 2004.

[66] A. C. Turner-Foster, M. A. Foster, J. S. Levy, C. B. Poitras, R. Salem, A. L. Gaeta, and M. Lipson. Ultrashort free-carrier lifetime in low-loss silicon nanowaveguides. *Optics Express*, 18(4):3582–3591, 2010.

[67] S. Zlatanovic, J. S. Park, S. Moro, J. M. C. Boggio, I. B. Divliansky, N. Alic, S. Mookherjea, and S. Radic. Mid-infrared wavelength conversion in silicon waveguides using ultracompact telecom-band-derived pump source. *Nature Photonics*, 4(August):561–564, 2010.

[68] R. J. Shul and S. J. Peartobs, editors. *Handbook of Advanced Processing Techniques*. Springer, 2000.

[69] B. E. A. Saleh and M. C. Teich. *Fundamentals of Photonics*. John Wiley & Sons Inc., 1991.

[70] W. T. Silverfast. *Laser Fundamentals*. Cambridge University Press, 2nd edition, 2004.

[71] H. A. Haus. *Waves and Fields in Optoelectronics*. Prentice Hall Inc., 1984.

[72] R. S. Quimby. *Photonics and Lasers*. John Wiley & Sons Inc., 2006.

[73] A. V. Kavokin, J. J. Baumberg, G. Malpuech, and F. P. Laussy. *Microcavities*. Oxford University Press, 2007.

[74] K. J. Vahala, editor. *Optical Microcavities*. World Scientific Publishing Co., 2004.

[75] A. F. J. Levi. *Applied Quantum Mechanics*. Cambridge University Press, 2003.

[76] W. Huang. Coupled-mode theory for optical waveguides: an overview. *Journal of the Optical Society of America A*, 11(3):963–983, 1994.

[77] A. Yariv, Y. Xu, R. K. Lee, and A. Scherer. Coupled-resonator optical waveguide: a proposal and analysis. *Optics Letters*, 24(11):711–713, 1999.

[78] C. Kittel. *Introduction to Solid State Physics*. John Wiley & Sons Inc., 8th edition, 2005.

[79] A. Ghatak and K. Thyagarajan. *Introduction to Fibre Optics*. Cambridge University Press, Cambridge, 1998.

[80] A. Locatelli, M. Conforti, D. Modotto, and C. De Angelis. Discrete negative refraction in photonic crystal waveguide arrays. *Optics Letters*, 31(9):1343–1345, 2006.

[81] T. Pertsch, T. Zentgraf, U. Peschel, A. Bräuer, and F. Lederer. Anomalous Refraction and Diffraction in Discrete Optical Systems. *Physical Review Letters*, 88(9):4–7, 2002.

[82] V. R. Almeida, Q. Xu, C. A. Barrios, and M. Lipson. Guiding and confining light in void nanostructure. *Optics Letters*, 29(11):1209–1211, 2004.

[83] C. J. Benton and D. V. Skryabin. Coupling induced anomalous group velocity dispersion in nonlinear arrays of silicon photonic wires. *Optics Express*, 17(7):5879–5884, 2009.

[84] W. H. Knox, N. M. Pearson, K. D. Li, and C. A. Hirlimann. Interferometric measurements of femtosecond group delay in optical components. *Optics letters*, 13(7):574–576, 1988.

[85] Z. Bor, K. Osvay, B. Racz, and G. Szabo. Group refractive index measurement by Michelson interferometer. *Optics Communications*, 78(2):9–12, 1990.

[86] J. Daniels and S. Diddams. Dispersion measurements with white-light interferometry. *Applied optics*, 13(6):1120–1129, 1996.

[87] J. M. Stone and J. C. Knight. Visibly "white" light generation in uniform photonic crystal fiber using a microchip laser. *Optics Express*, 16(4):2670–2675, 2008.

[88] K. K. Lee, D. R. Lim, H. Luan, A. Agarwal, J. Foresi, and L. C. Kimerling. Effect of size and roughness on light transmission in a Si/SiO$_2$ waveguide: Experiments and model. *Applied Physics Letters*, 77(11):1617–1619, 2000.

[89] C. E. de Nobriga, G. D. Hobbs, W. J. Wadsworth, J. C. Knight, D. V. Skryabin, A. Samarelli, M. Sorel, and R. M. De La Rue. Supermode dispersion and waveguide-to-slot mode transition in arrays of silicon-on-insulator waveguides. *Optics Letters*, 35(23):3925–3927, 2010.

[90] W. Ding, O. K. Staines, G. D. Hobbs, A. V. Gorbach, C. De Nobriga, W. J. Wadsworth, J. C. Knight, D. V. Skryabin, M. J. Strain, M. Sorel, and R. M. De La Rue. Modulational instability in a silicon-on-insulator directional coupler : role of the coupling-induced group velocity dispersion. *Optics Letters*, 37(4):668–670, 2012.

[91] G. S. Solomon, M. Pelton, and Y. Yamamoto. Modification of Spontaneous Emission of a Single Quantum Dot. *Physica Status Solidi (a)*, 178(1):341–344, 2000.

[92] S. Barland, J. R. Tredicce, M. Brambilla, L. A. Lugiato, S. Balle, M. Guidici, T. Maggipinto, L. Spinelli, G. Tissoni, T. Knodl, M. Miller, and R. Jager. Cavity solitons as pixels in semiconductor microcavities. *Nature*, 419(October):699–702, 2002.

[93] A. D. Stone. Wave-Chaotic Optical Resonators and Lasers. *Physica Scripta*, T90:248–262, 2001.

[94] S. Suzuki, Y. Hatakeyama, and Y. Kokubun. Precise control of wavelength channel spacing of microring resonator add-drop filter array. *Journal of Lightwave Technology*, 20(4):745–750, 2002.

[95] M. Notomi, A. Shinya, S. Mitsugi, G. Kira, E. Kuramochi, and T. Tanabe. Optical bistable switching action of Si high-Q photonic-crystal nanocavities. *Optics Express*, 13(7):2678–2687, 2005.

[96] K. Nozaki, A. Shinya, S. Matsuo, Y. Suzaki, T. Segawa, T. Sato, Y. Kawaguchi, R. Takahashi, and M. Notomi. Ultralow-power all-optical RAM based on nanocavities. *Nature Photonics*, 6(Advance Online Publication):1–5, 2012.

[97] T. J. Kippenberg, S. M. Spillane, D. K. Armani, and K. J. Vahala. Ultralow-threshold microcavity Raman laser on a microelectronic chip. *Optics Letters*, 29(11):1224–1226, 2004.

[98] W. Bogaerts, P. De Heyn, T. Van Vaerenbergh, K. De Vos, S. Kumar Selvaraja, T. Claes, P. Dumon, P. Bienstman, D. Van Thourhout, and R. Baets. Silicon microring resonators. *Laser & Photonics Reviews*, 6(1):47–73, 2012.

[99] M. Soltani, S. Yegnanarayanan, Q. Li, S. Member, and A. Adibi. Systematic Engineering of Waveguide-Resonator Coupling for Silicon Microring / Microdisk / Racetrack Resonators : Theory and Experiment. *IEEE Journal of Quantum Electronics*, 46(8):1158–1169, 2010.

[100] Q. Xu, D. Fattal, and R. G. Beausoleil. Silicon microring resonators with 1.5-micron radius. *Optics Express*, 16(6):4309–4315, 2008.

[101] S. Xiao, M. H. Khan, H. Shen, and M. Qi. Compact silicon microring resonators with ultra-low propagation loss in the C band. *Optics Express*, 15(22):14467144–75, 2007.

[102] A. Biberman, M. J. Shaw, E. Timurdogan, J. B. Wright, and M. R. Watts. Ultralow-loss silicon ring resonators. *Optics Letters*, 37(20):4236–4238, 2012.

[103] A. C. Turner, M. A. Foster, A. L. Gaeta, and M. Lipson. Ultra-low power parametric frequency conversion in a silicon microring resonator. *Optics Express*, 16(7):4881–4887, 2008.

[104] B. E. Little, J. S. Foresi, G. Steinmeyer, E. R. Thoen, S. T. Chu, H. A. Haus, E. P. Ippen, L. C. Kimerling, and W. Greene. Ultra-Compact Si - SiO Microring Resonator. *IEEE Photonics Technology Letters*, 10(4):549–551, 1998.

[105] F. Xia, M. Rooks, L. Sekaric, and Y. Vlasov. Ultra-compact high order ring resonator filters using submicron silicon photonic wires for on-chip optical interconnects. *Optics Express*, 15(19):11934–11941, 2007.

[106] M. Cai, O. Painter, K. J. Vahala, and P. C. Sercel. Fiber-coupled microsphere laser. *Optics Letters*, 25(19):1430–1432, 2000.

[107] D. K. Armani, T. J. Kippenberg, S. M. Spillane, and K. J. Vahala. Ultra-high-Q toroid microcavity on a chip. *Nature*, 421(February):925–928, 2003.

[108] J. S. Foresi, P. R. Villeneuve, J. Ferrera, E. R. Thoen, G. Steinmeyer, S. Fan, J. D. Joannopolous, L. C. Kimerling, H. I. Smith, and E. P. Ippen. Photonic-bandgap microcavities in optical wavegides. *Nature*, 390:143–145, 1997.

[109] G. Lecamp, J. P. Hugonin, P. Lalanne, R. Braive, S. Varoutsis, S. Laurent, A. Lematre, I. Sagnes, G. Patriarche, I. Robert-Philip, and I. Abram. Submicron-diameter semiconductor pillar microcavities with very high quality factors. *Applied Physics Letters*, 90(9):091120–1 – 091120–3, 2007.

[110] B. Song, S. Noda, T. Asano, and Y. Akahane. Ultra-high-Q photonic double-heterostructure nanocavity. *Nature Materials*, 4(3):207–210, 2005.

[111] M. Borselli, T. Johnson, and O. Painter. Beyond the Rayleigh scattering limit in high-Q silicon microdisks: theory and experiment. *Optics Express*, 13(5):1515–1530, 2005.

[112] S. M. Spillane, T. J. Kippenberg, K. J. Vahala, K. W. Goh, E. Wilcut, and H. J. Kimble. Ultrahigh- Q toroidal microresonators for cavity quantum electrodynamics. *Physical Review A*, 71(1):013817–1 – 013817–10, 2005.

[113] D. W. Vernooy, V. S. Ilchenko, H. Mabuchi, E. W. Streed, and H. J. Kimble. High-Q measurements of fused-silica microspheres in the near infrared. *Optics Letters*, 23(4):247–249, 1998.

[114] A.B. Matsko and V.S. Ilchenko. Optical resonators with whispering-gallery modes-part I: basics. *IEEE Journal of Selected Topics in Quantum Electronics*, 12(1):3–14, 2006.

[115] J. C. Knight, G. Cheung, F. Jacques, and T. A. Birks. Phase-matched excitation of whispering-gallery-mode resonances by a fiber taper. *Optics Letters*, 22(15):1129–1131, 1997.

[116] N. G. Stoltz, M. Rakher, S. Strauf, a. Badolato, D. D. Lofgreen, P. M. Petroff, L. a. Coldren, and D. Bouwmeester. High-quality factor optical microcavities using oxide apertured micropillars. *Applied Physics Letters*, 87(3):031105, 2005.

[117] S. Reitzenstein, a. Bazhenov, a. Gorbunov, C. Hofmann, S. Munch, a. Loffler, M. Kamp, J. P. Reithmaier, V. D. Kulakovskii, and a. Forchel. Lasing in high-Q quantum-dot micropillar cavities. *Applied Physics Letters*, 89(5):051107, 2006.

[118] T. F. Krauss, R. M. De La Rue, and S. Brand. Two-dimensional photonic-bandgap structures operating at near-infrared wavelengths. *Nature*, 383(24):699–702, 1996.

[119] J. D. Joannopolous, S. G. Johnson, J. N. Winn, and R. D. Meade. *Photonic Crystals Molding the Flow of Light*. Princeton University Press, 2nd edition, 2008.

[120] T. Yoshie, J. Vuckovic, A. Scherer, H. Chen, and D. Deppe. High quality two-dimensional photonic crystal slab cavities. *Applied Physics Letters*, 79(26):4289–4291, 2001.

[121] A. Chutinan and S. Noda. Waveguides and waveguide bends in two-dimensional photonic crystal slabs. *Physical Review B*, 62(7):4488–4492, 2000.

[122] Y. Akahane, T. Asano, B. Song, and S. Noda. Investigation of high-Q channel drop filters using donor-type defects in two-dimensional photonic crystal slabs. *Applied Physics Letters*, 83(8):1512–1514, 2003.

[123] K. Srinivasan, P. E. Barclay, O. Painter, J. Chen, A. Y. Cho, and C. Gmachl. Experimental demonstration of a high quality factor photonic crystal microcavity. *Applied Physics Letters*, 83(10):1915–1917, 2003.

[124] C. Sauvan, P. Lalanne, and J. Hugonin. Slow-wave effect and mode-profile matching in photonic crystal microcavities. *Physical Review B*, 71(16):165118–1 – 165118– 4, 2005.

[125] Y. Akahane, T. Asano, B. Song, and S. Noda. Fine-tuned high-Q photonic-crystal nanocavity. *Optics Express*, 13(4):1202–1214, 2005.

[126] E. Kuramochi, M. Notomi, S. Mitsugi, A. Shinya, T. Tanabe, and T. Watanabe. Ultrahigh-Q photonic crystal nanocavities realized by the local width modulation of a line defect. *Applied Physics Letters*, 88(4):041112–1 – 041112–3, 2006.

[127] B. Song, T. Asano, Y. Akahane, Y. Tanaka, and S. Noda. Transmission and reflection characteristics of in-plane hetero-photonic crystals. *Applied Physics Letters*, 85(20):4591–4593, 2004.

[128] O. Painter, R. Lee, A. Scherer, A. Yariv, J. O'Brien, P. Dapkus, and I. Kim. Two-dimensional photonic band-gap defect mode laser. *Science*, 284(5421):1819–1821, 1999.

[129] S. Fan, J. D. Joannopoulos, J. N. Winn, A. Devenyi, J. C. Chen, and R. D. Meade. Guided and defect modes in periodic dielectric waveguides. *Journal of the Optical Society of America B*, 12(7):1267–1272, 1995.

[130] J. D. Joannopoulos, S. G. Johnson, J. N. Winn, and R. D. Meade. *Photonic Crystals Molding the Flow of Light*. Princeton University Press, 2nd edition, 2008.

[131] P. Lalanne, C. Sauvan, and J. P. Hugonin. Photon confinement in photonic crystal nanocavities. *Laser & Photonics Review*, 2(6):514–526, 2008.

[132] D. Peyrade, E. Silberstein, Ph. Lalanne, A. Talneau, and Y. Chen. Short Bragg mirrors with adiabatic modal conversion. *Applied Physics Letters*, 81(5):829–830, 2002.

[133] P. Velha, E. Picard, T. Charvolin, E. Hadji, J. C. Rodier, P. Lalanne, and D. Peyrade. Ultra-High Q/V Fabry-Perot microcavity on SOI substrate. *Optics Express*, 15(24):16090–16096, 2007.

[134] M. Palamaru and P. Lalanne. Photonic crystal waveguides: Out-of-plane losses and adiabatic modal conversion. *Applied Physics Letters*, 78(11):1466–1467, 2001.

[135] C. Sauvan, G. Lecamp, P. Lalanne, and J. Hugonin. Modal-reflectivity enhancement by geometry tuning in Photonic Crystal microcavities. *Optics Express*, 13(1):245–255, 2005.

[136] P. Velha, J. C. Rodier, P. Lalanne, J. P. Hugonin, D. Peyrade, E. Picard, T. Charvolin, and E. Hadji. Ultra-high-reflectivity photonic-bandgap mirrors in a ridge SOI waveguide. *New Journal of Physics*, 8(9):1–14, 2006.

[137] Q. Quan and M. Loncar. Deterministic design of wavelength scale, ultra-high Q photonic crystal nanobeam cavities. *Optics Express*, 19(19):18529–18542, 2011.

[138] T. J. Kippenberg. *Nonlinear Optics in Ultra-high-Q Whispering-Gallery Optical Microcavities*. PhD thesis, California Institute of Technology, 2004.

[139] A. R. Zain. *One-dimensional Photonic Crystal / Photonic Wire Cavities Based on Silicon-on-Insulator (SOI)*. PhD thesis, University of Glasgow, 2009.

[140] R. G. Walker. Simple and accurate loss measurement technique for semiconductor optical waveguides. *Electronics Letters*, 21(13):581–583, 1985.

[141] G. Corcorullo and I. Redina. Thermo-Optical Modulation at 1.5 Microns In Silicon Etalon. *Electronics Letters*, 28(1):83–85, 1992.

[142] G. K. White. Thermal expansion of reference materials : copper, silica and silicon. *J. Phys. D: Appl. Phys*, 6:2070–2078, 1973.

[143] R. G. Hicks. Switchable materials: A new spin on bistability. *Nature chemistry*, 3(3):189–191, 2011.

[144] C. Schirm, M. Matt, F. Pauly, J. C. Cuevas, P. Nielaba, and E. Scheer. A current-driven single-atom memory. *Nature nanotechnology*, 8(9):645–648, 2013.

[145] J. R. Pomerening. Uncovering mechanisms of bistability in biological systems. *Current opinion in biotechnology*, 19(4):381–388, 2008.

[146] A. Szoke, V. Daneu, J. Goldhar, and N. A. Kurnit. Bistable Optical Element and its Applications. *Applied Physics Letters*, 15(11):376–379, 1969.

[147] H. M. Gibbs, S. L. McCall, and T. N. C. Venkatesan. Differential Gain and Bistability Using a Sodium-Filled Fabry-Perot Interferometer. *Physical Review Letters*, 36(19):1135–1138, 1976.

[148] R. W. Boyd. *Nonlinear Optics*. Academic Press, 2nd edition, 2003.

[149] L. Haret, T. Tanabe, E. Kuramochi, and M. Notomi. Extremely low power optical bistability in silicon demonstrated using 1D photonic crystal nanocavity. *Optics Express*, 17(23):21108–21117, 2009.

[150] X. Yang, C. Husko, C. W. Wong, M. Yu, and D. Kwong. Observation of femtojoule optical bistability involving Fano resonances in high-QV silicon photonic crystal nanocavities. *Applied Physics Letters*, 91(5):051113–1 – 051113–3, 2007.

[151] G. S. He and S. H. Liu. *Physics of Nonlinear Optics*. World Scientific Publishing Co. Pte. Ltd., 1999.

[152] M. Soljačić, M. Ibanescu, S. Johnson, Y. Fink, and J. Joannopoulos. Optimal bistable switching in nonlinear photonic crystals. *Physical Review E*, 66(5):055601–1 – 055601–4, 2002.

[153] P. Barclay, K. Srinivasan, and O. Painter. Nonlinear response of silicon photonic crystal microresonators excited via an integrated waveguide and fiber taper. *Optics Express*, 13(3):801–820, 2005.

[154] M. Soljacić and J. D. Joannopoulos. Enhancement of nonlinear effects using photonic crystals. *Nature materials*, 3(4):211–219, 2004.

[155] A. D. Bristow, N. Rotenberg, and H. M. van Driel. Two-photon absorption and Kerr coefficients of silicon for 850 - 2200 nm. *Applied Physics Letters*, 90(19):191104–1 – 191104–3, 2007.

[156] A. Gondarenko, J. S. Levy, and M. Lipson. High confinement micron-scale silicon nitride high Q ring resonator. *Optics Express*, 17(14):11366–11370, 2009.

[157] K. Ikeda, R. E. Saperstein, N. Alic, and Y. Fainman. Thermal and Kerr nonlinear properties of plasma-deposited silicon nitride/ silicon dioxide waveguides. *Optics Express*, 16(17):12987–12994, 2008.

[158] G. Ctistis, E. Yuce, A. Hartsuiker, J. Claudon, M. Bazin, J. Gerard, and W. L. Vos. Ultimate fast optical switching of a planar microcavity in the telecom wavelength range. *Applied Physics Letters*, 98(16):161114–1 – 161114–3, 2011.

[159] E. Yüce, G. Ctistis, J. Claudon, E. Dupuy, R. D. Buijs, B. de Ronde, A. P. Mosk, Je. Gérard, and W. L. Vos. All-optical switching of a microcavity repeated at terahertz rates. *Optics Letters*, 38(3):374–376, 2013.

[160] E. Yüce, G. Ctistis, J. Claudon, E. Dupuy, Klaus J. Boller, J. Gérard, and W. L. Vos. Competition between electronic Kerr and free-carrier effects in an ultimate-fast optically switched semiconductor microcavity. *Journal of the Optical Society of America B*, 29(9):2630–2641, 2012.

[161] R. Soref and B. Bennett. Electrooptical effects in silicon. *IEEE Journal of Quantum Electronics*, 23(1):123–129, 1987.

[162] H. C. Nguyen, Yc Sakai, M. Shinkawa, N. Ishikura, and T. Baba. 10 Gb/s operation of photonic crystal silicon optical modulators. *Optics Express*, 19(14):13000–13007, 2011.

[163] G. T. Reed, G. Mashanovich, F. Y. Gardes, and D. J. Thomson. Silicon optical modulators. *Nature Photonics*, 4(8):518–526, 2010.

[164] M. Fox. *Optical Properties of Solids*. Oxford University Press, 2001.

[165] T. Carmon, L. Yang, and K. Vahala. Dynamical thermal behavior and thermal self-stability of microcavities. *Optics Express*, 12(20):4742–4750, 2004.

[166] M. W. Pruessner, T. H. Stievater, M. S. Ferraro, and W. S. Rabinovich. Thermo-optic tuning and switching in SOI waveguide Fabry-Perot microcavities. *Optics Express*, 15(12):7557–7563, 2007.

[167] A. Armaroli, S. Malaguti, G. Bellanca, and S. Trillo. Oscillatory dynamics in nano-cavities with non-instantaneous Kerr response. *Physical Review A*, 84:1–7, 2011.

[168] S. Malaguti, G. Bellanca, A. de Rossi, S. Combrié, and S. Trillo. Self-pulsing driven by two-photon absorption in semiconductor nanocavities. *Physical Review A*, 83(Rapid Communications):051802–1 – 051802–4, 2011.

[169] T. J. Johnson, M. Borselli, and O. Painter. Self-induced optical modulation of the transmission through a high-Q silicon microdisk resonator. *Optics Express*, 14(2):817–831, 2006.

[170] T. Gu, N. Petrone, J. F. Mcmillan, A. V. D. Zande, M. Yu, G. Q. Lo, D. L. Kwong, J. Hone, and C. W. Wong. Regenerative oscillation and four-wave mixing in graphene optoelectronics. *Nature Photonics*, 6(July):554–559, 2012.

[171] X. Liu, R. M. Osgood, Y. A. Vlasov, and W. M. J. Green. Mid-infrared optical parametric amplifier using silicon nanophotonic waveguides. *Nature Photonics*, 4(August):2–5, 2010.

[172] R. Soref. Mid-infrared photonics in silicon and germanium. *Nature Photonics*, 4(8):495–497, 2010.

[173] A. R. Zain, N. P. Johnson, M. Sorel, and R. M. De La Rue. Coupling strength control in photonic crystal/cavity wire multiple cavity devices. *Electronics Letters*, 45(May):283–284, 2009.

[174] S. Azzini, D. Grassani, M. Galli, D. Gerace, M. Patrini, M. Liscidini, P. Velha, and D. Bajoni. Stimulated and spontaneous four-wave mixing in silicon-on-insulator coupled photonic wire nano-cavities. *Applied Physics Letters*, 103(3):031117–1 – 031117–4, 2013.